QST

ANNUAL REPORT

2021

Kansai Photon Science Institute

Quantum Beam Science Research Directorate

National Institutes for Quantum Science and Technology

KPSI ANNUAL REPORT 2021

Contents

はじめに

　本年報では、関西光科学研究所（以下、関西研）において 2021 年度に実施された研究開発の主だった成果を紹介しています。関西研は国立研究開発法人量子科学技術研究開発機構（以下、量研）の研究開発拠点であり、けいはんな学研都市にある京都府木津地区と兵庫県播磨地区の 2 か所に研究サイトを持っています。そこでは、研究系職員約 80 名及びそれを支える技術系・事務系スタッフを含めて総勢約 150 名のスタッフが、量研における関西研のミッションである「レーザーや放射光による光科学技術の研究開発」を推進しています。木津地区では、世界トップレベルの高強度レーザー技術を基盤としたレーザー加速や X 線発生等のレーザー駆動の新しい放射線源開発、レーザーの短パルス性を活かした超高速計測技術開発、そして放射線影響や創薬に資する量子生命科学の最先端の研究開発を実施しています。また、播磨地区では、大型放射光施設 SPring-8 の 2 本の専用ビームラインと計算機シミュレーションを活用することで、新しい放射光 X 線利用技術開発と物質材料科学の最先端研究を展開しています。

　量研関西研として 6 年が経ち、新しい組織の中で優れた研究成果が生まれ始めています。木津地区のレーザー科学分野においては、プラズマミラーを用いた J-KAREN-P レーザーのパルスコントラストの改善や、レーザー加速研究における極薄膜照射実験、次世代のレーザーの基盤技術となる OPCPA 用高安定励起源開発や新しいタイプの発振器開発、そして光と物質の相互作用に関する理論研究などについて着実な成果を挙げました。量子生命科学分野においては、生物の概日リズム生成に関与するたんぱく質の構造や、発がんに関連したヌクレオソームヒストンの構造メカニズムの解明、そしてモンテカルロシミュレーションを用いた遺伝子突然変異のメカニズム解明に向けた研究などを着実に進めています。また、播磨地区においても、放射光 X 線を用いた水素貯蔵合金開発や物質内部のナノ結晶の観察に加え、反強磁性体におけるスピンダイナミクスの理論に関する研究や、将来の放射光実験を見据えたデータ取得の機械学習と自動化などの優れた成果を挙げています。さらに、光技術の社会実装の観点からは、医療応用をめざした小型高輝度光源開発やレーザーによるトンネル検査技術の実用化に向けた取り組みを引き続き行っています。

　関西光科学研究所は、「光」を通じた我が国の量子科学技術の発展とイノベーション戦略に貢献する開かれた研究拠点としての役割を果たすべく、今後とも職員一同、より一層努力してまいります。皆様のご理解・ご協力を宜しくお願い申し上げます。

<div align="right">

2022 年吉日
関西光科学研究所　所長
河内　哲哉

</div>

Preface

This annual report from Kansai Photon Science Institute (KPSI) provides highlights of the scientific and technical research that was conducted over the 2021 fiscal year. KPSI is one of the research and development (R&D) bases of the National Institutes for Quantum Science and Technology (QST) and has two R&D sites, the Kizu site in Keihanna science city in Kyoto prefecture and the Harima site in Hyogo prefecture. There are about 150 staff, comprising around 80 researchers and the technical and administrative staff who support them. We promote the R&D of optical science and technology using lasers and synchrotron-radiation X-rays, which is the mission of KPSI in QST. At the Kizu site, we are conducting state-of-art research such as developing new-type laser-driven radiation sources such as laser accelerated particle beams and ultrashort X-rays based upon world-leading top-class high-intensity laser technology, ultrafast measurement methodology using ultrashort pulse technology, and quantum life science which helps us understand radiation effects and develop new medicines. At the Harima-site, using two contract beamlines of SPring-8 and computer simulation, we are developing new technology to utilize synchrotron radiation X-rays and carrying out state-of-art research in material science.

Six years have passed since the restart of KPSI in QST, and several outstanding results are being produced. In the laser science field at the Kizu site, we have steadily achieved results in areas such as the improvement of the pulse contrast of the J-KAREN-P laser using a plasma mirror, ultra-thin film irradiation experiments in laser acceleration research, development of a highly stable pump source for OPCPA and a new-type oscillator which are expected to become basic technology of next-generation lasers, and theoretical research in laser-matter interaction. In the field of quantum life science, we are steadily proceeding in areas such as the elucidation of the structure of the protein complex involved in the generation of circadian rhythms in living organisms, the establishment of a novel approach for measuring the "Cluster DNA damage" using an atomic force microscope (AFM), and the mechanism of gene mutation using Monte Carlo simulation. Additionally at the Harima site, we have achieved excellent results in areas such as the clarification of the hydrogenation mechanism of Fe-Mo alloy under high pressure, the observation of nanocrystals inside a material via Bragg coherent diffraction imaging using synchrotron X-rays, the theoretical study of spin dynamics in antiferromagnetic materials, and also we have made good progress in machine learning and automating data acquisition which must become important in future synchrotron radiation experiments. Furthermore, from the perspective of social implementation of optical technology, we are continuing efforts to develop compact high-brightness light sources for medical applications and to put laser tunnel inspection technology into practical use.

KPSI will continue to fulfill our role as an open research center of the "science of light" and will contribute to quantum science and technology and the strategy for innovation in Japan. We appreciate your understanding and cooperation.

Good day, 2022
KAWACHI Tetsuya
Director General of KPSI

Activities of KPSI

関西光科学研究所の主な動き

【トピックス、シンポジウム・研究会の開催、等】

2021 年 4 月 7 日から 5 月 27 日

【QST 初！ クラウドファンディングによる研究開発】

　関西研（木津地区）のジェームズ・ケビン・コーガ博士が
提案した「レーザーで空気中のウイルスを検出できるか？」
について、クラウドファンディングによる研究支援を受け
ることができました。2021 年 4 月 7 日から 5 月 27 日の 1
か月間での目標金額：500,000 円に対して、支援総額：
684,029 円を得ることができました。研究成果については、
下記 URL を参照してください。

（日本語）https://academist-cf.com/projects/213?lang=ja

（英語）https://academist-cf.com/projects/213?lang=en

クラウドファンディング成功の画面
（アカデミスト Web サイト）

2021 年 6 月 22 日（火）

【光・量子ビーム科学合同シンポジウム 2021（OPTO 2021）開催】

　大阪大学と量研との間で締結された包括協定に基づき、合同シンポジウム（OPTO 2021）を開催致し
ました。年 1 回開催している合同シンポジウム
ですが、昨年に続き今年も会場および Web 配
信によるハイブリッド開催を行いました。参加
者は約 200 名で、大阪大学レーザー科学研究
所と量研関西研を中心に、欧州（ELI-BL）等、
海外からの Web 参加者もおられました。シン
ポジウムでは、招待講演・口頭発表、ポスター
発表を中心に若手ポスター賞表彰、大阪大学近
藤賞受賞記念講演、意見交換会が行われまし
た。

現地会場での参加者集合写真　2021 年 6 月 22 日

2021 年 10 月 31 日（日）

【関西光科学研究所（木津地区）　施設公開】

　10 月 31 日に関西研（木津地区）の施設公開を 2 年ぶりに開催しま
した。新型コロナウイルス感染予防対策のため、規模を縮小し、事前予
約制での開催とはなりましたが、100 名を超える方々にお越しいただ
きました。世界トップクラスの高強度レーザー施設の見学や、光の実
験ショー、工作教室等、ご来場いただいた皆様にはご好評をいただき
ました。

光の実験ショー
2021 年 10 月 31 日

2021 年 12 月 7 日（火）

【セルゲイ ブラノフ上席研究フェロー 外国人叙勲伝達式（チェコ共和国）】

功績概要:「科学技術分野における 日本の国際貢献の向上 に寄与」

　令和 2 年度（2020 年度）秋の叙勲において、量研の上席研究フェローである Sergey Bulanov 博士が、外国人叙勲（Conferment of Decorations on Foreign Nationals）を受章される栄誉に浴されました。新型コロナウイルス感染症拡大のために伝達式が 1 年程度遅れましたが、無事、チェコ共和国駐箚日本国特命全権大使 鈴木秀生閣下から褒章を授与されました。
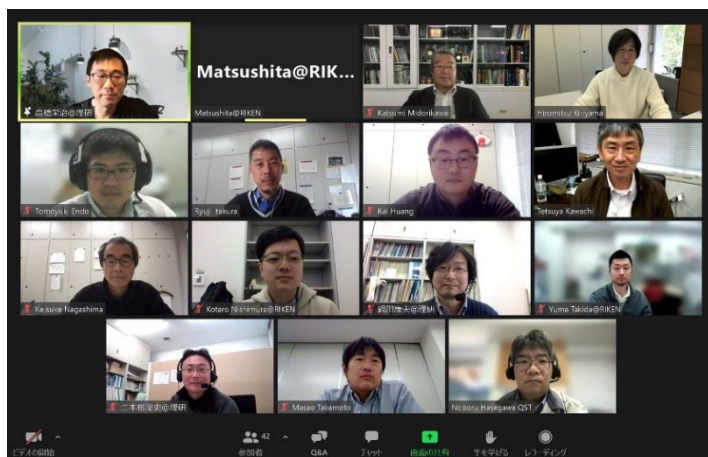

Bulanov 夫妻、鈴木秀生大使夫妻
2021 年 12 月 7 日　在チェコ日本国大使公邸

2022 年 2 月 4 日（金）

【第 5 回　理研光量子工学研究センター・量研関西光科学研究所合同セミナー」（Web 開催）】

　今回、第 5 回（5 年目）を迎えた本合同セミナーは昨年に続き、完全オンラインで開催されました。参加者は、昨年と同じ程度で常時 40 名以上が参加しました。講演内容は、最先端極短パルス光源開発からレーザー電子加速、分子や物性計測に加え、レーザーを利用した測地やトンネル検査などにおける幅広い領域にわたりました。

左）講演者リスト　　　右）Web 上での講演者・主催者集合写真　2022 年 2 月 4 日

2022 年 3 月 17 日（木）

【日本国駐箚ドイツ連邦共和国特命全権大使　Dr. Clemens von Goetze 閣下来所（視察）】

　関西研（木津地区）では、現在ヘルムホルツ研究機構との学術交流協定をむすび、レーザー加速や高強度場科学の国際協力を進めています。（ドイツ：ヘルムホルツ研究機構ドレスデン研究所、日本：大阪大学レーザー科学研究所および量研関西研）今回、日本国駐箚ドイ

関西研(木津地区)玄関、2022 年 3 月 17 日(木)

ツ連邦共和国特命全権大使 Dr. Clemens von Goetze 閣下が来所され、研究所の紹介、実験室見学、意見交換を行いました。今後の研究の進展が期待されています。

2022 年 3 月 28 日（月）
【QST 未来ラボ次世代放射光利用研究グループ 2021 年度公開ワークショップ】
　現在、量研は国の主体として、民間・地域パートナーとともに次世代放射光施設の整備・開発に取り組んでいます。QST 未来ラボ「次世代放射光利用研究グループ」は、量研が整備する 3 本の共用ビームラインを利用して、量子材料や量子生命科学といった量子戦略に関わる研究を行うための基盤を築くことを目的としています。本ワークショップでは「光電子分光と軟 X 線磁気分光の融合利用による量子マテリアルの研究」と題し、第一線で活躍する若手から中堅の 4 人の研究者による招待講演を含め、現状と将来展望について活発な議論が行われました。
https://www.qst.go.jp/site/kansai/aslws2021.html

【主な出展等イベント】

7 月 11 日～14 日 「第 21 回 SPring-8 夏の学校」開催（大型放射光施設 SPring-8、兵庫県佐用町）
11 月 1 日～13 日　けいはんな R&D フェア 2021 へ出展（Web 開催）
11 月 1 日～12 月 1 日　けいはんなビジネスメッセ 2021Virtual へ出展（Web 開催）

第 21 回 SPring-8 夏の学校ポスター

SPring-8 の QST ビームライン：
BL11XU 表面 X 線回折計での実習の様子

プレスリリース（研究成果）

1. 反強磁性モット絶縁物質におけるフェムト秒の電子スピン配列振動を発見
   — 超高速磁性ダイナミクスの探査手法を提案 —（2021 年 4 月 26 日）
   https://www.qst.go.jp/site/press/20210426.html
   論文タイトル：Antiphase Oscillations in the Time-Resolved Spin Structure Factor of a Photo-excited Mott Insulator

2. ヌクレオソーム中の H2A-H2B テイルの動的構造を解明（2021 年 7 月 5 日）
   https://www.qst.go.jp/site/press/20210705.html
   論文タイトル：N-terminal tails of histones H2A and H2B adopt two distinct conformations in the nucleosome with contact and reduced contact to DNA

3. 希少な元素を使わずにアルミニウムと鉄で水素を蓄える
   — 水素吸蔵合金開発の新たな展開を先導 —（2021 年 7 月 29 日）
   https://www.qst.go.jp/site/press/20210729.html
   論文タイトル：Hydrogen storage by earth-abundant metals, synthesis and characterization of $Al_3FeH_{3.9}$

4. レーザー中性子・X 線による同時瞬間撮影
   — 10 万分の 1 秒の短いパルスで可視光や X 線で見えなかった高速現象を撮る —（2021 年 9 月 16 日）
   https://www.qst.go.jp/site/press/20210916.html
   論文タイトル：Single shot radiography by a bright source of laser driven thermal neutrons and x-rays

5. 巨大負熱膨張のメカニズムを解明
   — さらなる新材料の設計に道を拓く —（2021 年 9 月 29 日）
   https://www.qst.go.jp/site/press/20210929.html
   論文タイトル：Origin and absence of giant negative thermal expansion in reduced and oxidized Ca_2RuO_4

6. 世界初！元素種を識別して材料のミクロ構造を解析するノイズ耐性の高い新解析法を開発
   — 将来的なデバイス材料のミクロ構造研究に活路を開く —（2021 年 12 月 11 日）
   https://www.qst.go.jp/site/press/20211211.html
   論文タイトル：Bayesian sparse modeling of extended X-ray absorption fine structure to determine interstitial oxygen positions in yttrium oxyhydride epitaxial thin film

7. 放射光を使った磁石の奥まで透ける顕微鏡
   — X線発光の新原理を用い開発に成功 —（2022 年 1 月 25 日）
   https://www.qst.go.jp/site/press/20220125.html
   論文タイトル：Bulk-sensitive magnetic microscope utilizing x-ray magnetic circularly polarized emission

8. 世界最強最薄ターゲットによるレーザーイオン加速の実現
   — グラフェンと超高強度レーザーが切り拓く極限世界 —（2022 年 2 月 16 日）
   https://www.qst.go.jp/site/press/20220216.html
   論文タイトル：Robustness of large-area suspended graphene under interaction with intense laser

9. 世界初の完全非破壊コンクリート遠隔打音検査手法を開発
   — コンクリート構造物のひび割れをレーザーで素早く視覚化 —（2022 年 2 月 22 日）
   https://www.qst.go.jp/site/press/20220222.html
   論文タイトル：Defect detection of concrete in infrastructure based on Rayleigh wave propagation generated by laser-induced plasma shock waves

10. 巨大タンパク質複合体による概日リズム制御
    — 小角散乱と計算科学の統合アプローチ —（2022 年 3 月 10 日）
    https://www.qst.go.jp/site/press/20220310.html
    論文タイトル：Overall structure of fully assembled cyanobacterial KaiABC circadian clock complex by an integrated experimental-computational approach

11. 世界初！放射線によって生じた DNA 損傷の直接観察に成功
    — 老化・がん治療研究にブレイクスルー —（2022 年 3 月 22 日）
    https://www.qst.go.jp/site/press/20220322-1.html
    論文タイトル：Formation of clustered DNA damage in vivo upon irradiation with ionizing radiation: Visualization and analysis with atomic force microscopy

User Facilities

主要な施設・装置

木津地区

○J-KAREN-P レーザー装置

【装置概要】

　世界トップクラスの極短パルス超高強度レーザーです。最大 30 J のレーザーエネルギーを 30 フェムト秒（1 フェムトは 1000 兆分の 1）の時間に閉じ込めることにより 1000 兆ワットの超高強度を実現します。（右の写真は強力な励起レーザーの光で緑色に光っています。）

【供給装置性能】
- 中心波長：810 nm
- 繰り返し：シングルショット〜0.1 Hz
- ターゲット照射エネルギー：〜10 J/pulse
- パルス幅：30~50 フェムト秒
- 集光強度：10^{20}〜10^{22} W/cm^2
- 時間コントラスト比：<10^{-11}　（プラズマミラー不使用時）
  　　　　　　　　　　　<10^{-13}　（シングルプラズマミラー使用時）
  　　　　　　　　　　　<10^{-15}　（ダブルプラズマミラーへアップグレード予定）

上記以外のパラメータもお問い合わせ下さい。

【主要な研究課題】

　超高強度レーザー高度化技術開発、イオンや電子の加速技術開発、高輝度 X 線等の量子ビーム源開発

○QUADRA-T レーザーシステム

【装置概要】

　1 秒間に 3000 発のレーザーパルスが繰り出せる高平均出力ピコ秒パルスレーザーです。

【装置性能】
- 照射エネルギー：10 mJ/pulse
- 波長：1030 nm
- 繰り返し：3 kHz
- パルス幅：約 1 ピコ秒
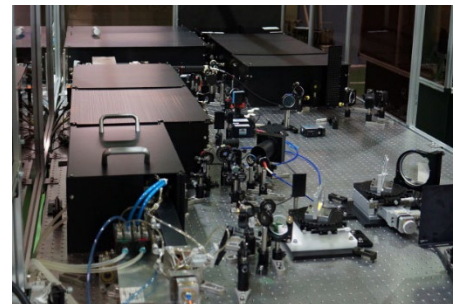
【主要な研究課題】

　高繰り返し高出力レーザー（パラメトリック増幅器等）の開発、高強度テラヘルツ光源の開発

播磨地区

播磨地区では大型放射光施設 SPring-8 に 2 本の QST 専用ビームラインを設置しているほか、日本原子力研究開発機構（JAEA）の専用ビームラインにも複数の放射光専用実験装置を常設しています。一方で、QST 専用ビームラインにも、JAEA の専用実験装置が常設されています。

○BL11XU（QST 極限量子ダイナミクス I ビームライン）

【装置概要】

SPring-8 標準の真空封止アンジュレータを光源とし、マルチ結晶交換システムを装備することで、広範囲のエネルギー領域の高輝度放射光 X 線を高効率に利用できるビームラインです。

【装置性能】
- ・光源：真空封止アンジュレータ
- ・エネルギー領域：6〜70 keV
- ・分光結晶：Si(111)、Si(311)
- ・実験装置：放射光メスバウアー分光装置、共鳴非弾性 X 線散乱装置、及び表面 X 線回折計

1. 放射光メスバウアー分光装置

^{57}Fe、^{61}Ni 等のメスバウアー核種を対象とした放射光メスバウアー分光が可能で、物質の電子、磁気状態から格子振動状態に関する情報などを得ることができます。更に、斜入射法や同位体置換試料を利用する事で、金属薄膜の表面部を原子層単位で測定する事も可能です。
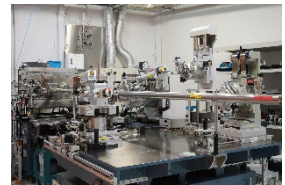

2. 共鳴非弾性 X 線散乱装置

入射 X 線、散乱（発光）X 線の双方のエネルギーを 0.1 eV 程度のエネルギーで分光実験が可能な装置です。4 軸回折計配置で共鳴非弾性 X 線散乱により電子励起の運動量依存性が測定できるほか、高エネルギー分解能 X 線吸収分光、X 線発光分光の実験も可能です。試料温度は 10 K から 800 K まで可変です。
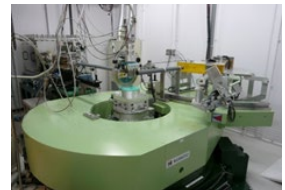
3. 表面 X 線回折計

分子線エピタキシー（MBE）チェンバーを搭載した表面構造解析用 X 線回折計です。半導体量子ドットや半導体多層膜などの成長過程を X 線回折によりその場観察・リアルタイム観察が可能です。2 台の MBE を交換し、GaAs、InAs などのヒ素化合物成長と RF-MBE による GaN、InN などの窒化物半導体成長を行うことができます。
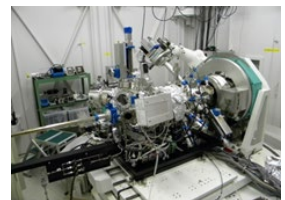
【主要な研究課題】

金属薄膜の原子層単位での磁性探査、遷移金属化合物における電荷・スピン・軌道励起の観測、触媒や電池電極材料のオペランド電子状態解析、半導体量子ドットや半導体多層膜の成長過程のリアルタイム解析

○BL14B1（QST 極限量子ダイナミクスⅡビームライン）

【装置概要】

　　偏向電磁石を光源とすることで、連続スペクトルを持つ白色Ｘ線や高エネルギーの単色Ｘ線が利用可能なビームラインです。全反射ミラーや分光結晶の曲げ機構によって、試料位置への集光が可能となっています。

【装置性能】

・光源：偏向電磁石

・エネルギー領域：白色Ｘ線（5〜150 keV）、単色Ｘ線（5〜90 keV）

・実験装置：高温高圧プレス装置、汎用四軸Ｘ線回折計及び分散型 XAFS 測定装置（JAEA）

　　1.　高温高圧プレス装置

　　10 GPa（13 万気圧）、2300 K 程度までの圧力・温度状態下の試料を、白色Ｘ線を用いたエネルギー分散型Ｘ線回折法やラジオグラフィー法、単色Ｘ線を用いた XAFS（X線吸収微細構造）法や角度分散型Ｘ線回折法等によって調べることができます。

【主要な研究課題】高圧下での金属水素化物形成過程のその場観察

　　2.　汎用四軸Ｘ線回折計

　　令和 2 年 3 月に RI 実験棟から移設。Ｘ線照射位置を可視化するためのレーザーを整備しており、がん研究等のための単色Ｘ線を利用した照射実験に使用できます。高エネルギー単色Ｘ線を利用した回折法により、大型構造材料中の応力・ひずみ、結晶方位分布計測の測定も可能です。

【主要な研究課題】応力・ひずみ、結晶方位の三次元分布測定、及び照射実験等

○BL22XU（JAEA 専用ビームライン）における放射光専用実験装置

　　1.　ダイヤモンドアンビルセル回折計（JAEA　BL22XU）

　　最高 70 keV の高エネルギーX線と大型二次元Ｘ線検出器の利用により最大 $Q = 27Å^{-1}$ までのＸ線全散乱プロファイルが迅速に得られ、約 100 Å までの距離相関の原子二体分布関数が導出できます。専用アタッチメントにより、室温、1 MPa 未満の水素と窒素ガス雰囲気でのその場観察ができます。試料·検出器間距離が可変のため高角データから高分解能データまで取得が可能であり、ダイヤモンドアンビルセルを用いた高圧力下Ｘ線回折測定にも適用可能です。

　　2.　大型Ｘ線回折計

　　Ｘ線領域のブラッグ反射を利用したコヒーレントＸ線回折イメージングが実施できる水平振りの大型Ｘ線回折計です。粒径 100 nm 以下のナノ結晶ひと粒のサイズや形状、内部構造（応力、ドメイン等）を含む3次元イメージングが可能です。

【主要な研究課題】

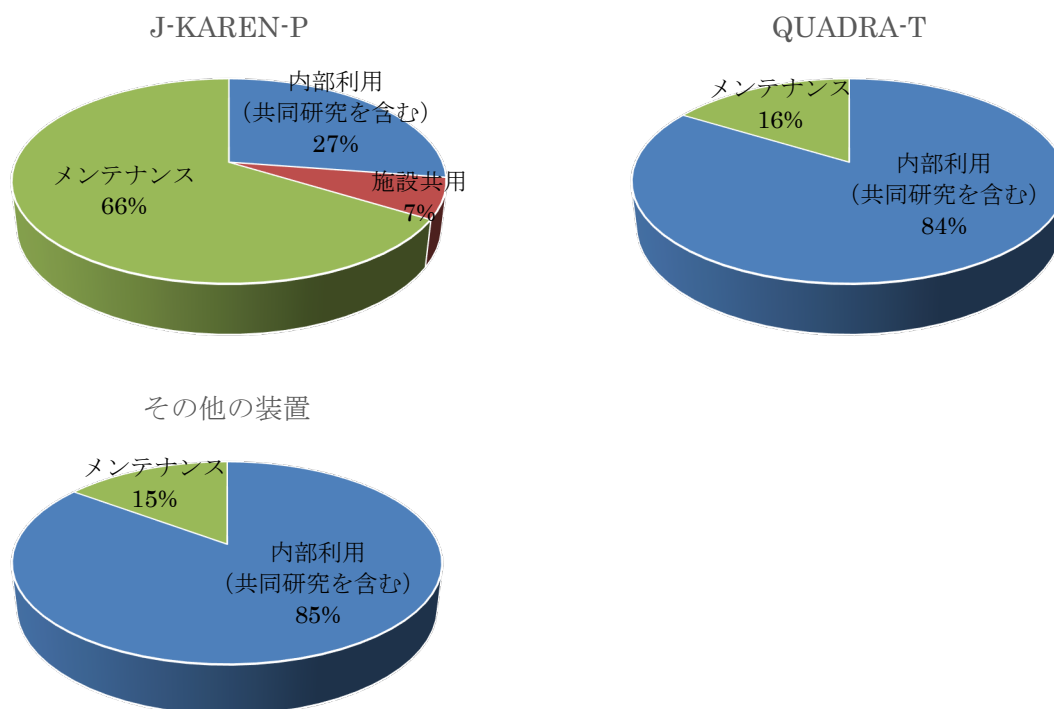　　水素貯蔵合金、負の熱膨張材料、100~500 nm 級チタン酸バリウムナノ結晶粒子一粒の3次元可視化、40 nm 級パラジウムナノ結晶粒子一粒の3次元可視化

施設の稼働実績と利用状況

木津地区

　2021 年度の運転時間は J-KAREN-P は 1826 時間、QUADRA-T は 1131 時間、その他装置は合計 1916 時間でした。J-KAREN-P は上期にコントラスト比を上げるためのプラズマミラー導入作業を行い、下期より利用研究を再開しました。

実施課題件数

装置名称	独自研究	受託研究	共同研究	施設共用
J-KAREN-P レーザー装置	2	1	0	1
QUADRA-T レーザーシステム	3	1	0	0
kHz チタンサファイアレーザー	6	1	1	0
X 線回折装置	1	0	1	0

稼働時間内訳

J-KAREN-P
内部利用（共同研究を含む）27%　施設共用 7%　メンテナンス 66%

QUADRA-T
メンテナンス 16%　内部利用（共同研究を含む）84%

その他の装置
メンテナンス 15%　内部利用（共同研究を含む）85%

播磨地区

　2021 年度の SPring-8 蓄積リングの運転時間は 5208 時間で、放射光利用時間はそのうちの 4440 時間でした。量研、JAEA とも専用ビームラインでは 10%程度の調整時間を除き、放射光利用時間で独自研究や受託研究、外部利用者への施設共用と研究支援を行っています。

実施課題件数

ビームライン	独自研究	受託研究	共同研究	施設共用
BL11XU	10	0	3	17
BL14B1	14	0	6	16
BL22XU	6	0	5	3

利用日数

ビームライン	独自研究	受託研究	共同研究	施設共用
BL11XU	95	0	13	56
BL14B1	58	0	21	53
BL22XU	38	0	27	13

　＊件数、日数ともに QST の利用のみ
　＊日数は 3 シフトを 1 日とした。

稼働時間内訳

QST極限量子ダイナミクスⅠビームライン（BL11XU)

QST極限量子ダイナミクスⅡビームライン（BL14B1)

JAEA重元素科学Ⅰビームライン（BL22XU)
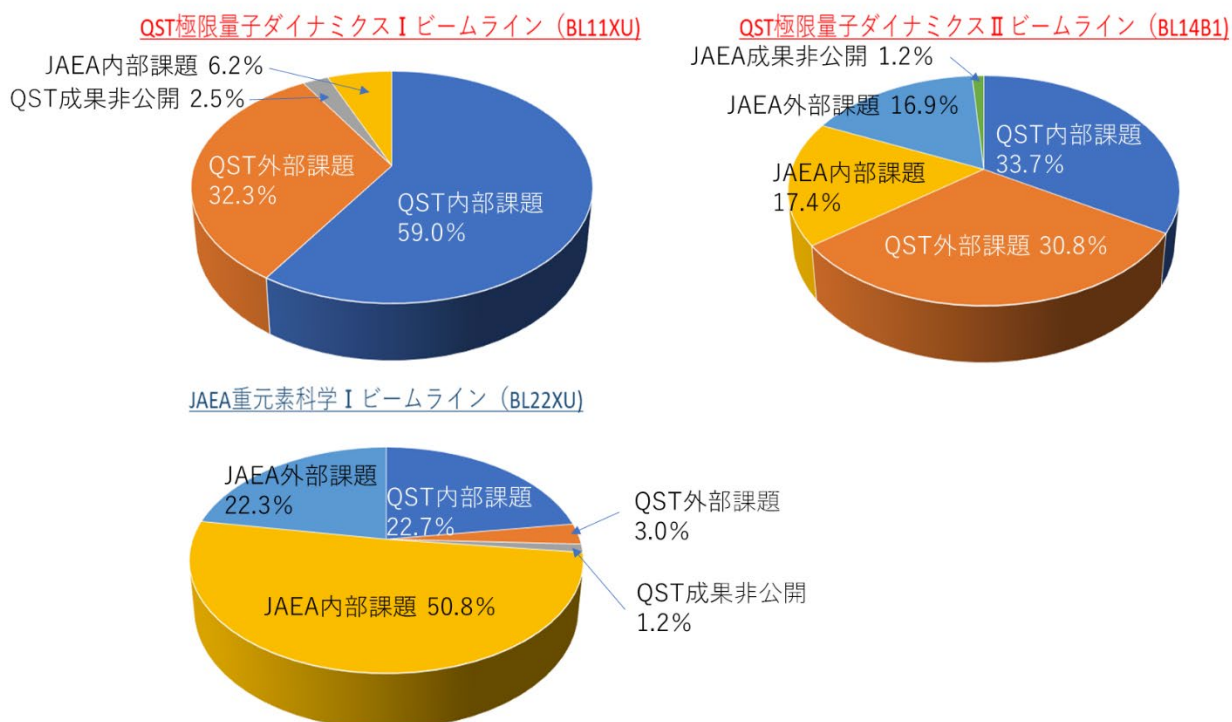
Research Highlights

Advanced Photon Research Activities

KONDO Kiminori

Department of Advanced Photon Research

The science and technology of advanced lasers are the foundation of the department of Advanced Photon Research. The advanced laser development is the basic part of this department. High-peak-power laser technology, high-repetition-rate and high-stability laser technology, and ultrashort-pulse technology are of particular importance. We develop these technologies in-house and apply them to various objects.

The largest laser system in KPSI is the petawatt (PW)-class high-peak-power J-KAREN-P laser. This system has been upgraded since FY2012 by obtaining a supplementary budget. After the long commissioning operation term, internal users in the KPSI and external users started to use this system in the PW-class operation mode. However, from the last fiscal year, we started to set a large plasma mirror system to avoid the rising part of the femtosecond high peak power pulse, which is a serious problem for laser-driven ion acceleration with a nanometer-scale thin foil target. This fiscal year, the machine time of J-KAREN-P for users began in September 2021. Until the middle of September, a large plasma mirror system was installed. Therefore, in the fiscal year 2021, only one theme was shared with external users, although 20 % of all user time was shared in FY2020. Although the user time of J-KAREN-P has declined drastically, the installation of the large plasma mirror system was completed in this fiscal year. Dr. Kon, from the high-intensity laser science group, reports this installation and shows the present performance. Moreover, some ion acceleration experiments, which have been proposed in FY2020 but have not been conducted due to Covid-19, have been conducted in this FY2021. They had the chance to use the extremely focused intensity of over 10^{21} W/cm^2 on targets with extremely high contrast, with the suppression of the leading optical component to the main pulse. Unfortunately, for the experimental application of this extreme laser-matter interaction, there is no article in this annual report. Currently, the data analysis is ongoing. We expect to show good results with the large plasma mirror system in the next annual report. This extreme status of our high-power laser infrastructure was maintained by the laser facility operation office, advanced laser group, and high-intensity laser science group. The advanced laser group not only maintained J-KAREN-P to deliver laser pulses with the best conditions but also developed and introduced new technology to maintain the world-leading class condition of J-KAREN-P. Dr. Miyasaka reported the development of a highly stable sub-nanosecond Nd:YAG pump laser, which will improve the synchronization between the pump and seed in OPCPA in the J-KAREN-P laser system. With this improvement, the stability of J-KAREN-P is expected to drastically improve.

The high-intensity laser science group has mainly studied laser-driven ion acceleration, laser electron acceleration, and relativistic high-order harmonic generation with J-KAREN-P in KPSI. One of the most important applications of this technology is the development of laser-driven quantum beams. An extremely high optical field can be formed by focusing an extremely high peak power on an ultimately small spot. The atoms and molecules exposed to this extremely high field were immediately ionized by field ionization. The corresponding optical intensity of the atomic unit was only 3×10^{16} W/cm^2, which is much lower than that generated with J-KAREN-P. The generated free electrons move along the extremely high optical field, inducing ultra-relativistic

Fig.1 Research and development of the department of Advanced Photon Research

quiver motion. These energetic quivering electrons induced the generation of various secondary radiations. This means that there is the possibility of a compact energetic quantum beam source without conventional accelerator technology. If this technology is established and applied to various fields, destructive innovation can occur. Dr. Fukuda et al., in the advanced laser group, reported energetic ion acceleration with a large-area suspended graphene target. Although the thickness of the graphene target was just a nanometer, this thin foil was irradiated by a high peak intensity J-KAREN-P laser pulse without using a plasma mirror device, and the energetic ions were detected. In the report, they explained what happened in this unique laser shot experiment. Normally, the extremely high peak intensity optical pulse has a high-intensity rising edge, which can break away a few-layer graphene thin foil. If so, there should be no chance of accelerating ions with such an extremely thin foil.

Although there are no precise reports in this annual report, one of the most important applications of laser-driven energetic particles is the application to the Quantum Scalpel, which is a new-generation heavy-ion cancer therapy machine. Quantum Scalpel is one of the main projects in QST. The injector part of the quantum scalpel is based on a laser-driven carbon accelerator. The JST-MIRAI R&D program (large-scale type) started in Nov. 2017. This program aims to demonstrate the proof of concept (POC) of a laser-plasma accelerator. In addition to an ion accelerator, a laser-plasma electron accelerator is also under development in KPSI within the MIRAI program. The POC of the laser-driven heavy ion injector must be demonstrated by the end of FY2026. In FY2020, the first-stage gate was successfully passed through, and FY2021 is in the second stage in JST-MIRAI. This year, the driver laser for generating a carbon-ion beam, which is the platform laser for developing the injector of Quantum Scalpel, has been upgraded to a double CPA 30 TW Ti:sapphire laser with a contrast ratio of 10^{10}. With this laser, up to 6th ionized carbon ions were observed, while only up to 4th ionized carbon ions were observed during the 1st stage in JST-MIRAI. The beamline for estimating the number of energetic carbon ions with a finite solid angle is estimated to be set in the ion acceleration platform by corroboration with the Sumitomo Heavy Industry. Moreover, using Hitachi Zosen, a repeatable special target system, with which carbon ions are generated, is currently being developed. Highly ionized energetic carbons are expected to be observed at 10 Hz in the near future.

Another important application of advanced laser science and technology is ultrafast probes for life and material science. The ultrafast dynamics group studied not only the basic science of ultrafast molecular behavior, but also developed a unique ultrafast high-power laser system. Until four years ago, the ultrafast dynamics group performed the C-Phost project. In this project, a kHz 10-mJ ps laser system, QUADRA-T, was developed. Recently, this system has been improved using a thin disk amplifier with a higher average power. Moreover, a mid-infrared high-average-power laser system is under development for starting attosecond experimental studies in KPSI. These laser systems will be used for laser fabrication and ultrafast laser science, which are studied in the Q-LEAP program at JST. Dr. Otobe reports a semi-classical theoretical approach for laser-metal interaction, which is important in the development of cyber physical system (CPS) laser fabrication in the Q-LEAP project. The ultrafast dynamics group also collaborated with the QST activity in quantum life science. An effective multiphoton microscope is under development for this purpose. In KPSI, a high-repetition-rate mid-infrared laser system with a high average power was developed for this microscope. Dr. Nagashima reported the development of a synchronously pumped OPO with a spatially dispersed beam, which has the potential of an MHz ultrashort high-average-power unique oscillator in the future. A related theoretical study of CPS laser fabrication was also conducted by the X-ray laser group. Dr. Yonetani reported a theoretical account of the calculation of long-range electrostatic interactions and studied on the interaction between DNA and radiation, which is included in the QST activity for quantum life science.

The most important application of our advanced laser science and technology is industrialization. The new SIP program, which follows the previous SIP program that was completed three years ago, began in the last year for the development of nondestructive tunnel inspection technology. This technology is being tested for its application in commercial technology at the venture company Photon-Labo. Non-destructive tunnel inspection is possible using laser hammering technology. This laser hammering technology is expected to be used not only for tunnel inspection abuts but also for various concrete structures. Dr. Hasegawa in the X-ray laser group reports on this study in an attempt to achieve social implementation.

Using high-power laser technology, a strong and compact infrared laser can be developed for various medical applications, including detecting blood glucose measurements. Dr. Akahane reported the development of a compact, high-energy Yb:YAG passive Q-switch laser, which can be used not only for detecting blood glucose measurements but also for pumping nonlinear processes.

Installing plasma mirror system at J-KAREN laser

KON Akira

High-Intensity Laser Science Group, Department of Advanced Photon Research

With the development of chirped pulse amplification technology invented in 1985 [1], research on high-intensity lasers has evolved for various applications [2]. In recent years, laser systems with an output power of more than 10^{20} W/cm^2 have been constructed in many countries worldwide owing to the development of high-energy and spatio-temporal control technologies by increasing the diameter of optical systems [3].

However, in laser-plasma experiments, target destruction owing to the pre-pulse becomes a problem as the focused intensity increases. The causes of the pre-pulse include amplified spontaneous emission, higher-order dispersion, clipping of the spectrum, scattering from the diffraction gratings, and nonlinear optical effects. These are so intricately intertwined that it is difficult to eliminate their causes.

To solve this problem, plasma mirrors (PMs) have been adopted in experimental facilities to improve temporal contrast [4, 5]. The PM's principle is that the main pulse is reflected by the self-generated plasma on the mirror substrate. However, because of the low intensity of the prepulse, a PM is not created, and most of it passes through the mirror substrate. Also, part of the prepulse is reflected by the anti-reflection (AR) coated mirror substrate surface (Figure.1).
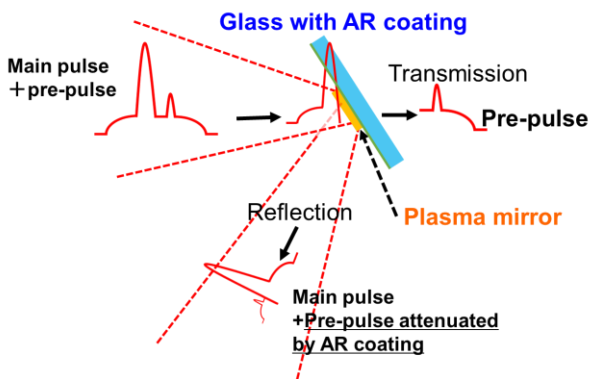

Figure.1 Principle of temporal contrast enhancement using PM

At the Kansai Photon Science Institute (KPSI), Quantum Science and Technology, the upgrade of the J-KAREN laser system and experimental area was completed in 2018 [6]. Also, in 2021 we installed a PM system to improve temporal contrast further for J-KAREN-P (1 PW, 0.1 Hz). Here, we report on the PM system installed at our facility and its performance [7].

As Figure 2 shows, the PM system was installed after the final compressor and before the target chamber. The vacuum chamber's size of the PM system (TOYAMA Co., Ltd.) was 2.1 m × 2.7 m × 2.3 m. The internal components consisted of two periscope pairs, two OAP mirrors, and a PM substrate. The mirror holders of periscopes were the ANTARES series made by LIOP-TEC GmbH, and the driving mechanism was a piezo actuator (Physik Instrumente GmbH & Co. KG). The OAP (TYDEX.

LLC) had a focal length of 2 m (F/8) and a wavefront accuracy of λ/10 (P-V) at 633 nm. The setup was a "single" PM (see Figure 1). The PM substrate's size was 400 mm × 70 mm × 30 mm, and the laser was incident on the mirror with S polarization at an incident angle of 16°. The reflectance of the AR coating on both sides was <1% at 770-830 nm, 16°, and there were silver-coated areas on the top, bottom, and center for alignment. The PM was placed on an automatic stage (Kohzu Precision Co., Ltd) for XYZ and θx. The mirror was moved for each shot by a drive stage of ±250 mm in the vertical direction and ±35 mm in the horizontal direction. This PM system could be used for ~1,000 shots at 1 Hz without replacing the mirror.
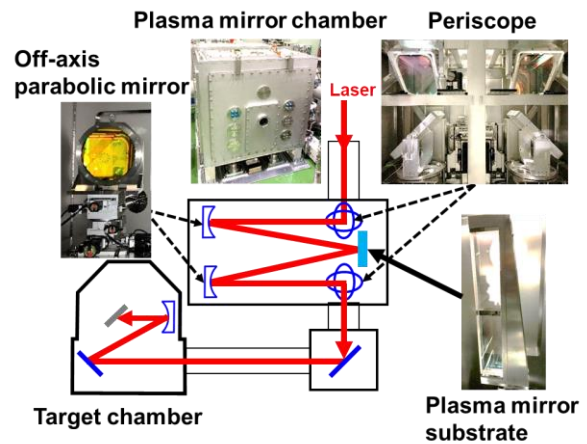

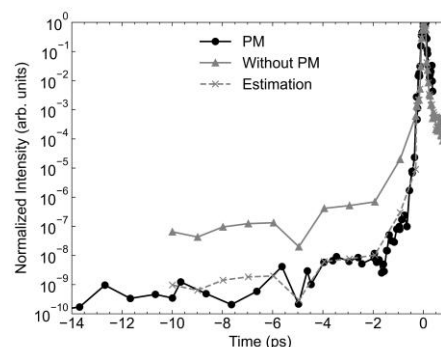Figure.2 Plasma mirror system at J-KAREN-P

Figure.3 Temporal contrast with and without PM system

Temporal contrast was measured using a third-order cross-correlator [8] (SEQUOIA, Amplitude Technologies). The performance of the temporal distribution was measured using light picked off from a full beam with a diameter of 25.4 mm.

Figure 3 shows the results obtained with and without the PM system. From -10 ps to several hundred femtoseconds, the contrast improved by approximately 100. The trigger time for the PM was expected to be -0.9 ps to -0.3 ps from Figure.3. The dotted line in Figure 3 shows the predicted results without a PM, considering the reflectivity of the PM (65%) and AR coating (1%). The estimated and measured results correlated. However, the temporal contrast could be further improved by one to two orders of magnitude by optimizing the AR coating [9].

The reflectivity of the PM system was calculated using an energy-calibrated charge coupled device after the final stage amplification and an absolutely calibrated integrating sphere and spectrometer after the PM for each shot. In the experiment, reflectance data were obtained when the fluence was varied by changing the distance of the OAP to the PM and laser energy. Figure 4 shows the PM system's reflectivity results. The reflectivity increased as the fluence increased, reaching 85% at a fluence of approximately 100 kJ/cm^2.

We reported on the configuration and performance of a single PM system installed in the J-KAREN laser system. In future, we plan to conduct experiments using high-contrast lasers (e.g., ion acceleration). Subsequently, we will upgrade to a double PM and adopt a deformable mirror after the compressor to upgrade the laser system.
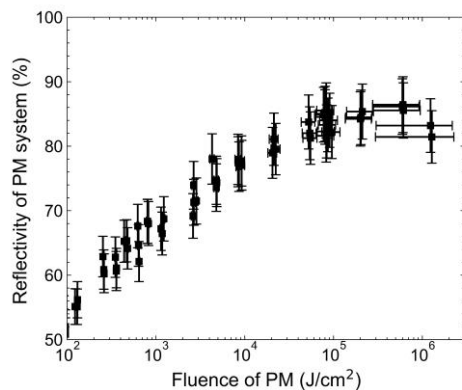

Figure.4 Reflectivity of PM system

References
1. D. Strickland and G. Mourou, Optics Communications 56, 219 (1985).
2. G. A. Mourou, T. Tajima, and S. V. Bulanov, Reviews of Modern Physics 78, 309 (2006).
3. C. N. Danson, C. Haefner, J. Bromage, T. Butcher, J.-C. F. Chanteloup, E. A. Chowdhury, A. Galvanauskas, L. A. Gizzi, J. Hein, D. I. Hillier, N. W. Hopps, Y. Kato, E. A. Khazanov, R. Kodama, G. Korn, R. Li, Y. Li, J. Limpert, J. Ma, C. H. Nam, D. Neely, D. Papadopoulos, R. R. Penman, L. Qian, J. J. Rocca, A. A. Shaykin, C. W. Siders, C. Spindloe, S. Szatmári, R. M. G. M. Trines, J. Zhu, P. Zhu, and J. D. Zuegel, High Power Laser Science and Engineering 7, e54 (2019).
4. H. C. Kapteyn, A. Szoke, R. W. Falcone, and M. M. Murnane, Optics Letters 16, 490 (1991).
5. G. Doumy, F. Quéré, O. Gobert, M. Perdrix, P. Martin, P. Audebert, J. C. Gauthier, J. -P. Geindre, and T. Wittmann, Physical Review. E 69, 026402 (2004).
6. H. Kiriyama, A. S. Pirozhkov, M. Nishiuchi, Y. Fukuda, K. Ogura, A. Sagisaka, Y. Miyasaka, M. Mori, H. Sakaki, N. P. Dover, K. Kondo, J. K. Koga, T. Z. Esirkepov, M. Kando, and K. Kondo, Optics Letters 43, 2595 (2018).
7. A. Kon, M. Nishiuchi, Y. Fukuda, K. Kondo, A. Ogura, Y. Sagisaka, N. P. Miyasaka, M. Dover, A. Kando, S. Pirozhkov, I. Daito, L. Chang, I. W. Choi, C. H. Nam, T. Ziegler, H.-P. Schlenvoigt, K. Zeil, U. Schramm, and H. Kiriyama, "Characterization of plasma mirror system at J-KAREN-P facility" submitted to High Power Laser Science and Engineering, Feb. 2022.
8. S. Luan, M. H. R. Hutchinson, R. A. Smith, and F. Zhou, Measurement Science and Technology 4, 1426 (1993).
9. S. Inoue, K. Maeda, S. Tokita, K. Mori, K. Teramoto, M. Hashida, and S. Sakabe, Applied Optics 55, 5647 (2016).

Energetic ion acceleration by direct irradiation of ultra-intense laser on large-area suspended graphene

KURAMITSU Yasuhiro[1], WOON Wei-Yen[2], KANASAKI Masato[3], KIRIYAMA Hiromitsu[4], FUKUDA Yuji[4]

Kuramitsu Y.

Fukuda Y.

[1] *Graduate School of Engineering, Osaka University, Japan*
[2] *Department of Physics, National Central University, Taiwan*
[3] *Graduate School of Maritime Sciences, Kobe University, Japan*
[4] *Advanced Laser Group, Department of Advanced Photon Research, QST-KPSI, Japan*

Atomically thin graphene is transparent, highly electrically and thermally conductive, lightweight, and the strongest material. To date, graphene has been used in many applications, including transport, medicine, electronics, energy, defense, and desalination. In this paper, we report another disruptive application of graphene in laser-ion acceleration, in which the unique features of graphene play a crucial role. Osaka University researchers, in collaboration with researchers at the National Institute for Quantum Science and Technology (QST), Kobe University, and National Central University in Taiwan, have demonstrated direct energetic ion acceleration by irradiating the world's thinnest and strongest graphene target using an ultra-intense J-KAREN-P laser at the Kansai Photon Science Institute, QST [1].

Recent developments in laser technology have enabled us to access the radiation regime of laser-ion acceleration with relatively thin targets. However, a thinner target is less durable than a thicker target and can be easily broken by a pedestal or pre-pulse through impact and heating before arriving at the main laser. A possible solution to this problem is to use a plasma mirror, which is a surface plasma produced by the foot of the laser pulse on an optically transparent material that functions as an effective mirror only for the main laser peak. Thus far, diamond-like carbon (DLC) has been used to enhance ion acceleration in an extremely thin target range (< 10 nm) with plasma mirrors. It is necessary to use plasma mirrors, even in a moderately thin target range (10–100 nm), to realize energetic ion generation. However, DLC is not a two-dimensional (2D) material; therefore, it is costly to make it thin and flat. Moreover, graphene is stronger than diamond in an extremely thin region and is more suitable for mass production. Furthermore, installing and operating plasma mirrors at a high repetition rate is expensive. In this study, we investigated another direct solution using graphene as the thinnest and strongest target ever made. We developed a facile transfer method to fabricate large-area suspended graphene (LSG) as a target for laser-ion acceleration with precision down to a single atomic layer [2]. Direct irradiation of LSG targets with an ultra-intense laser generates energetic carbons and protons, demonstrating the durability of graphene without a plasma mirror. This application extends the new frontier of graphene science in extreme electromagnetic fields, such as energy frontiers and nuclear fusion.

Experiments were performed using J-KAREN-P at QST-KPSI [3], where the laser intensity reaches the highest class curr-
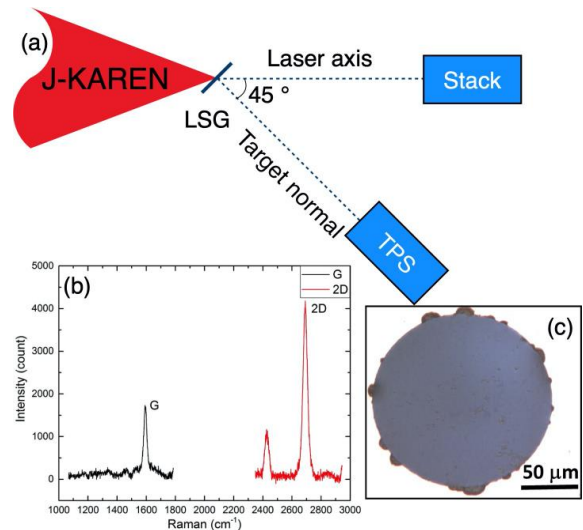

Fig. 1. (a) Schematic of experimental setup with large-area suspended graphene target (LSG). (b) Raman spectrum and (c) optical microscopic images for typical LSG, respectively.

ently available worldwide. Fig. 1(a) shows schematic images of the experimental setup. Fig. 1(b) and (c) show the Raman spectrum and optical microscopic images of a typical LSG, respectively. Here, the narrow bandwidth of the 2D band (< 30 cm^{-1}) and the higher intensity ratio (> 2.5) of the 2D and G bands (I[2D]/I[G]) confirmed the presence of a single-layer LSG. The small peak next to the 2D peak comes from the slight curvature of the LSGlower owing to the high aspect ratio of the LSG. We placed the convex and concave sides of the laser and detector, respectively, to achieve improved beam collimation. The ideal LSG was 0.34 nm, whereas the obtained transferring graphene was close to 1 nm because of the molecular adsorption on the surface [2]. By transferring the graphene layer by layer, we controlled the target thickness with 1 nm accuracy.

The J-KAREN-P laser was focused with an F/1.3 off-axis parabolic mirror on the LSG from 45° to the target normal direction to prevent the back reflection of incident light and destroy the upstream optics without a plasma mirror. The pulse

energy, duration, focal spot, and intensity were ~10 J on the target, 40 fs, ~2 μm, and ~5×10^{21} Wcm^{-2}, respectively, and measured immediately before the experiment. Energetic ion beams were produced by irradiating the LSGs with intense lasers. The accelerated ions were detected using a stack of radiochromic films, a solid-state nuclear track detector (CR-39), and a Thomson parabola spectrometer (TPS). When a solid target was irradiated with an intense laser, a proton beam was generated independently of the target material, owing to surface contamination from moisture in the air. CR-39s enable us to distinguish heavier ions and mostly carbons from protons based on the size of ion pits [4]. Furthermore, TPS provides the charge-to-mass ratio and the energy spectra.
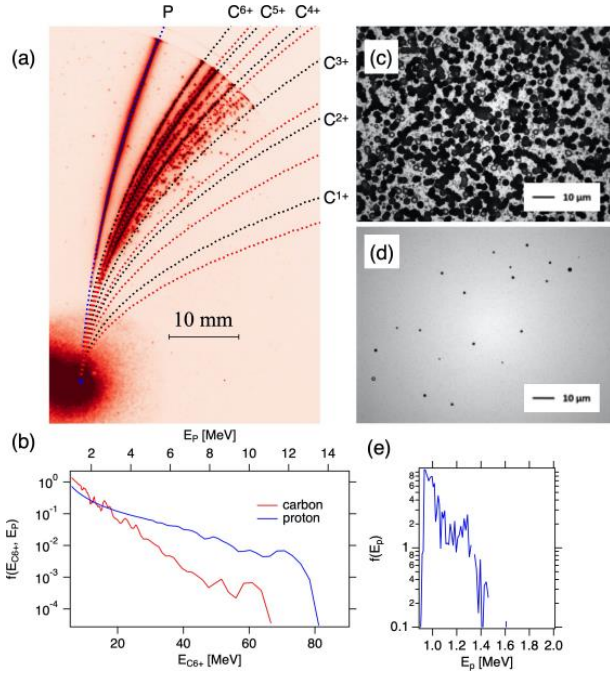

Fig. 2. (a) Image captured using TPS with eight-layer LSG, where a micro-channel plate and a charged-couple device were used as detectors. The black and green parabolae correspond to carbon and oxygen ions, respectively. (b) Energy distribution functions calculated from (a) for proton and C^{6+}. (c) Carbon pits on first CR-39 covered with a 12 μm aluminum foil with energy of 12−94 MeV. (d) Proton pits on CR-39 behind aluminum foil, two RCFs, and CR-39 corresponding to the energy of 12.2 − 13.2 MeV. (e) Proton energy distribution function obtained using two-layer LSG.

Figure 2 shows the results for an eight-layer LSG, that is, an 8 nm thick target with the full energy of J-KAREN-P at the best focus. In Fig. 2(a), the raw TPS data are represented by blue, black, and red dotted lines corresponding to the protons, carbon ions, and oxygen ions, respectively. Figure 2(b) shows the proton and carbon energy distribution functions f(E$_{P,C}$), where E$_{P,C}$ are the proton and C^{6+}, respectively, after subtracting the background. Approximately 30% of the oxygen ions were also present. The ion spectra showed bump-on-tail or monoenergetic features in higher-energy tails. When the proton and carbon were accelerated by the same potential field, which occurred in typical laser-ion acceleration, the carbon energy was six times higher than that of the proton because of the difference in the charge-to-mass ratio. The experimental results showed that the proton energy was slightly higher than 1/6 of the carbon energy. Figure 2(c) and (d)

show the etched pits of mostly carbons and protons, respectively, which are consistent with the TPS. Figure 2(e) shows the same plot as Fig. 2(b), except for the double-layer LSG corresponding to a thickness of 2 nm. This image was captured under a different condition in which the laser incident angle was 10° with a moderate contrast level of ~10^{-7}. For the eight-layer LSG shot, the contrast level was ~10^{-10} or lower

As mentioned above, the pre-pulse and pedestal are significant practical problems in the extremely thin target region. Recent experiments have utilized single- or double-plasma mirrors to suppress the pre-pulse and pedestal and achieve energetic ion acceleration. Surprisingly, energetic ions are generated by irradiating single-figure-nanomer thin targets with an ultra-intense laser at ~10^{22} Wcm^{-2} without a plasma mirror. Our double-layer LSG is the thinnest target that generates energetic ions, even without a plasma mirror at this thickness.

In conclusion, the results of this study apply to the development of compact and efficient laser-driven ion accelerators for cancer therapy, laser nuclear fusion, high-energy physics, and laboratory astrophysics. The direct acceleration of energetic ions without a plasma mirror demonstrates the robustness of the LSG. We will use atomic-thin LSG as a target mount to accelerate other materials that cannot stand without support. We also demonstrated energetic ion acceleration at non-relativistic intensity (not discussed here). This research will help us investigate laser-ion acceleration using relatively small laser facilities. Furthermore, energetic ion acceleration was achieved even without a plasma mirror in the extremely thin target region, thus, opening a new region for laser-driven ion acceleration.

Acknowledgments

References

1. Y. Kuramitsu, T. Minami, T. Hihara, K. Sakai, T. Nishimoto, S. Isayama, Y.T. Liao, K.T. Wu, W.Y. Woon, S.H. Chen, Y.L. Liu, S.M. He, C.Y. Su, M. Ota, S. Egashira, A. Morace, Y. Sakawa, Y. Abe, H. Habara, R. Kodama, L. N. K. Dohl, N. Woolsey, M. Koenig, H. S. Kumar, N. Ohnishi, M. Kanasaki, T. Asai, T. Yamauchi, K. Oda, Ko. Kondo, H. Kiriyama, Y. Fukuda, Robustness of large-area suspended graphene under interaction with intense laser, accepted for publication in Scientific Reports.
2. N. Khasanah, N. Bolouki, T.-Y. Huang, Y.-Z. Hong, W.- L. Chung, W.-Y. Woon, C.-Y. Su and Y. Kuramitsu, Large-area suspended graphene as a laser target to produce an energetic ion beam, High Power Laser Sci. Eng. **5**, e18 (2017).
3. H. Kiriyama, Y. Miyasaka, A. Sagisaka, K. Ogura, M. Nishiuchi, A. S. Pirozhkov, Y. Fukuda, M. Kando, and K. Kondo, High-contrast high-intensity repetitive petawatt laser. Opt. Lett. **43**, 2595 (2018).
4. T. Hihara, M. Kanasaki, T. Asai, T. Kusumoto, S. Kodaira, H. Kiriyama, K. Oda, T. Yamauchi, W. Y. Woon, Y. Kuramitsu, and Y. Fukuda, Discriminative detection of laser-accelerated multi-MeV carbon ions utilizing solid state nuclear track detectors, Sci. Rep. **11**, 16283 (2021).

Sub-nanosecond Nd:YAG pump laser for optically synchronized optical parametric chirped-pulse amplification

MIYASAKA Yasuhiro

Advanced Laser Group, Department of Advanced Photon Research

The J-KAREN-P laser, which is the petawatt-class femtosecond laser system developed in the Kansai Photon Science Institute (KPSI), achieves a high pulse contrast of 10^{12} by combining optical parametric chirped-pulse amplification (OPCPA) as a pre-amplifier and subsequent Ti:sapphire amplifications [1]. In the current J-KAREN-P laser, the timing jitter between the pump and seed pulses for the OPCPA is ~100 ps, because the two oscillators for the pump and seed lasers are electrically synchronized with a commercially available pulse delay generator. Reducing the timing jitter improves the stability of the output pulse conditions of the J-KAREN-P laser to achieve higher-quality experiments. Teisset et al. developed an optical synchronization scheme with a single oscillator by generating pump pulses from a portion of the signal pulses to reduce timing jitter [2]. A timing jitter of less than 400 fs is realized by optically synchronized pumping; however, the pulse duration reported to date is too short for our purpose. To use the optically synchronized pump pulses for the OPCPA in the J-KAREN-P laser, a long pulse duration is required because the pulse duration of the signal pulses is stretched to ~1ns to avoid optical damage in the subsequent Ti:sapphire amplifiers. A frequency-doubled Nd:YAG laser was used for OPCPA pumping in the J-KAREN-P laser because of the efficient laser operation at room temperature without complex cooling systems. The longest pulse duration of an optically synchronized Nd:YAG laser was reported to be 207 ps [3]. Herein, we report the development of a highly stable optically synchronized frequency-doubled Nd:YAG pump laser. Pulse durations of 600 ps at 1064 nm and 490 ps at 532 nm were obtained by optimizing the Nd:YAG crystal temperature [4].

Figure 1 shows the schematic of the proposed optically synchronized pump laser. All components were set on a water-cooled optical table to minimize the temperature effects. The laser comprised a Ti:sapphire oscillator, fiber systems for stable chirped-seed pulse generation at a wavelength of 1064 nm, bulk amplifier systems for high-energy amplification, and a frequency doubler. Pulses from a Ti:sapphire oscillator were focused on a 23 cm photonic crystal fiber to extend the spectrum to include 1064 nm. Polarizing the input pulses was controlled by a feedback control system composed of a spectrometer and half-wave plate mounted on a motorized rotation stage to stabilize the output spectrum at 1064 nm. The stabilized pulses were amplified to 130 mW (rms: 0.2 %) by four Yb-doped fiber amplifiers and
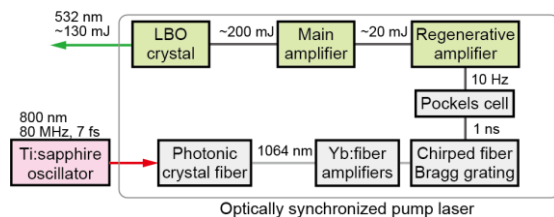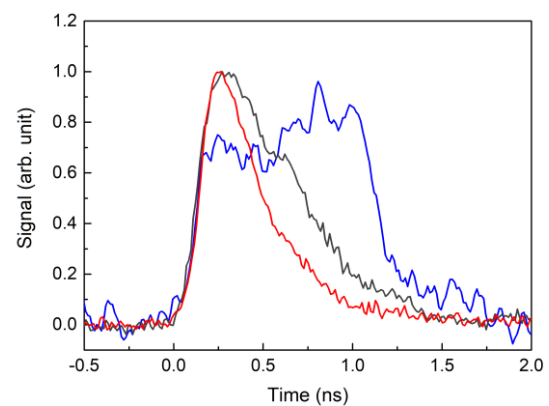

Fig. 2. Measured pulse shapes before passing through the

stretched to 1 ns by a chirped Bragg fiber grating. The repetition rate of the fiber output pulses was reduced from 80 MHz to 10 Hz using a Pockels cell for subsequent amplifications with a diode-pumped Nd:YAG regenerative amplifier and a two-pass main amplifier. The regenerative amplifier was designed to set a beam diameter of ~2 mm on a 6 mm diameter Nd:YAG rod to avoid Fresnel diffraction from the rod edge. With 10 round trips, the pulses were amplified to 20 mJ (RMS: 0.3%) with a beam diameter of 2.3 mm. The amplified pulses were expanded to a diameter of 4 mm before injecting into the main amplifier. A serrated aperture of 5 mm diameter was placed after the beam expander to avoid optical damage induced by Frenel diffraction at the 8 mm diameter Nd:YAG rod in the main amplifier. A pulse energy of 200 mJ was achieved with excellent stability of better than 0.2% (rms). The amplified pulses' frequency was doubled in an LBO crystal with a length of 13 mm. A pulse energy of 130 mJ with a stability of 0.6% (rms) at a wavelength of 532 nm was obtained, with a conversion efficiency of 64%. The pulse duration after frequency doubling was shortened to 330 ps; whereas, the pulse duration before regenerative amplification was 1 ns. Fig. 2 shows the measured pulse shapes before and after the regenerative amplifier with a 30 GHz oscilloscope. The pulse duration after applying the regenerative amplifier was 360 ps. The pulse duration decreased as the number of round trips in the regenerative amplifier increased.We investigated the phenomenon of pulse shortening owing to the pulse shape distortion behavior of high-gain chirped-pulse amplification in a regenerative amplifier. Assuming a single value of stimulated emission cross-section for chirped pulse amplification in a regenerative amplifier, a pulse duration of more than 850 ps was calculated using the Frantz-Nodvik equation [5]. The difference between the experimental and calculation results was derived from the wavelength dependence of the stimulated emission

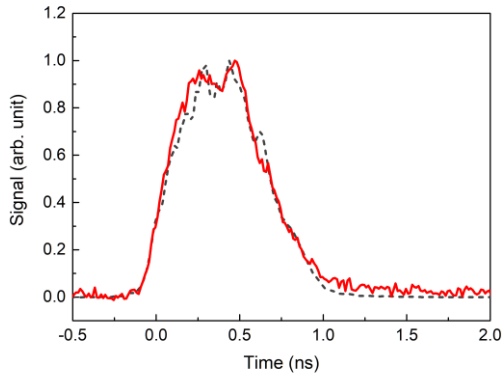Fig. 1. Diagram of our optically synchronized pump laser.

Fig. 3. Measured (solid line) and calculated (dashed line) pulse shapes after the regenerative amplifier.

cross-section [6]. The temperature dependence and narrow bandwidth of the stimulated emission cross-section of the Nd:YAG crystal affected pulse shortening. In this experiment, the Nd:YAG crystal was cooled with water at 18°C. The dashed line in Fig. 3 shows the calculated pulse shape after regenerative amplification at a rod temperature of 31.5°C. The pulse duration was increased to 620 ps because the wavelength of the peak cross section shifted to the spectrum peak of the chirped pulse. To confirm this effect experimentally, we measured the amplification at a cooling-water temperature of 31°C. The solid line in Fig. 3 shows the pulse shape after regenerative amplification. The pulse duration was extended to 600 ps, which agreed with the calculation results. After the main amplification, the pulse duration was reduced to 540 ps. Therefore, we considered the pulse shortening to be due to the gain narrowing caused by the decrease in stored energy when the latter part of the pulse was amplified. The pulse duration after doubling was 490 ps. A longer pulse duration will be achieved using a chirped fiber Bragg grating with a higher group velocity dispersion and a lower bandwidth. The increase in the chirp rate of the incident pulse enabled the regenerative amplifier to generate a longer pulse for the optically synchronized OPCPA in the J-KAREN-P laser.

References

1. H. Kiriyama, Y. Miyasaka, A. Kon, M. Nishiuchi, A. Sagisaka, H. Sasao, A. S. Pirozhkov, Y. Fukuda, K. Ogura, K. Kondo, N. P. Dover, M. Kando, "Enhancement of pre-pulse and picosecond pedestal contrast of the petawatt J-KAREN-P laser," High Power Laser Science and Engineering 9, e62 (2021).
2. C. Y. Teisset, N. Ishii, T. Fuji, T. Metzger, S. Köhler, R. Holzwarth, A. Baltuška, A. M. Zheltikov, and F. Krausz, "Soliton-based pump-seed synchronization for few-cycle OPCPA," Optics Express 13(17), 6550–6557 (2005).
3. A. Vaupel, N. Bodnar, B. Webb, L. Shah, M. Hemmer, E. Cormier, and M. Richardson, "Hybrid master oscillator power amplifier system providing 10 mJ, 32 W, and 50 MW pulses for optical parametric chirped-pulse amplification pumping," Journal of the Optical Society of America B 30(12), 3278–3283 (2013).
4. Y. Miyasaka, K. Kondo, and M. Kishimoto, M. Mori, M. Kando, H. Kiriyama, "Highly stable sub-nanosecond Nd:YAG pump laser for optically synchronized optical parametric chirped-pulse amplification," Optics Express 29(20), 32404–32411 (2021).
5. L. M. Frantz and J. S. Nodvik, "Theory of pulse propagation in a laser amplifier," Journal of Applied Physics 34(8), 2346–2349 (1963).
6. Y. Sato and T. Taira, "Temperature dependencies of stimulated emission cross section for Nd-doped solid-state laser materials," Optical Materials Express 2(8), 1076 (2012).

Synchronously pumped optical parametric oscillator with a spatially dispersed beam

NAGASHIMA Keisuke

Ultrafast Dynamics Group, Department of Advanced Photon Research

Synchronously pumped optical parametric oscillator (SPOPO) is a conventional apparatus used for wavelength-tunable infrared light sources [1–3]. Periodically poled materials have been used in several SPOPO experiments because these materials provide several advantages such as high nonlinear coefficients and lack of spatial walk-off [4-6]. In addition, they have a significant advantage that various structures with different poling periods can be flexibly designed [7]. Furthermore, structures with chirped or fan-out poling periods have been developed [8-10].

Chen et al. proposed a method for an optical parametric amplifier (OPA) using a fan-out type poled device [11]. In this method, broadband phase matching was achieved by adjusting the fan-out poling period and the spatially dispersed beam. The frequency-domain OPA is a similar method that uses a spatially dispersed beam [12]. In this study, the demonstration of a broadband SPOPO is presented using a fan-out type poled device and a spatially dispersed beam [13].
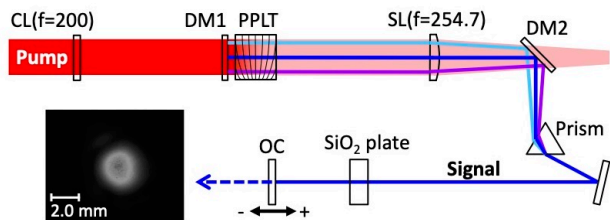

Fig. 1. Optical layout of the SPOPO. It consists of components such as spherical lens (SL), cylindrical lens (CL), periodically poled LiTaO$_3$ (PPLT), dichroic mirrors (DM1 and DM2) that reflect only the signal light, and an output coupler (OC) with a signal light transmittance of 50%. The inset depicts the output signal beam profile measured at a distance of 1.7 m from the OC.

An Yb-doped fiber laser was used as the pump source for the SPOPO. The laser had a repetition frequency of 43.3 MHz, central wavelength of 1038 nm, full-width at half-maximum (FWHM) pulse length of 390 fs, and a maximum pump power of 14 W. Fig. 1 shows the optical layout of SPOPO. This layout was similar to that used in a previous study [14]. MgO-doped periodically poled LiTaO$_3$ (MgO:PPLT) was used as the nonlinear material. The output coupler (OC) had a constant transmission rate of 50% in the frequency range of 1300 – 1700 nm. The cavity length was 3.46 m, which corresponded to the repetition frequency of the pump laser. Flat mirrors were used in the cavity for dichroic mirrors (DM1 and DM2) and the OC. Only one spherical lens was used in the cavity. The spherical lens was made of CaF$_2$ with a broadband anti-reflection (AR) coating and it had a focal length of 254.7 mm for a wavelength of 1580 nm.

An N-SF11 glass equilateral prism was installed in the cavity. Fig. 2 shows the details of the fan-out type MgO:PPLT and the spatially dispersed beam. The prism had an AR coating for the wavelength range of 1500 – 1700 nm when the S-polarization light was incident at an angle of 60.6°. The prism generated an angular dispersion of $\Delta\theta/\Delta\lambda$. The spatial displacement at the

spherical lens was $\Delta X/\Delta\lambda = f\Delta\theta/\Delta\lambda = 9.3 \times 10^{-3}$ mm/nm, where f is the focal length. In Fig. 2, the three lines represent signal beam axes with different wavelengths. The beams were parallel between DM1 and the spherical lens, and coaxially overlapped between the prism and OC.
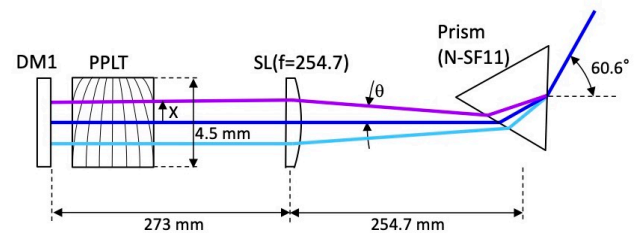

Fig. 2. Details of the fan-out type MgO:PPLT and the spatially dispersed beam.

The nonlinear crystal was 1 mol% MgO-doped stoichiometric PPLT (manufactured by OXIDE). The crystal had a broadband AR coating in the range of 1000 – 1700 nm and it had a length (Z-direction), height, and width (X-direction) of 10, 2, and 6 mm, respectively. The effective width was 4.5 mm, where the poling period had a nonlinear fan-out structure and it varied in the range of 28.6 – 32.4 μm. Fig. 3(a) shows the relationship between the position X in the MgO:PPLT and the poling period. The fan-out structure was designed to exhibit a linear relationship between horizontal position (X) and the signal wavelength, as shown in Fig. 3(b). The slope of the linear relation was $\Delta X/\Delta\lambda = 9.24 \times 10^{-3}$ mm/nm, which was equal to the value obtained by the prism dispersion.
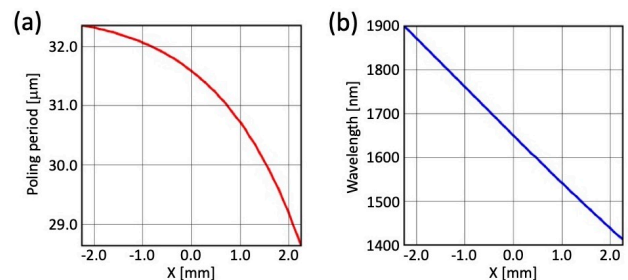

Fig. 3. (a) Poling period of MgO:PPLT as a function of the horizontal position (X). (b) Signal wavelength that satisfies the phase-matching condition as a function of X.

The spectral dispersion in the cavity was dominated by the dispersion of the transmission materials (MgO:PPLT, CaF$_2$, and N-SF11 glass). The thickness of the CaF2 lens was 2.7 mm and the pass length in the N-SF11 prism was approximately 8 mm. The GDD values were 567, -3.7, and, 246 fs^2 for MgO:PPLT, CaF$_2$, and N-SF11, respectively. Therefore, the total GDD was 809 fs^2. This spectral dispersion was compensated for by using a fused silica (SiO$_2$) plate with an AR coating. Fig. 4(a) shows the

group indices of the transmission materials ($n_g(\lambda)$). The plotted values represent the difference from the value at $\lambda_0 = 1580$ nm. The total dispersion was evaluated as a summation of group indices multiplied by their lengths, that is, $\Sigma\{n_g(\lambda) - n_g(\lambda_0)\}L$, where L is the length. The length of the SiO$_2$ plate was determined to be 24 mm to compensate for the total dispersion. Fig. 4(b) depicts the total dispersions with and without the SiO$_2$ plate.
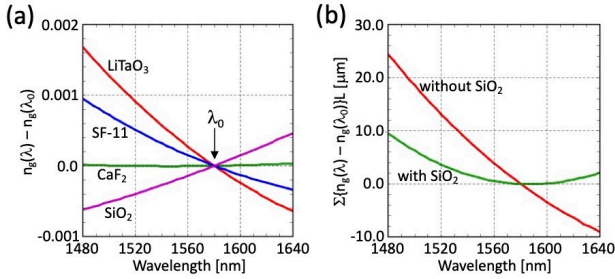

Fig. 4. (a) Group indices of transmission materials in the SPOPO cavity as a function of the wavelength. (b) Total dispersion of transmission materials in the SPOPO cavity.

The pump beam was linearly focused in the horizontal direction using a cylindrical lens with a focal length of 200 mm. A wide region in the MgO:PPLT was pumped and broad spectral components of the signal light were generated in this line-focus setup.
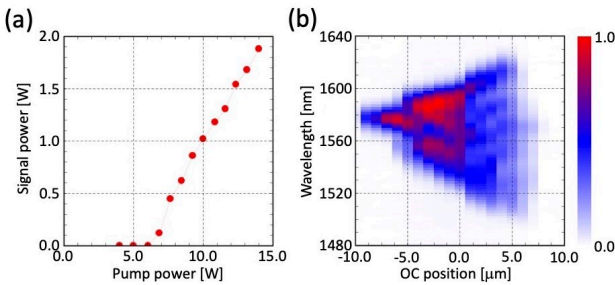

Fig. 5. (a) Signal output power as a function of pump power when the OC position is zero. (b) Contour plot of the signal spectra as a function of the OC position when the pump power is 14.0 W.

Fig. 5(a) depicts signal output power as a function of the pump power. The OC position was determined to maximize the signal output power and this position was defined as the origin of the OC position. The threshold pump power was approximately 7 W. The slope efficiency was approximately 20% in the pump power range over 10 W. Fig. 5(b) shows a contour plot of the spectra as a function of the OC position when the pump power was 14.0 W. The figure shows that the spectra expand with an increase in the OC position. The spectral width was approximately 80 nm at the OC position of 0.0 and 120 nm at the OC position of 5.0 μm. The broadband oscillation was observed in a wider range of the OC

position with an increase in the pump power.

The pump pulse length (FWHM) was measured as 392 fs using the SHG-FROG (frequency-resolved optical gating) measurement. The signal pulse length was 81 fs from the SHG-FROG for the line-focus setup with a pump power of 14 W and the OC position at zero. This length was approximately 1/5 of the pump pulse length. It was observed that the signal pulse length was the shortest when the OC position was near zero. Furthermore, when the OC position was over zero, the spectrum became broader, but the pulse length did not decrease.

In conclusion, the broadband operation of SPOPO with a spatially dispersed beam was demonstrated. Additionally, signal pulses with a pulse length of approximately 1/5 of the pump pulse length were generated.

Acknowledgments

References

[1] S. C. Kumar, J. Wei, J. Debray, V. Kemlin, B. Boulanger, H. Ishizuki, T. Taira, and M. Ebrahim-Zadeh, Opt. Lett. 40, 3897 (2015).
[2] X. Meng, Z. Wang, W. Tian, H. He, S. Fang, and Z. Wei, Opt. Lett. 43, 943 (2018).
[3] J. Fan, C. Gu, J. Zhao, R. Liao, Y. Chu, L. Chai, C. Wang, and M. Hu, Opt. Lett. 43, 2316 (2018).
[4] T. Südmeyer, E. Innerhofer, F. Brunner, R. Paschotta, T. Usami, H. Ito, S. Kurimura, K. Kitamura, D. C. Hanna, and U. Keller, Opt. Lett. 29, 1111 (2004).
[5] A. Esteban-Martin, O. Kokabee, and M. Ebrahim-Zadeh, Opt. Lett. 33, 2650 (2008).
[6] K. A. Tillman, D. T. Reid, D. Artigas, J. Hellström, V. Pasiskevicius, and F. Laurell, J. Opt. Soc. Am. B 20, 1309 (2003).
[7] P. E. Powers, T. J. Kulp, and S. E. Bisson, Opt. Lett. 23, 159 (1998).
[8] D. Artigas and D. T. Reid, Opt. Lett. 27, 851 (2002).
[9] D. Descloux, J.-B. Dherbecourt, J.-M. Melkonian, M. Raybaut, J.-Y. Lai, C. Drag, and A. Godard, Opt. Express 24, 11112 (2016).
[10] S. C. Kumar, S. Parsa, and M. Ebrahim-Zadeh, Opt. Lett. 41, 52 (2016).
[11] L. Chen, S. Wen, Y. Wang, K. You, L. Qian, and D. Fan, Phys. Rev. A 82, 043843 (2010).
[12] B. E. Schmidt, N. Thiré, M. Boivin, A. Laramée, F. Poitras, G. Lebrun, T. Ozaki, H. Ibrahim, and F. Légaré, Nat. Commun. 5, 3643 (2014).
[13] K. Nagashima, R. Itakura, and N. Ishii, Opt. Lett. 46, 4414 (2021).
[14] K. Nagashima, Y. Ochi, and R. Itakura, Opt. Lett. 45, 674 (2020).

Semi-classical approach for laser-metal interaction

OTOBE Tomohito

Ultrafast Dynamics Group, Department of Advanced Photon Research

The comprehensive modeling of laser material machining [1-3] is complex, with multi-scale time and space, multi-phase, and possibly chemical reactions. For laser processing of metals, a two-temperature model (TTM) has been proposed as the simplest continuum model [4]. In the TTM, empirical parameters are employed for all material properties, and the penetration depth models the dynamics of the electromagnetic field. The most critical assumption of the TTM is the quasi-equilibrium of the electron temperature and the electron-lattice interaction term.

Recently, the first-principles approach employing time-dependent density functional theory (TDDFT) [5] has been applied to laser-matter interactions [6,7]. Although TDDFT offers a compromise between accuracy and computational feasibility, its computational cost remains high. Electron-electron collisions (which are not included in TDDFT) play an important role in the laser-metal interactions.

The Vlasov equation has been employed in nuclear physics and electron dynamics in metal clusters to describe the collision process of fermi particles [8-10]. Because the Vlasov equation treats the distribution function of space, momentum, and time, it requires tremendous computational resources. In general, the computational cost is reduced by assuming that the distribution function is the summary quasi-particles.

The time-dependent Kohn–Sham equation [5] is the fundamental equation of the TDDFT.

$$i\hbar \frac{\partial \phi_i}{\partial t} = H_{KS}\phi_i \qquad 1$$

Here:

$$H_{KS}[n_e(\vec{r},t)] = -\frac{\hbar^2}{2m}\nabla^2 + V_{eff}[n_e(\vec{r},t)] \qquad 2$$

where H_{KS} was the Kohn–Sham Hamiltonian, m the electron mass, V_{eff} the effective potential, and $n_e(\vec{r},t)$ the time-dependent electron density.

$$n_e(\vec{r},t) = \sum_{i=1}^{N}|\phi_i(\vec{r},t)|^2 \qquad 3$$

Further, the von Neumann equation governed the time-evolution of the density matrix $\hat{\rho}$

$$\frac{\partial \hat{\rho}(\vec{r},\vec{r}',t)}{\partial t} = -\frac{i}{\hbar}[\hat{H}_{KS}, \hat{\rho}(\vec{r},\vec{r}',t)]. \qquad 4$$

By performing the Wigner transformation and taking the limit $\hbar \to 0$, the density operator was mapped onto a real function $f(\vec{r},\vec{p},t)$, which obeyed the Vlasov equation:

$$\frac{\partial}{\partial t}f(\vec{r},\vec{p},t) = -\frac{\vec{p}}{m}\cdot\nabla_{\vec{r}}f(\vec{r},\vec{p},t) + \nabla_{\vec{r}}V_{eff}\cdot\nabla_{\vec{p}}f(\vec{r},\vec{p},t), \qquad 5$$

Here, $f(\vec{r},\vec{p},t)$ was interpreted as the electron distribution function in phase space.

The effective potential was a function of the electron density $n_e(\vec{r},t)$ and decomposed into

$$V_{eff}[n_e(\vec{r},t)] = V_{Cou}[n_e(\vec{r},t)] + V_{xc}[n_e(\vec{r},t)] + V_{ext}(\vec{r},t), \qquad 6$$

with the exchange-correlation potential V_{xc} [11], external field potential V_{ext}, and

$$V_{Cou}[n_e(\vec{r},t)] = \sum_{j}V_{ps}(\vec{r}-\vec{r}'_j) + V_H[n_e(\vec{r},t)], \qquad 7$$

where V_{ps}, V_H, and j denoted the ionic pseudopotential, Hartree potential, and label of ions, respectively.

We employed a modified Heine–Abarenkov-type local pseudopotential for V_{ps} with parameters to reproduce the all-electron density functional theory calculations [12]. V_H was evaluated by solving the Poisson equation. V_{xc} was the exchange-correlation potential in the local density approximation. The laser-electron interaction was described in the length gauge.

We approximated the six-dimensional time-dependent function with the summation of the pseudo particle (PP):

$$f(\vec{r},\vec{p},t) = \frac{1}{N_s}\sum_{k=1}^{N_{pp}}g_r(\vec{r}-\vec{r}_k(t))g_p(\vec{p}-\vec{p}_k(t)) \qquad 8$$

Here, k was the label of the PP, and N_{pp} the total number of PPs defined as $N_{pp} = N_s N_e$, where N_s and N_e were the number of PPs per electron and the total number of electrons, respectively.
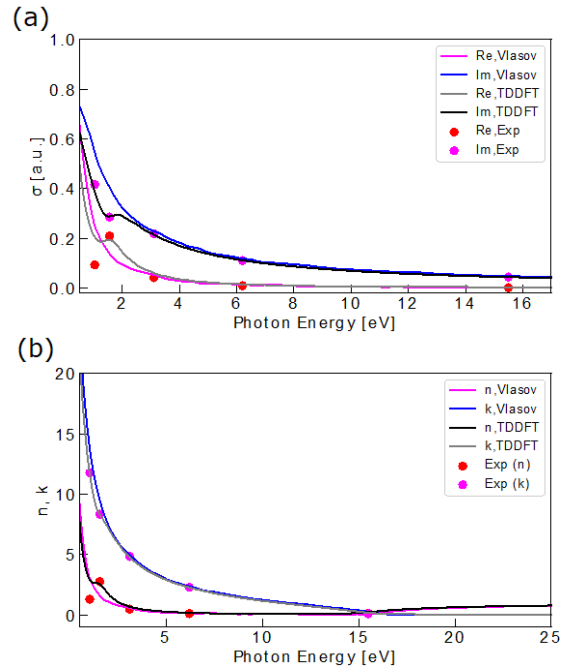

Fig. 1 (a) Conductivity and (b) refractive indexes of bulk-Al with the Vlasov equation and TDDFT [15]. The filled circles indicate the experimental results [13].
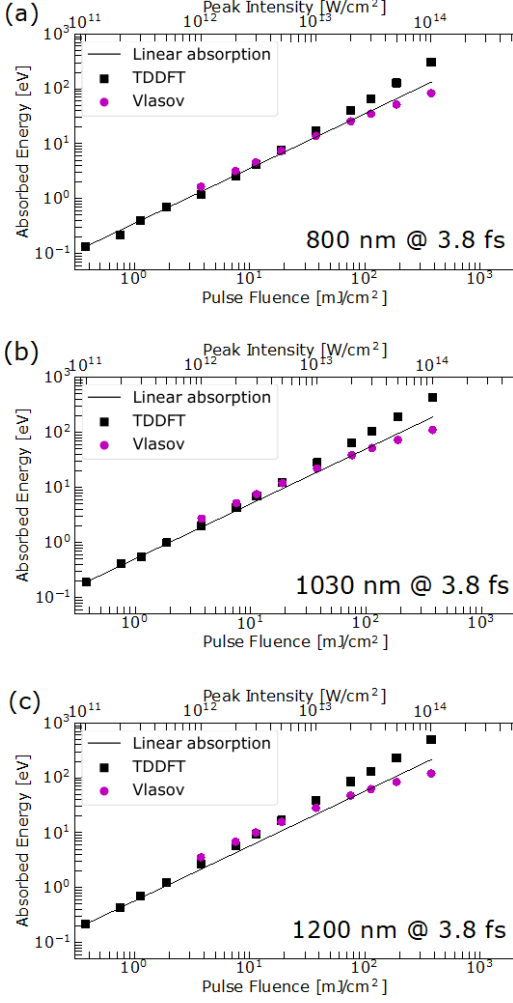
Fig. 2 Laser fluence dependence of the energy absorption with a wavelength of (a) 800 nm, (b) 1,030 nm, and (c) 1,200 nm.[15]

We defined the smoothing functions for position $g_r(\vec{r})$ and momentum $g_p(\vec{p})$ in the Gaussian form. The Newton equation described the motion of the PP under an effective potential with a periodic boundary condition as follows:

$$\frac{d\vec{r}_k}{dt} = \frac{\vec{p}_k}{m} \qquad 9$$

$$\frac{d\vec{p}_k}{dt} = -\int d\vec{r}\, V_{eff}(\vec{r})\nabla_{\vec{r}}\, g_r(\vec{r}_k(t) - \vec{r}) \qquad 10$$

The dynamics of PPs were performed by the Verlet method [14].

We discussed the complex optical conductivity, refractive index, extinction coefficient, and reflectivity as functions of photon energy [15]. Despite the simplicity of the Vlasov approach, the results agreed with the TDDFT results and experimental values (Fig. 1). The peak and dip at approximately 1.5 eV in the TDDFT results were due to inter-band transition, which was not reproduced by the present Vlasov approach because the latter considered only the free-electron dispersion.

Fig. 2 shows the absorbed energy as a function of laser intensity with laser wavelengths of (a) 800 nm, (b) 1,030 nm, and (c) 1,200 nm [15]. The triangles indicated the results obtained using TDDFT, and the circles indicated the results obtained using

the Vlasov equation. The scaled one-photon absorption was indicated by the solid line for the guiding eye. At all wavelengths, the Vlasov equation agreed with TDDFT below the intensity of 1×10^{13} W/cm². Above 1×10^{13} W/cm², Vlasov underestimated compared with TDDFT.

Here, we proposed a semi-classical approach for the laser-metal interactions employing the Vlasov equation. The master equation and potential were based on the Kohn–Sham Hamiltonian with a local density approximation. We employed PP to reproduce the continuous density distribution function in the real and momentum spaces. Our results agreed with TDDFT for the weak and intense laser field regimes. In particular, the Vlasov equation reproduced the optical properties of aluminum without artificial parameters. The advantages of the Vlasov equation was its low computational cost (approximately 1/50 of TDDFT) and high scalability. Assuming Pauli blocking, we included the electron-electron collision process in the materials. Further, the collision between PP and the pseudo-potential ensured semiclassical molecular dynamics.

Acknowledgments

References

1. C. Schäfer, H. M. Urbassek, and L. V. Zhigilei, Phys. Rev. B **66**, 115404 (2002)
2. C. Kerse, H. Kalaycıoglu, P. Elahi, B. Çetin, D. K. Kesim, Ö. Akçaalan, S. Yavaş, M. D. Aşık, B. Öktem, H. Hoogland, R. Holzwarth, and F. Ö. Ilday, Nature (London) **537**, 84 (2016)
3. R. R. Gattass and E. Mazur, Nat. Photonics **2**, 219 (2008)
4. S. I. Anisimov, B. L. Kapeliovich, and T. L. Perel'man, JETP **39**, 375 (1974)
5. E. Runge and E. K. U. Gross, Phys. Rev. Lett. **52**, 997 (1984)
6. T. Otobe, M. Yamagiwa, J. -I. Iwata, K. Yabana, T. Nakatsukasa, and G. F. Bertsch, Phys. Rev. B **77**, 165104 (2008)
7. M. Noda, S. A. Sato, Y. Hirokawa, M. Uemoto, T. Taleuchi, S. Yamada, A. Yamada, Y. Shinohara, M. Yamaguchi, K. Iida, I. Floss, T. Otobe, K.-M. Lee, K. Ishimura, T. Noku, G. F. Bertsch, K. Nobusada, and K. Yabana, Comp., Phys. Commun. **235**, 356 (2019)
8. A. Domps, P. -G. Reinhard, and E. Suraud, Ann. Phys. **260**, 171 (1997)
9. L. Plagne, J. Daligault, K. Yabana, T. Tazawa, Y. Abe, and C. Guet, Phys. Rev. A **61**, 033201 (2000)
10. T. Fennel, G. Bertsch, and K.-H. Mwiwes-Broer, Eur. Phys. J. D **29**, 367 (2004)
11. J. P. Perdew and A. Zunger, Phys. Rev. B **23**, 5048 (1981)
12. C. Fiolhais, J. P. Perdew, S. Q. Armster, J. M. MacLaren, and M. Brajczewska, Phys. Rev. B **51**, 14001 (1995)
13. A. D. Rakić, Appl. Opt. **34**, 4755 (1995)
14. L. Verlet, Phys. Rev. **159**, 98 (1967)
15. M. Tani, T. Otobe, Y. Shinohara, and K. L. Ishikawa, Phys. Rev. B **104**, 075157 (2021)

Social implementation of laser hammering system for maintenance of concrete structures

HASEGAWA Noboru

X-ray laser group, Department of Advanced Photon Research

1. Introduction

In Japanese road tunnels, periodic inspections are required once every five years in the wake of the collapse of a ceiling panel in the Sasago Tunnel on the Chuo Expressway in December 2012. Maintenance works are carried out in accordance with the inspection guidelines established by the Ministry of Land, Infrastructure, Transport and Tourism, but there are concerns about a shortage of inspectors in the near future due to aging and retirement. Therefore, new technologies for measurement/ monitoring and non-destructive inspection are being registered in the "Inspection Support Technology Performance Catalog" led by the Ministry of Land, Infrastructure, Transport and Tourism. QST and Photon Lab Co., Ltd. improved the inspection speed of the "laser hammering method"[1] that involves non-contact inspection and digitization. This project was collaboration work with the Institute for Laser Technology (ILT) which was supported through the SIP: Cross-ministerial Strategic Innovation Promotion Program (2014-2019, Yozo Fujino PD) led by the Cabinet Office in collaboration. Based on this result, we have developed a new laser hammering system[2] assuming social implementation. In June 2020, this system was registered in the Inspection Support Technology Performance Catalog (registration number: TN020003-V0020)[3], and trial work was started with a construction consultant company that carries out inspection works[4-7].

2. Laser hammering system

The main requirements for measurement/monitoring and infrastructure inspection technologies are improvement of the inspection speed, remote control, quantification, and digitization, which are in good agreement with the characteristics of the laser hammering method. A schematic of the laser hammering method is shown in Figure 1(a). In this method, a high-intensity pulse laser (1064 nm, 10 Hz, Nd:YAG laser) was used as the impact force, instead of a hammer. The irradiated laser energy was converted into momentum as a blowout of small particles (laser ablation), and an impact force was generated on the concrete surface. The excited vibration on the concrete surface was measured using an interferometer (laser Doppler vibrometer) with a continuous oscillation laser (532 nm, Nd:YVO₄ laser). A wavelength of 532 nm is suitable for the surface vibration of concrete because it passes through water and can measure surface vibrations even if the concrete surface is wet. Both lasers were irradiated to the inspection point through galvanic mirrors for high-speed scanning. The interval between each measurement point was set arbitrarily (minimum 10 mm), and the range of one scan was approximately 500 mm for the object at a distance of 5 m. If a 500 mm square area is measured at 50 mm scan intervals, 121 points are measured, and the required time is 36 s (measured three times per point to improve the S/N ratio).

A schematic for detecting defects using the laser hammering method is shown in Figure 1(b). Resonant vibration occurs in the area containing a defect, such as peeling inside the concrete, due to interference in the elastic wave at the position of the defect

(deflection resonance). For example, in the case of a disk-shaped defect with diameter $2a$ located at a depth l, the resonance frequency is proportional to l/a^2. On the other hand, resonant vibration does not appear in sound (defect-free) areas. Inspectors using the conventional hammering test recognize the difference in the magnitude and frequency of these vibrations as a difference in sound, and determine the soundness of the concrete. Similarly, in the laser hammering method, the detection of defects is determined by the resonant frequency and spectral power.
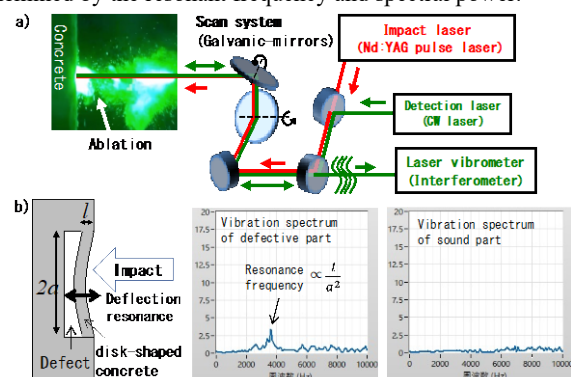

Figure 1) Scheme of the laser hammering method[4]

Figure 2 shows the laser hammering system (LHS) mounted on a 4-ton loading platform truck. The LHS can be easily transported to the destination tunnel, and laser alignment after arriving at the tunnel is almost unnecessary. The LHS contains an optical system (impact laser, laser vibrometer, scanning, and aiming system), a control system (laser driver, chiller, device for data acquisition and analysis), and a diesel electric generator. Each component was mounted on vibration isolators to prevent interference due to vibrations from the diesel electric generator and vehicle engine. Sub-micron scale vibration measurement is possible when the vehicle is stopped[5].
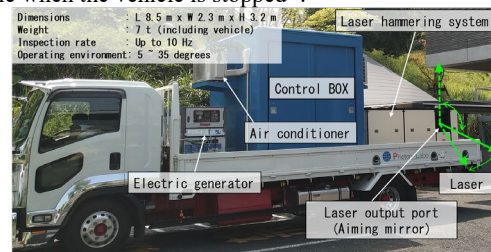
Figure 2) Laser hammering system mounted on vehicle[4]

The impact and detection laser beams are guided to the inspection points, such as cracked areas of the tunnel surface and locations where the presence of defects was reported in previous inspections, by the aiming mirror installed at the laser output port. By using the aiming mirror, it is possible to measure any position in the circumferential direction of the tunnel, and several meters in the travel direction of the tunnel, while the vehicle is stopped.

For measurements of more than several meters in the travel direction, the vehicle is moved.

3. Application to maintenance of road tunnels

A trial to apply LHS to the maintenance of road tunnels was started in collaboration with a construction consultant company in 2020[4-7]. Figure 3 shows inspection of a horizontal construction joint (spring line), which are required to be inspected according to Road Tunnel Periodic Inspection Guidelines. This work was carried out by placing an LHS vehicle in a lane closed to traffic. The area around the LHS was designated as a laser-controlled area according to JIS C6802 "Safety of laser products".
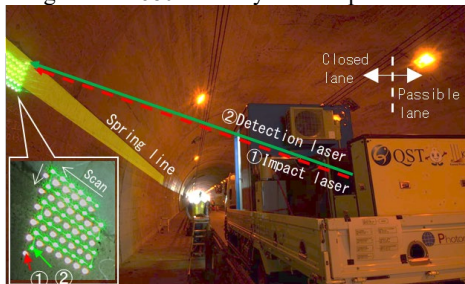

Figure 3) Laser hammering inspection under one-sided traffic restrictions in road tunnel[4]

Figure 4 shows an example of the results for one span of the spring line (10.5 m) and the measured vibration spectrum. The inspection area per scan was 50×50 cm, and the inspection interval was 5 cm. The areas shown in red were identified by LHS as containing defects, and the green areas were determined to be defect-free. The defects were concentrated near the boundary of the spring line, and this result was in good agreement with that obtained by a conventional hammering test.

The results in Figure 4 result in a binary judgment (sound or defective). However, it is possible to obtain more detailed information by analyzing the vibration spectrum. For example, the relative severity of a defect can be determined from the spectral power ((2) >> (4) > (1) >> (3)). Furthermore, by recording the vibration spectrum, it is possible to obtain information on the progress of the severity of the defect in subsequent inspections.

It will be possible to develop AI that can classify the soundness according to categories I to IV in response to the requirements of the Road Tunnel Periodic Inspection Guidelines by learning the vibration spectrum and time waveform of various defects. This research is in progress as the improvement of the judgment/diagnosis system of LHS in the SIP 2nd phase (2018~, Yuichiro Anzai PD).

4. Summary

The laser hammering system developed by QST and Photon Lab has been used in several trials[4-7] as a support tool for the inspection of road tunnels since June 2020. To meet the demands of practical usage, such as increased speed and smaller size, improvements and optimization[8] of the device and operation are in progress through multiple national projects, including the SIP 2nd phase.
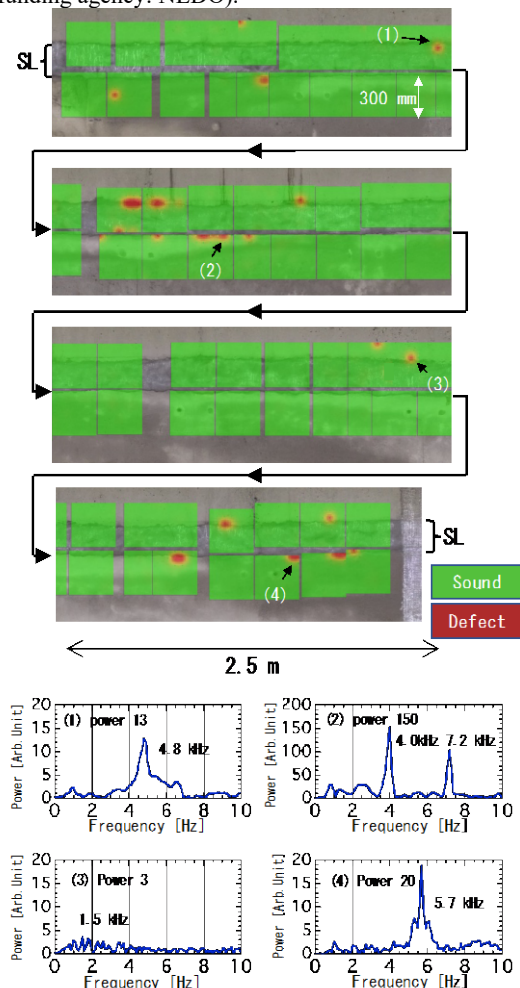
Figure 4) Inspection result at the horizontal construction joint (spring line) in the road tunnel[4]

References

1. S. Kurahashi, K. Mikami, T. Kitamura, N. Hasegawa, H. Okada, S. Kondo, M. Nishikino, T. Kawachi, and Y. Shimada: J. Appl. Remote Sens., 12 (2018) 15009.
2. N. Hasegawa, M. Nishikino, H. Okada, S. Kondo, T. Kitamura, M. Abe, K. Masuzoe, S. Kogure: ITA-AITES World Tunnel Congress, WTC2020 and 46th General Assembly Kuala Lumpur, Malaysia 11-17 September (2020) 653-656.
3. Photon Lab Co., Ltd.：Ministry of Land, Infrastructure, Transport and Tourism Road Bureau, Inspection Support Technology Performance Catalog, Non-destructive inspection technology (tunnel), (2020) 2-283 - 2-287.
4. N. Hasegawa, H. Okada, S. Kondo, T. Kitamura, M. Nishikino, K. Sakamoto and S. Kogure: Journal of the Society of Instrument and Control Engineers, Vol.60 No. 11 (2021) 765-769.
5. N. Hasegawa, M. Nishikino, H. Okada, S. Kondo, T. Kitamura, S. Kogure：Photonics division, Vol.7, No.1, (2021) 22-26.
6. S. Tomoto, N. Hasegawa, T. Kitamura, Y. Fujisaki：Journal for Civil Engineers, Vol. 62, No. 7 (2021) 84-87.
7. S. Tomoto, N. Hasegawa, H. Okada, S. Kondo, T. Kitamura, K. Mikami, M. Nishikino, and H. Nakamura: JSCE Committee of Structural Engineering, Vol.68A (2022) 671-684.
8. K. Mikami, N. Hasegawa, T. Kitamura, H. Okada, S. Kondo, and M. Nishikino: Jpn. J. Appl. Phys. 59 (2020) 076502-1-10.

Theoretical account on the calculation of long-range electrostatic interactions

YONETANI Yoshiteru

X-ray Laser Group, Department of Advanced Photon Research

Electrostatic interactions are critically important because they govern the microscopic and macroscopic behaviors of various molecular systems. The calculation of electrostatic interactions has been one of the major subjects in particle simulations, such as molecular dynamics (MD) and Monte Carlo (MC) simulations [1, 2]. Short-range interactions, such as van der Waals forces, can be evaluated using a cutoff treatment that considers finite-range contribution only. However, electrostatic interactions are long-range, and the contributions from distant regions are non-negligible. Thus, a simple cutoff treatment suffers from various artifacts in terms of the structural and energetic properties. The most significant problem is that the cutoff treatment does not ensure convergence of the simulation results. Increasing the cutoff length does not necessarily improve the simulation results. A typical example is the structure of liquid water; previous MD studies [3-5] clearly showed that increasing the cutoff length worsens the result, contrary to our expectations. In extreme situations, the cutoff simulation produces an artificial layer structure in which water molecules are highly ordered in dipolar orientations [3-5].

In 1980, Neumann and Steinhauser [6] explored the theoretical background of the cutoff problem. Using the Onsager dielectric continuum model with a cutoff boundary condition, they evaluated the electric behavior of a dielectric medium surrounding a dipolar particle. The result of the distance-dependent Kirkwood function $G_K(R)$ showed that the cutoff boundary condition produced field polarization that was strikingly different from the correct no-cutoff case. A no-cutoff calculation that considers the contributions from an infinite region provides a flat $G_K(R)$ profile. However, when the cutoff condition was applied, a peculiar hole-like profile appeared in the $G_K(R)$ function. This emergence of unusual polarization can be recognized as cutoff-induced dipolar ordering. In this way, Neumann and Steinhauser [6] theoretically demonstrated how the cutoff treatment produces an artificial orientational order in dipolar systems.

Recently, cutoff-based real-space treatment has improved significantly [7–9]. Suitable tuning of shifting and damping can substantially reduce cutoff artifacts. MD simulations using this approach have provided good results for various molecular systems, such as liquid water, liquid–vapor, biomolecules, and inorganic materials. However, such developments in real-space treatment have not yet been completed. Studies on the real-space treatments are trying to address the fundamental problem, that is, if long-range electrostatic features in condensed phases can be described using the short-range treatment. To achieve this,
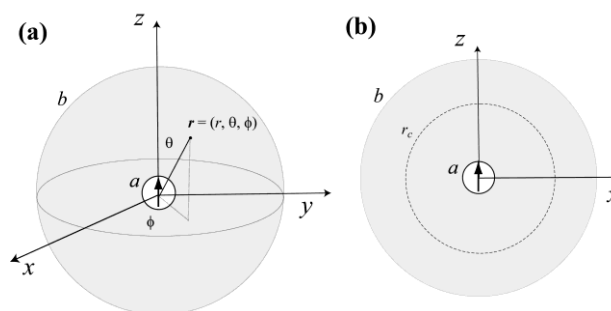

Fig. 1: Dielectric continuum model (left) and the two-dimensional view (right). The parameters a and r_c are the radii of the central dipolar particle and cutoff, respectively. b denotes the region of the dielectric continuum. (Reprinted from [10], with the permission of AIP publishing)

thorough theoretical exploration is required.

In this study [10], we employed the dielectric continuum model (Fig. 1) to explore the fundamental background of the recently developed shift treatments. Shifting has been widely used as a pivotal part of modern real-space treatment. From a physical point of view, shifting can be interpreted as an image-charge (or image multipole) effect that accounts for the electric cancellation in condensed phases [7]. Here, we selected three ways of shifting: shift potential (SP), gradient-shift force (GSF), and Taylor-shift force (TSF) [9]. We explored the physical background of these shifting schemes using the Neumann–Steinhauaer approach [6]. The results clarified how shifting reduces the cutoff artifact and what remains to be solved [9].

Fig. 2 shows the results of the theoretical analysis. When using a simple cutoff (i.e., bare), $G_K(R)$ decreased when $R < r_c$ and then increased when $R > r_c$. This is a *hole-shaped artifact*, known as a major cutoff artifact [3–6]. In contrast, SP, GSF, and TSF exhibited distinct behavior, in which $G_K(R)$ gradually increased with R. For comparison, the no-cutoff result [6] is also shown in the figure. In this case, $G_K(R) = 1$ for any value of R. All other results show some deviations from this correct result. SP, GSF, and TSF avoided the cutoff artifact of the hole shape. However, deviations from the flat profile [i.e., $G_K(R) = 1$] remained, indicating that some artificial orientational order existed. That is, shifting alone was not sufficient for SP, GSF, and TSF; shifting should be employed with damping, as suggested previously [9].

To clarify why different treatments produce different shapes of $G_K(R)$, we next considered the relationship between the dipolar
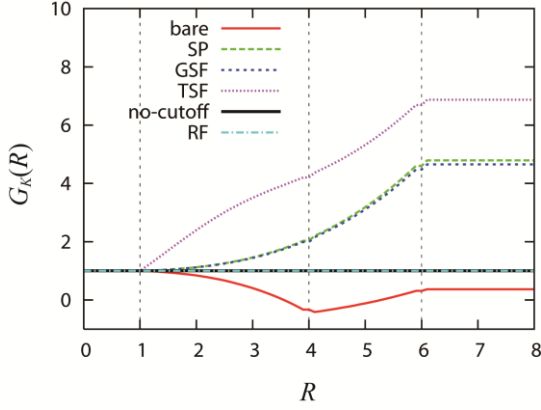
Fig. 2: Distance-dependent Kirkwood function $G_K(R)$. The parameters used were $a = 1.0$, $r_c = 4.0$ and $b = 6.0$, which are denoted by the vertical dotted lines. No-cutoff [6] and reaction field (RF) results overlapped completely. (Reprinted from [10], with the permission of AIP publishing)

force K and $G_K(R)$. Based on the dielectric continuum model (Fig. 1) employed here, the central dipolar force K produces the surrounding dielectric polarization P, which consequently produces the electric field F. The spatial distribution of the F vectors seemed similar between the bare cutoff and the shift treatments; however, we observed a significant difference. The difference from the no-cutoff result ΔF ($= F - F_{no\text{-}cutoff}$) clearly shows that the bare cutoff was distinctly different from the other cases: SP, GSF, and TSF. In particular, the ΔF of the bare cutoff was discontinuous at the cutoff boundary $r = r_c$, where the directions were upset. Such drastic changes were not observed in SP, GSF, and TSF.

To verify the theoretical results, we performed Monte Carlo simulations on dipolar particles [$r_c = 9.38$, 17.31, and 28.00 Å]. The MC results (Fig. 6 in Ref. [10]) were slightly different from the continuum results (Fig. 2), particularly at the short cutoff $r_c = 9.38$ and 17.31 Å. However, at the largest cutoff of $r_c = 28.00$ Å, the MC result was slightly similar to the result of the continuum model. The continuum feature was more visible when the number of particles included within the spherical cutoff region $r = r_c$ increased (that is, $r_c \sim 28.00$ Å). This indicates that increasing the particle number made the local microscopic feature less dominant and the global macroscopic feature more dominant. In

other words, the continuum model analysis captured the feature with a large r_c well.

In particular, the continuum analysis presented here could predict if *hole-shaped artifact* appeared; it produced *hole-shaped artifact* for bare cutoff, but not for other shift treatments (Fig. 2). This indicates that the shift treatments resolved the $G_K(R)$ problem of the simple cutoff. In this respect, the present continuum model results were consistent with the MC results.

As shown in the MC results (Fig. 6 in Ref. [10]), the bare cutoff exhibited a large deviation, which became significant as r_c increased. At $r_c = 28.00$ Å, the hole shape grew significantly. In this case, an artificial layer structure [3–5] was formed (Fig. 3; bare cutoff). The other shift treatments did not show such an artificial structure (Fig. 3). This suggests that the shift treatments still resolved this problem. This observation was consistent with that for the continuum model, where shift treatments did not show any indication, that is, no hole.

This study [10] theoretically explains how recent modifications to electrostatic calculations can improve the simple cutoff. The present study, using the continuum model, offers a stringent criterion to determine whether the basic electrostatic behavior is correctly described. This knowledge will be useful for future construction of electrostatic treatments. In addition, the present study contributes to the progress of computational physics, which covers a broad range of scientific fields, such as material and biological sciences.

References

1. M. P. Allen and D. J. Tildesley, Computer Simulation of Liquids (Oxford University Press, 1987).
2. D. Frenkel and B. Smit, Understanding Molecular Simulation: From Algorithms to Applications, 2nd ed. (Academic Press, 2001).
3. Y. Yonetani, Chem. Phys. Lett. **406**, 49 (2005).
4. Y. Yonetani, J. Chem. Phys. **124**, 204501 (2006).
5. D. van der Spoel and P. J. van Maaren, J. Chem. Theory Comput. **2**, 1 (2006).
6. M. Neumann and O. Steinhauser, Mol. Phys. **39**, 437 (1980).
7. D. Wolf, P. Keblinski, S. R. Phillpot, and J. Eggebrecht, J. Chem. Phys. **110**, 8254 (1999).
8. I. Fukuda, Y. Yonezawa, H. Nakamura, J. Chem. Phys. **134**, 164107 (2011).
9. M. Lamichhane, J. D. Gezelter, and K. E. Newman, J. Chem. Phys. **141**, 134109 (2014).
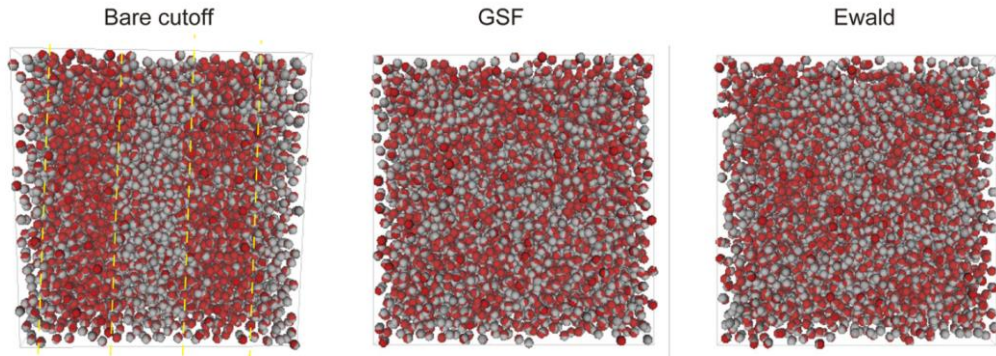10. Y. Yonetani, J. Chem. Phys. **154**, 044103 (2021).

Fig. 3: Results from the Monte Carlo simulations of dipolar particles. Each particle is colored red and gray to show the dipolar direction. Bare cutoff shows the layer structure (denoted by the yellow dashed lines), whereas GSF and no-cutoff (Ewald) do not. (Reprinted from [10], with the permission of AIP publishing)

Development of compact, high-energy Yb:YAG passive Q-switch laser for pumping nonlinear process

AKAHANE Yutaka and YAMAKAWA Koichi

Medical Laser Applications Group, Department of Advanced Photon Research
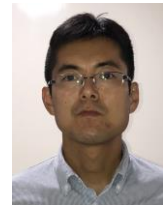
We studied tiny ytterbium (Yb)-doped high-intense passive Q-switched lasers for the development of palm-sized intense infrared (IR) lasers that employ optical-parametric oscillation (OPO). The passive Q-switched laser can generate intense, short laser pulses without opto-electric polarizing devices such as Pockels cell; it is suitable for pumping palm-sized OPO lasers. When generating mid-IR (over 3 μm) laser pulses with an OPO scheme, the low OPO gain and low laser damage threshold (<10 MW/cm^2) of nonlinear OPO crystals should be considered. A laser cavity for this mid-IR OPO must have a relatively long (a few centimeters) OPO crystal and be pumped by long nanosecond (ns: 10^{-9}s; a few ns ~10 ns) laser pulses. Yb:YAG was chosen as laser gain media to generate such long ns pulses. For the same cavity length, shown in Fig.1, considerably longer ns pules can be generated with Yb:YAG laser cavity than with conventional Nd:YAG[1]. In this study, we have designed compact laser cavity with Yb:YAG gain media, and succeeded to generate such long laser pulses from passive Q-switched pump lasers with high energy.
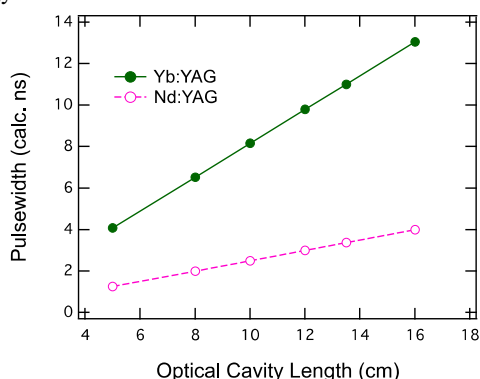

Fig. 1 Calculated width of output laser pulse with respect to optical cavity length in a passive Q-switch laser with a Cr:YAG saturable absorber. For the same cavity length, considerably longer pules can be generated from an Yb:YAG laser cavity (green) than Nd:YAG (pink).

The schematic of our passive Q-switch laser is shown in Fig. 2. Yb:YAG ceramics is used as gain medium, which is monolithically calcined with Cr:YAG ceramic material as a saturable absorber. The Yb:YAG-side surface of the monolithic ceramic was high-reflection (HR) coated, which acted as a cavity mirror. The composite structure of Yb:YAG/Cr:YAG monolithic ceramics has the advantage of reducing the number of boundary surfaces for higher damage resistance. The Yb:YAG ceramic was pumped by fiber-coupled laser diode (LD) at 940 nm. The laser cavity of Yb:YAG microchip laser comprised the HR coated surface of Yb:YAG ceramic and partially reflecting coated surface of the output coupler. The optical length of the laser cavity was approximately 24 mm. The Q-switched pulses generated at a wavelength of 1030 nm, as shown on the left picture in Fig.2, are launched from the surface of the output coupler. In the experiment,
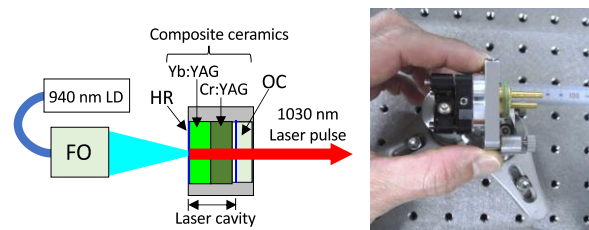
Fig. 2 Schematic and photo of Yb:YAG microchip laser. LD: laser diode, FO: focusing optics, HR: high-reflection coating, OC: output coupler.

laser pulses of 3 mJ, 3 ns (FWHM) were obtained at a repetition rate of 60 Hz.

We also measured the long-term stability of laser output of the microchip laser. As seen in Fig. 3, the energy of the output laser pulses fluctuated because of the effect of residual thermal load on the pump LD irradiation. In the first experiment, the standard deviation of the measured output laser energy was 12% with water cooling. To improve stability of the laser, thermoelectric (TE) cooling was introduced with the laser system. After this modification, the standard deviation was reduced to 5%, which is sufficient stability for pumping a mid-IR OPO.

A plural Q-switch laser pulse generation from a single-pump LD irradiation is available with this laser cavity. When the duration of LD pump pulse exceeds the next Q-switching threshold, successive Q-switchings occur in a sequence. In the typical temporal waveform shown in Fig.4, we can see a barrage of four Q-switched laser pulses on a single LD pump pulse irradiation. There are several merits with plural Q-switching operation on OPO pumping, such as repetition multiplexing, high power and

Fig. 3 Long-term energy output of microchip laser. Standard deviation of the output laser energy was 12% with a water-cooled jacket (red), which was improved to 5% with a thermoelectric cooled jacket (blue).

Fig. 4 (Top) Observed plural passive Q-switching; typical temporal waveform of output laser pulses. (Bottom) total output energy and laser efficiency with respect to pump LD pulsewidth. Inset numbers (1-4) indicate the numbers of plural Q-switching pulses.
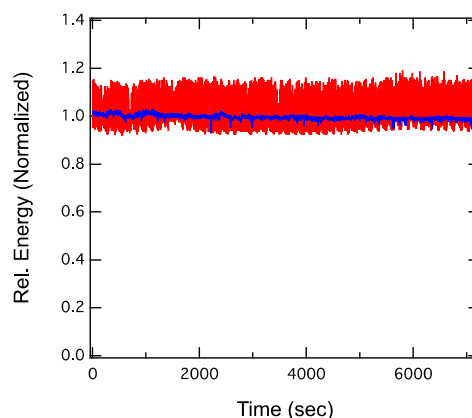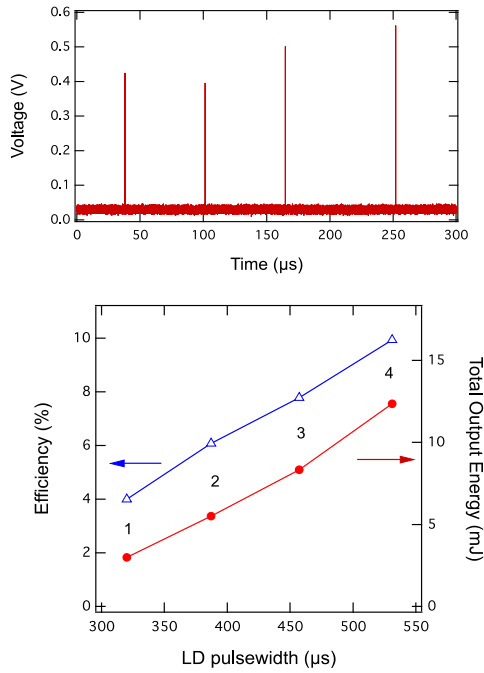
efficiency of laser output, which is a potential tools for compact mid-IR lasers.

The laser cavity could be extended generate a longer (~10 ns) energetic laser pulse. Figure 5 shows the measured output energies and pulse durations with respect to the cavity length of the Yb:YAG microchip laser. As the theoretical prediction[2], pulse duration of output laser pulse is almost proportional to cavity length, and lengthening the cavity increases the output laser pulse energy with cavity mode expansion. The output energy, shown in Fig. 5, increases with a longer cavity, and a maximum 6.3 mJ pulse energy was measured with a cavity of ~160 mm. The measured pulse duration was also increased with a longer cavity from 4.3 ns to 12.0 ns (FWHM).
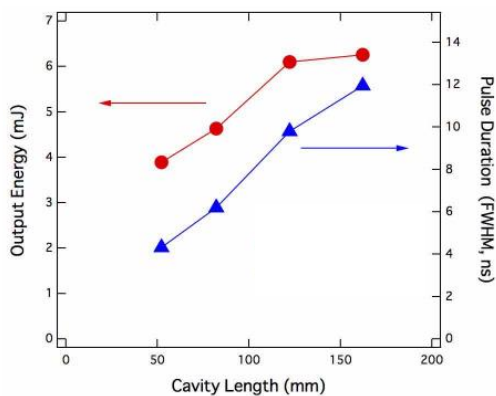

Fig. 5 Output energies (red circles) and pulse durations (blue triangles) with respect to cavity length in the Yb:YAG passive Q-switch laser, which is increased with cavity lengthening. Maximum energy and pulse duration were 6.3 mJ and 12.0 ns (FWHM), respectively, with a ~160 mm cavity.

Spatial and temporal shaping of laser pulse should be considered to utilize high-intensity passive Q-switch laser pulses as the OPO pump pulse. In general, laser pulses generated in long-cavity lasers tend to exhibit multimodal beam profiles. In a long cavity passive Q-switch laser using a saturable absorber, a laser pulse that originates from the large-diameter multimode part contains a low intensity temporal component generated from the outer higher-modes of the laser cavity. The low-intensity temporal component does not contribute to nonlinear laser interaction, such as OPO in some cases, which has a threshold of laser intensity. And furthermore, irradiation by the un-needed low-intensity part of the laser pulse causes laser damage on the OPO crystal. Spatial filtering (SF) was introduced to eliminate the low-intensity, higher-mode of Q-switched output laser pulses. As shown in Fig. 6, a spatial filter, comprising a lens pair and a pinhole was installed on the output laser optical path. The diameter of the pinhole was set to ~1.2 times larger than the diffraction-limited size of the laser beam, which is a compromise
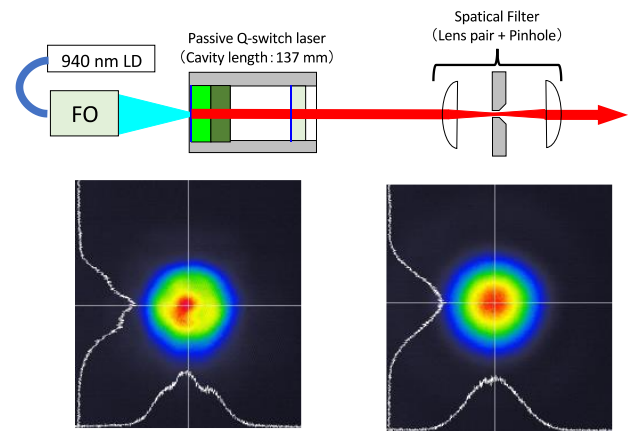
Fig. 6 (Top) Schematic of spatial filtering in Yb:YAG passive Q-switch laser. (Bottom) Spatial profiles of output laser pulses: left: without spatial filter, right: with spatial filter.

between eliminating higher modes and maintaining the transmission efficiency.

After SF, shown in lower images in Fig.6, the spatial profile was significantly improved. The duration of the laser pulse was also reduced from 11.4 ns to 10.8 ns with SF, and the threshold pump laser intensity for some mid-IR OPO was reduced from 3.7 MW/cm^2 to 2.3 MW/cm^2, which clearly shows the effectiveness of the SF technic.

In summary, we developed a compact, intense passive Q-switch laser with Yb:YAG/Cr:YAG composite ceramics for pumping nonlinear processes. In the microchip laser cavity of 24 mm length, an output laser pulse with 3 mJ of energy and 3 ns of duration was obtained at 60 Hz. We also observed multiple Q-switched laser oscillation on a single LD pumping, which is expected to efficient laser pulse generation. In a long cavity design, the energy and the pulse duration of the generated Q-switched laser pulse were increased to 6.3 mJ and 12.0 ns, respectively, which can be a more powerful infrared OPO pump source with spatial filtering. Lasers studied in this research will contribute to the development of palm-sized intense mid-infrared lasers, which have many applications in fields including medical care, environment measuring, material treatment.

References
1. Y. Akahane, et. al. Jpn. Patent 6551898 (2019)
2. H. Sakai, et. al., Opt. Express. 16 19891 (2008)

Research Activities at the Synchrotron Radiation Research Center

WATANUKI Tetsu

Synchrotron Radiation Research Center

A wide range of X-ray techniques are being developed at the Synchrotron Radiation Research Center (SRRC) for the investigation of the structural, electronic, and magnetic properties of matter, primarily using the two QST beamlines, BL11XU and BL14B1, at the large synchrotron radiation facility SPring-8. Hard X-ray non-destructive *in situ* techniques are investi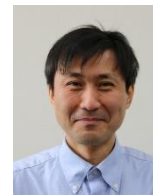gated to enable ground-breaking measurements using techniques such as single atomic-layer magnetic microscopy, element/orbital-specific excited state analysis, coherent X-ray nanoscale imaging, and time-resolved studies of samples under extreme conditions.

The SRRC consists of the Coherent X-ray Research Group, High-Pressure Science and Stress Research Group, Magnetism Research Group, Condensed Matter Theory Group, and a beamline operation office (Table 1). The research activities of each research group are summarized below.

Measures have been undertaken to support digital transformation (DX) of the activities at SRCC by utilizing the supplemental budget to upgrade the equipment and facilitate automatic measurements. A contract was signed with the Advanced Research Infrastructure for Materials and Nanotechnology in Japan (ARIM) to initiate a project for the development of a unifying structure for the data generated by the in-house analysis equipment at the facility. Additionally, work has been conducted to upgrade the monochromator of BL11XU for the reduction of beam instabilities and enhancement of the beam quality. The equipment developed at SRCC is available for public use and we accepted 34 research proposals in FY2021 as a member institute of the Nanotechnology Platform Japan [1].

Synchrotron/ free-electron laser (FEL) X-ray facilities are being constructed worldwide at a rapid pace. Research is being conducted by the ***Coherent X-ray Research Group*** to ensure state-of-the-art synchrotron/FEL research. Advanced measurement/analysis techniques are being developed for the effective utilization of novel advanced light sources. The application of spatially coherent X-rays has enabled the visualization of the inhomogeneity inside matter. An apparatus for Bragg coherent X-ray diffraction imaging (Bragg-CDI) is being developed and it will be applied to the study of inhomogeneous structures of sub-micrometer-sized crystalline fine particles of functional materials. The technique is applicable to particles with a size in the range of 40 – 500 nm [2].

Nonlinear and quantum optical techniques are being developed using simple atomic systems to exploit the temporal coherence and intensity offered by next-generation light sources at short wavelengths. Previously, the soft X-ray beamline of SACLA was used to observe 'superfluorescence' at extreme ultraviolet wavelengths. A source of superfluid liquid helium droplets is being developed for use at SACLA. The development

of this source will extend the technique to shorter wavelengths and ensure improved pulse control. The development and application of world-leading pump-probe [3] and innovative [4] gas-phase measurements are ensured by this group.

A surface X-ray diffractometer coupled with a molecular beam epitaxy chamber was used for in situ measurements of crystal truncation rod (CTR) scattering to investigate the atomic structure of gallium nitride surfaces under growth conditions. The presence of a pseudo 1×1 structure was confirmed by the CTR profile analysis and the structural parameters (interlayer distance, coverage, and temperature factor) were determined.

The research objectives of the ***High-Pressure Science and Stress Research Group*** are (i) the development of experimental techniques for in-situ measurements under extreme conditions, including high-pressure conditions and compressed hydrogen gas environments (ii) fundamental and applied studies of advanced functional materials using the above-mentioned techniques (iii) studies on synchrotron radiation X-ray irradiation effects on tumors. The research group members focus on the high-pressure synthesis of novel hydrogen-rich compounds and the study of the nano- to meso-scale structures of functional materials by collaboration with the Coherent X-ray Research Group.

Metal-hydrogen systems are a primary research target of this group. A hydride Al_3FeH_4 at 9 GPa and 750 °C was synthesized [5]. In-situ X-ray and neutron diffraction experiments clarified the hydrogenation mechanism of Fe−Mo alloy under high pressure [6]. An atomic pair-distribution function (PDF) is obtained by Fourier transformation of the total scattering pattern and it is a powerful tool for studying the local structures of functional materials. The nitrogen gas flow type temperature control system was improved to enable measurement between $100 - 400$ K. This system was applied to the giant negative thermal expansion oxide Ca_2RuO_4 to elucidate the mechanism of negative thermal expansion [7]. Additionally, studies have been conducted to investigate the irradiation effects on tumors with nanoparticles containing high-Z elements. The ablation of the tumor spheroid with iodine-loaded nanoparticles was observed using X-rays ($E = 33.2$ keV) above the iodine K-absorption edge [8].

The spin degrees of freedom of electrons have a significant effect on functional materials and devices, ranging from high-T_c superconducting oxides to spintronic devices. In the ***Magnetism Research Group***, advanced X-ray spectroscopic techniques such as nuclear resonant scattering (NRS), resonant inelastic X-ray scattering (RIXS), and X-ray magnetic circularly polarized emission (XMCPE), and measurement techniques utilizing measurement informatics are being developed to unveil the functionality of such materials and devices. Measurement

informatics aims to improve the efficiency of measurement and analysis using machine learning techniques. Recently, active learning is applied to spectral measurements to enhance its experimental efficiency [9]. Automated stopping criterion based on expected generalization error is revealed to be effective in X-ray absorption spectroscopy experiment with active learning. This method enables high-throughput autonomous experiments for the discovery of novel materials. For NRS, synchrotron-based Mössbauer spectroscopy using a frequency-domain technique was conducted by incorporating a nuclear Bragg monochromator. The microscopic origin of the interfacial perpendicular magnetic anisotropy (PMA) on the Fe/Au(111) multilayer surface was studied by ^{57}Fe probe layer method. The measured spectra exhibited the PMA characteristics and enhancement of the interfacial component in the hyperfine field through Fe-Au bonding. The results demonstrated that the PMA in the Fe/Au(111) interface originated from the interaction between the spin and orbital magnetic moments in Fe and Rashba-type spin-orbit coupling in Au [10]. XMCPE is a novel magnetic spectroscopy technique operated in the hard X-ray regime with a distinctive feature of a large flipping ratio (25%) for the $K\alpha$ emission of $3d$ transition metal elements. Recently, a bulk-sensitive magnetic microscope was developed utilizing XMCPE with a 10-μm lateral resolution and the observation of magnetic domains in an electrical steel sheet was demonstrated [11]. Additionally, the sum rules of XMCPE at L edges for $3d$ transition metal elements were deduced utilizing the theoretical framework developed for $K\alpha$ XMCPE spectra [12].
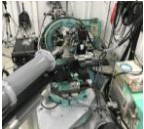
The **_Condensed Matter Theory Group_** develops advanced simulation methods based on quantum mechanics to investigate the theory of condensed matter using supercomputers. Additionally, the methods are applied to perform numerical simulations to understand various properties of materials such as magnetism, high-T_c superconductivity, and catalytic activity, with the support of X-ray experiments such as from SPring-8. The present activities of this group include (i) the development of advanced simulation techniques based on first principles path integral molecular dynamics for investigating the nuclear quantum effects of hydrogen-containing materials such as clathrate hydrates (ii) the development of a numerically exact diagonalization method to investigate time-resolved spectroscopies of antiferromagnetic Mott insulators, which can provide insights into their electronic dynamics [13] (iii) the development of a theoretical framework and computational codes to analyze material properties probed by X-ray spectroscopies such as X-ray magnetic circular dichroism (XMCD), RIXS, and XMCPE [12], and (iv) theoretical investigations using large-scale numerical exact diagonalization of quantum spin systems found in hypermaterials, which exhibit novel quantum phases such as spin nematic liquid.

References

1. http://www.kansai.qst.go.jp/nano/
2. N. Oshime *et al.*, Jpn. J. Appl. Phys. **60**, SFFA07 (2021).
3. F. Allum *et al.*, Faraday Discuss. (2020).
4. H. Iwayama *et al.*, Applied Sciences **10** 7852 (2020).
5. H. Saitoh *et al*, Mater. Des. **208**, 109953 (2021).
6. R. Utsumi *et al*, J. Alloys Compd. **893**, 162300 (2021).
7. L. Hu *et al*, Chem. Mater. **33**, 7665 (2021).
8. Y. Higashi *et al*, Sci. Rep. **11**, 14192 (2021).
9. T. Ueno *et al.*, npj Comput. Mater. **7**, 139 (2021).
10. J. Okabayashi *et al.*, Phys. Rev. B **103**, 104435 (2021).
11. K. Sugawara *et al.*, J. Appl. Phys. **130**, 113901 (2021).
12. A. Koide, T. Nomura *et al.*, Phys. Rev. B **104**, 094419 (2021).
13. K. Tsutsui *et al.*, Phys. Rev. Lett. **126**, 127404 (2021).

Table 1. Groups at the Synchrotron Radiation Research Center.

Group	Coherent X-ray Research Group	High Pressure Science and Stress Research Group	Magnetism Research Group	Condensed Matter Theory Group
Members	K. Ohwada (GL), J. Harries, T. Sasaki	H. Saitoh (GL), A. Machida, A. Shiro, N. Oshime	T. Inami (GL), T. Mitsui, H. Iwasawa, T. Ueno, K. Fujiwara, A. Koide, (K. Ishii, A. Agui)	(T. Sakai (GL)), T. Ikeda, K. Tsutsui, T. Nomura
Typical techniques & Apparatuses	Coherent x-ray scattering Surface x-ray diffraction Quantum optics in EUV region	High-pressure and high-temperature x-ray diffraction Pair distribution function analysis	Mössbauer spectroscopy Resonant inelastic x-ray scattering X-ray magnetic circularly polarized emission	First principles molecular dynamics simulations, numerical calculations
Research objective	Ferroelectrics, nitride semiconductors, superfluorescence	hydrogen containing materials, negative thermal expansion materials, irradiation effects on tumor	magnetism, spintronics, high-T_c superconductivity, measurement informatics	hydrogen containing materials, high-T_c superconductivity, catalysis, magnets
Beamline Operation Office/ Y. Katayama(Section Manager), K. Sugawara, Y. Teraoka, Y. Kai, S. Fujikawa, A. Shimada				

Hydrogen storage by earth-abundant metals, high-pressure synthesis of Al_3FeH_4

SAITOH Hiroyuki

High Pressure Science and Stress Research Group, Synchrotron Radiation Research Center

Hydrogen is a promising energy carrier because it does not emit greenhouse gases during usage. Additionally, once the energy is converted to hydrogen, it will not be lost even if it is stored for a long period of time. Hydrogen is a gas at ambient conditions, and therefore, has a low volumetric energy density. In addition, the high risk of explosions and high diffusivity in the material, which causes a decrease in the material strength called hydrogen embrittlement, make the storage of hydrogen even more difficult. Along with high-pressure hydrogen gas tanks, liquid hydrogen, chemical hydrides, and hydrogen storage materials have been extensively studied for a long time.

In hydrogen storage materials, hydrogen is stored in the form of atoms. A schematic of hydrogen storage in a hydrogen storage material is shown in Fig. 1. Molecular hydrogen dissociates on the alloy surface, diffuses into the alloy as atomic hydrogen, and occupies specific sites in the metal lattice to form interstitial hydrides. As a result, hydrogen exists in a solid state, and the volumetric density of hydrogen in hydrogen storage materials is comparable to that of liquid hydrogen, despite the presence of metal atoms that make up the hydrogen storage materials.

As aforedescribed, hydrogen storage materials have excellent hydrogen storage properties, but still certain problems must be solved, such as low gravimetric hydrogen density and high material costs. Among the hydrogen storage materials that have been developed thus far, $LaNi_5$ and TiFe alloys are commercially used; however, $LaNi_5$ contains an expensive and heavy rare earth element, and TiFe contains relatively expensive titanium. Is it possible to obtain a new hydrogen storage alloy that can solve these issues through material exploration?

The hydrogen storage alloys reported thus far are composed of a combination of metals with high and low affinity to hydrogen [1]. The guideline of "combining metals with high and low affinity for hydrogen" for the synthesis of hydrogen storage materials suggests that hydrides of metals with high affinity for hydrogen are extremely stable to release hydrogen; therefore, the addition of metals with low affinity for hydrogen is adjusted to release hydrogen at moderate temperature conditions. Hence, it is difficult to obtain hydrogen storage materials from only metals

with a low affinity for hydrogen, and there are no actual reports of such materials. Many studies have been conducted on the search for materials based on conventional guidelines, and the author believes that it will be difficult to realize new classes of materials.

We have been searching for new classes of hydrides consisting only of metals with a low affinity for hydrogen using the high-pressure hydrogenation technique, which is expected to be advantageous for the synthesis of new hydrides. Aluminum is a lightweight and inexpensive metal that is ideal for use as a raw material for hydrogen storage materials. However, it is also known that aluminum and its alloys have very low affinity for hydrogen. In 2021, we reported that an alloy consisting only of aluminum and iron, earth-abundant metals with low hydrogen affinity, can form hydrides at high temperatures and pressures and that the resulting hydrides may be thermodynamically stable even at near-ambient pressures [2]. If the synthesis pressure of this hydride can be lowered, it can be used as a hydrogen storage material. The experimental procedure and results are described below.

The starting material was an $Al_{13}Fe_4$ alloy prepared in an arc furnace. The ingot obtained was crushed into a disk with a diameter of 1 mm and height of 0.4 mm. The disk-shaped sample was set in a sample capsule made of boron nitride and located in a cubic pressure medium along with a graphite heater, internal hydrogen source, and hydrogen-sealing capsule. The internal hydrogen source evolved hydrogen at a high pressure, and the evolved hydrogen was confined in the hydrogen-sealing capsule. Hydrogen can permeate the boron nitride capsule and react with the sample, whereas byproducts from the internal hydrogen source cannot pass through the capsule. Thus, we hydrogenated the alloys under a high pressure and temperature.

The sample was pressurized to 9 GPa at room temperature and heated to 750 °C at approximately constant pressure of 9 GPa. The sample was immersed in fluid hydrogen to form its hydride. The sample was then cooled to room temperature and depressurized to ambient pressure. The hydrogenation process of the sample was monitored by an in situ synchrotron radiation X-ray diffraction measurement system installed on beamline BL14B1, SPring-8 [3].

Figure 2 shows in situ synchrotron radiation X-ray diffraction profiles of the sample under high pressure and temperature. The bottom profile was taken when the sample was pressurized to 9 GPa at room temperature. All the Bragg peaks that appeared in the profile were indexed by a unit cell of $Al_{13}Fe_4$ alloy, indicating that no structural phase transition occurred during pressurization. When the sample was heated to around 600 °C, the internal hydrogen source evolved hydrogen, and the sample was immersed in fluid hydrogen. Simultaneous to the hydrogen evolution, the peaks intensities from $Al_{13}Fe_4$ began decreasing and new Bragg peaks began to appear. The Bragg peaks from $Al_{13}Fe_4$ vanished approximately 5 min after the
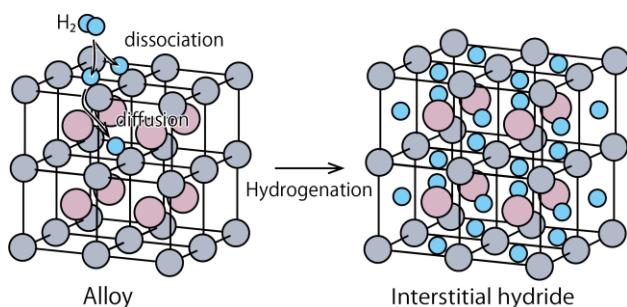

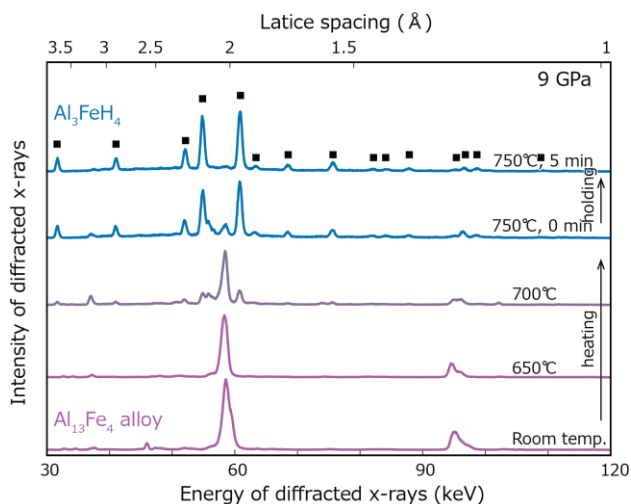Figure 1. Schematic of hydrogenation reaction of a hydrogen storage material.

Figure 2. Series of in situ synchrotron radiation X-ray diffraction profiles recorded when $Al_{13}Fe_4$ alloy was hydrogenated to 9 GPa.

Figure 3. Schematic of the crystal structure of Al_3FeH_4.

sample was heated to 750 °C. The newly appeared Bragg peaks were indexed by a unit cell of a novel hydride, Al_3FeH_4. Thus, we determined the hydrogenation pressure–temperature conditions of $Al_{13}Fe_4$ alloy under high pressure and temperature using in situ synchrotron radiation X-ray diffraction technique. The obtained Al_3FeH_4 retained its crystal structure during the process of cooling to room temperature and decompression to ambient pressure and could be recovered at ambient conditions.

The obtained hydride recovered at ambient conditions was examined for hydrogen release upon heating using a thermogravimetric-mass spectrometer. The hydrogen evolution from the hydride started at approximately 150 °C. The gravimetric hydrogen density calculated from the weight loss during hydrogen release was 2.9 wt%. This value is comparable to that of typical hydrogen storage alloys such as $LaNi_5$ (1.4 wt%) and $TiFe$ (1.9 wt%). The crystal structure of the sample after hydrogen release was the same as that of $Al_{13}Fe_4$.

Because the decomposition temperature and pressure conditions of hydrides can be determined using in situ synchrotron radiation powder X-ray diffraction, the thermodynamic stability of hydrides can be evaluated from these results. The results showed that Al_3FeH_4 had the potential to be thermodynamically stable near ambient conditions; that is, thermodynamically, this alloy had the potential to be used for hydrogen storage near ambient pressure. At present, however, the hydrogenation reaction requires a high pressure of more than 7 GPa. We believe that this is because the chemically stable surface oxide layer on the $Al_{13}Fe_4$ alloy inhibits the hydrogenation reaction. If the effect of the oxide layer could be suppressed in some way, hydrogen storage could be realized using only aluminum and iron, which are the cheapest and most industrially important metal combinations. We are currently studying the reduction in the hydrogenation pressure.

Why does Al_3FeH_4 remain stable at ambient conditions even though it deviates from the conventional guidelines for hydrogen storage materials? We believe that the key point lies in the bonding between metal and hydrogen. To investigate the stabilization mechanism of Al_3FeH_4, the crystal structure was investigated using neutron and synchrotron radiation X-ray diffraction techniques. A schematic of the crystal structure obtained is shown in Fig. 3. The arrangement of the metal atoms
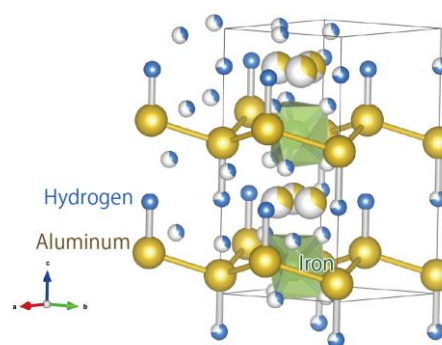
changed significantly owing to hydrogenation. This indicates that Al_3FeH_4 may be a different type of hydride from the interstitial hydride, in which hydrogen is located at interstitial sites in the metal lattice.

The bond length between aluminum and hydrogen and between iron and hydrogen in Al_3FeH_4 were compared with those in known hydrides, and the results showed that they were close to those in hydrides with a covalent nature. It was also observed that the structural units in Al_3FeH_4 were similar, but not perfectly matched, to the typical structural units found in hydrides with a covalent nature. For example, observing the bonds between Fe and hydrogen in Al_3FeH_4, the bond lengths and arrangements were noted to be similar to those of octahedral $[FeH_6]^{4-}$ complex anions present in other iron complex hydrides. However, it was also observed that the structural unit in Al_3FeH_4 had 1/3 partial occupancy of six hydrogen sites and was distorted from the octahedral structure. It is likely that hydrides that deviate from conventional guidelines are stabilized by a peculiar bonding nature that does not fit the conventional classification of hydrides. In the future, we aim to obtain guidelines for the synthesis of this new class of hydrides through further experimental elucidation of their electronic structures.

Acknowledgments

References

1. A. Züttel, Mater. Today **6**, 24 (2003).
2. H. Saitoh, T. Sato, M. Tanikami, K. Ikeda, A. Machida, T. Watanuki, T. Taguchi, S. Yamamoto, T. Yamaki, S. Takagi, T. Otomo, and S. Orimo, Mater. Des. **208**, 109953 (2021).
3. H. Saitoh, A. Machida, and K. Aoki, Chinese Sci. Bull. **59**, 5290 (2014).
4. K. Momma and F. Izumi, J. Appl. Crystallogr. **41**, 653 (2008).

Development of an apparatus for Bragg coherent X-ray diffraction imaging at SPring-8

OHWADA Kenji

Coherent X-ray Research Group, Synchrotron Radiation Research Center

The demand for structural characterization in nano- to micrometer scales, also called mesoscale regions, is rapidly increasing. For example, in the field of ferroelectrics, the *size effect* [1-3] --the dielectric properties of ferroelectric fine particles strongly depend on the particle size-- is well-known but their structural origin is undiscovered. In the case of $BaTiO_3$ fine particles, which have attracted considerable scientific and industrial interest over the past few decades, the dielectric constants have been reported to increase as the average particle size decreases and rapidly decrease below the critical size [4,5]. This cannot be confirmed even when we consider only perovskite-type unit cells. Currently, it is suggested that the particle is composed of a core region with a tetragonal crystal system and a shell region with a cubic crystal system. A gradient lattice strain layer (GLSL) [6] bridges the core and shell regions, and nanosized ferroelectric domains exist in the core region. To obtain a true picture of what occurs within a $BaTiO_3$ fine particle, it is essential to precisely investigate the structure of individual single particles, including the particle size, shape, and global structure (such as domains and GLSL) in nano- to-micrometer scales.

Coherent X-ray diffraction imaging (CDI) [7] is a highly effective technique for visualizing the structure of nano- to micrometer particles. CDI is a lens-less imaging technique that was rapidly developed following the availability of coherent X-ray light sources, the 3rd generation synchrotron light sources, such as SPring-8. Several CDI techniques are in use at present [8]; however, the following approach is common to all techniques. If an object is illuminated by coherent X-rays, the far-field diffracted wave is proportional to its Fourier transform. This situation guarantees the feasibility of image reconstruction. However, the diffracted images are actually measured as a square of the Fourier transform, and the phase information of the diffracted wavefield is lost; therefore, we cannot obtain the image using a simple inverse Fourier transform. This is called a phase problem. However, the image of an object can be reconstructed using a phase-retrieval algorithm. The diffracted images must be sampled at a frequency that is finer than the Nyquist interval.

Here, we focus on the Bragg CDI [9] technique for visualizing individual fine particles. Bragg-CDI is a method dedicated to crystalline fine particles, in which Bragg scattering can be obtained. In Bragg-CDI, a fine particle is illuminated by coherent X-rays and the diffraction patterns around the Bragg position are measured in three dimensions. Therefore, a three-dimensional image of the fine particles can be obtained by the phase retrieval of the diffraction patterns. The retrieved amplitude and phase are related to the electron density and displacement/strain field of the crystal lattice in the fine particles, respectively [10]. Because the Bragg scattering profile and intensity are sensitive to the degree of decoherence of the crystal lattice, the Bragg CDI method can sensitively image the displacement or strain field in fine particles.

Because the orientation of particles is random in a powder, polycrystalline, or ceramic sample, the Bragg-CDI technique is an efficient tool for investigating individual particles in such samples. Because the Bragg peaks of individual particles can be separated in the scattering space, individual particles can be distinguished from their neighbors. Moreover, in most cases, three-dimensional data can be obtained by changing the crystal angle by an order of 1°, which is an advantage over other CDI techniques.

The Bragg-CDI method and related techniques have already been developed in the United States (Advanced Photon Source) and applied to the study of various nanoparticles [11-14]; however, no dedicated apparatus for Bragg-CDI exists in Japan. Thus, we aim to construct an apparatus for investigating the structure of individual fine particles using the Bragg-CDI method. The Bragg-CDI method and precise X-ray structural analysis of individual fine particles are key techniques for obtaining a true picture of what occurs in a single particle.

In the field of fine particle development, the scanning electron microscope (SEM) is frequently used for characterizing the particles. In this case, the shape and surface of the particles can be observed; however, information on the internal structure (strain and domains) and the shape and surface of the back of the particle cannot be obtained. Furthermore, particles in devices such as deep inside multilayer ceramic capacitors (MLCCs) cannot be measured using electron beams. The use of (hard) X-rays overcomes this disadvantage.

In this study, we develop an apparatus for Bragg-CDI and perform the three-dimensional imaging of some fine particles using the apparatus [15-16].
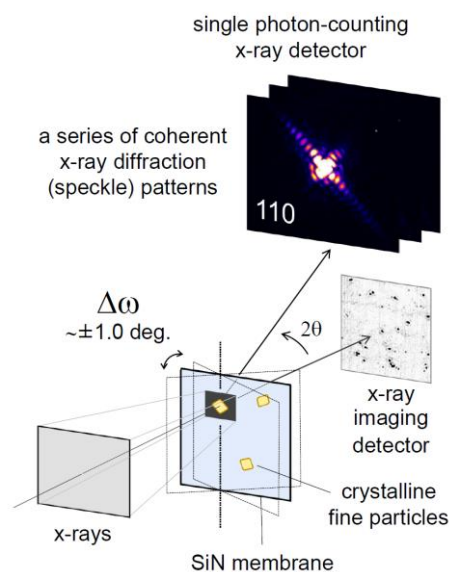

Fig. 1 Schematic drawing of the setup for Bragg coherent X-ray diffraction imaging. Speckle patterns were drawn using ImageJ [17].
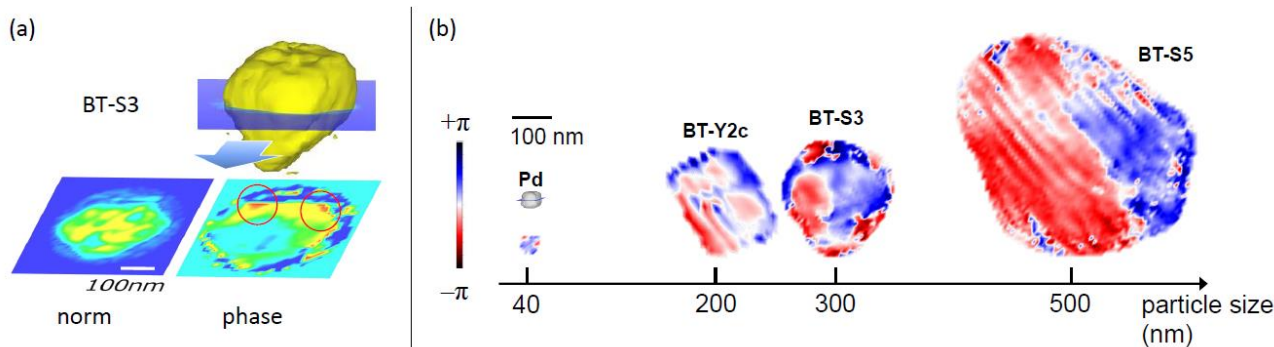
Fig. 2 (a) Reconstructed 3D image of a BaTiO₃ fine particle and cross-sectional drawings of norm (corresponds to the electron density) and phase (corresponds to the strain). (b) Phase (strain) distribution for a series of samples: Pd, BT-Y2c, BT-S3, and BT-S5. These figures were drawn using VESTA 3. [19])

: The Bragg-CDI apparatus was developed at BL22XU in SPring-8. Figure 1 shows the schematic of the experimental setup. The X-ray energy is typically 8 keV. Fine particles were dispersed on the SiN membrane or STEM grid, which did not disturb the coherency of the X-rays. The membrane/grid was set on a sample holder and inserted into a vacuum chamber specially designed for Bragg CDI measurements [16]. The X-rays were focused using a refractive lens (Karlsruhe Institute of Technology) to approximately 2×2 (V × H) μm², with a focal length of 1.0 m. A fine particle on the SiN membrane was illuminated by the focused X-rays, and the diffracted X-rays were collected by a single photon-counting two-dimensional X-ray detector, that is, Eiger500k (Paul Scherrer Institute) or Pilatus300k (DECTRIS). A typical coherent X-ray diffraction pattern is shown in Fig.1. One can clearly see a typical coherent X-ray diffraction pattern, the so-called speckle pattern. We collected three-dimensional speckle patterns around the Bragg position by changing the Bragg angle (ω-scan) to within ±1.0 °. with a step size of typically 0.01°. Using the three-dimensional Bragg diffraction data, we reconstructed three dimensional images of the fine particles. Phase retrieval of the observed diffraction patterns was carried out using a series of hybrid input output (HIO) and error reduction (ER) algorithms [18], which are frequently used in CDI. Three types of BaTiO₃ and Pd particles were prepared: Pd with an average size of 40 nm (Kyoto University and Kyushu University), BT-Y2c with an average particle size of 200 nm and a cube-like shape (Yamanashi University), and BT-S3 and BT-S5 with average sizes of 300 and 500 nm (Sakai Chemical Industry Co., Ltd.), respectively.

Figure 2(a) shows a reconstructed 3D image of fine BaTiO₃ (BT-S3) particles with a size of ~300 nm. Cross-sectional drawings of the norm and phase, which correspond to electron density and strain, respectively, are also shown. Stress concentration, as indicated by the red circles, is observed at the outer shell of the particle. We could observe the 3D structures of an individual whole single particle, including particle size, shape, and strain within 10-nanometer resolution. Figure 2(b) shows the phase (strain) distribution of a cross-section for a series of samples of various sizes obtained by the Bragg-CDI method. Because of the introduction of the vacuum chamber, as mentioned above, we could measure particles with a wide variety of sizes, from 40 nm to 500 nm. The inhomogeneities of the phase shown in Fig. 2(b) correspond to the strains or phase defects associated with the grain boundaries inside the particles. To clarify this supposition, further investigations on changing the sample environments are required and are now actively under construction.

In summary, the shape and size of the particles were successfully reconstructed. The details of the internal structure and reverse surface of the particles were also obtained. This information is not available from SEM measurements. Our technique can be used to study particles as small as ~ 40 nm in size. Bragg-CDI is an effective technique for investigating nanosized crystalline particles and will open the door to studying particles located within devices, such as MLCCs, which are inaccessible by electron beam techniques.

References
1. G. Arlt et al., J. Appl. Phys. **58**, 1619 (1985).
2. K. Ishikawa et al., Phys. Rev. B **37**, 5852 (1988).
3. T. Yamamoto et al., Jpn. J. Appl. Phys. **32**, 4272 (1993).
4. S. Wada et al., Jpn. J. Appl. Phys. **42**, 6188 (2003).
5. T. Hoshina, J. Ceram. Soc. Jpn. **121**, 156-161 (2013).
6. T. Hoshina et al., Appl. Phys. Lett **93**, 192914 (2008).
7. J. Miao et al., Nature **400**, 342 (1999).
8. J. Miao et al., Science **348**, 530 (2015).
9. I. Robinson et al., Rev. Lett. **87**, 195505 (2001).
10. I. Robinson et al., Nat. Mater. **8**, 291 (2009).
11. S. O. Hruszkewycz et al., Phys. Rev. Lett. **110**, 177601 (2013).
12. W. Cha et al., Phys. Rev. Lett. **117**, 225501 (2016).
13. D. Karpov et al., Nat. Commun. **8**, 280 (2017).
14. A. Ulvestad et al., Nat. Mat. **16**, 565 (2017).
15. K. Ohwada et al., Jpn. J. Appl. Phys. **58**, SLLA05 (2019)
16. N. Oshime et al., Jpn. J. Appl. Phys. **60**, SFFA07 (2021).
17. M. Abramoff et al., Biophotonics Int. **11**, 36 (2004).
18. J. R. Fienup, Appl. Opt. **21**, 2758 (1982).
19. K. Momma et al., J. Appl. Crystallogr. **44**, 1272 (2011).

Automated stopping of spectral measurements with active learning

UENO Tetsuro

Magnetism Research Group, Synchrotron Radiation Research Center

An improvement in experimental efficiency is essential in materials science. The research and development of materials with enhanced functionality and the discovery of novel materials can be accelerated through high-throughput experiments. 'Measurement informatics' is a methodology to enhance experimental efficiency using machine learning techniques. Active learning is a machine learning scheme to obtain predictive models with high precision at a limited cost through the sophisticated selection of samples for labelling. We have previously developed a method to improve the efficiency of X-ray magnetic circular dichroism (XMCD) spectral measurements with active learning [1]. XMCD spectroscopy is a derivative experimental technique of X-ray absorption spectroscopy (XAS) that uses circularly polarized X-rays to investigate the element-specific magnetic properties of materials. The XMCD spectral measurement with active learning depends on the magnetic moment evaluated using the predicted spectrum as the stopping criterion. This condition limits the method to a spectral measurement in which the relationship between the spectrum and physical parameter is known. Moreover, the physical parameters must be evaluated immediately from the spectrum to be included in the active learning cycle of the measurement and Gaussian process regression (GPR). Generally, the evaluation of physical parameters from the spectra is not straightforward; for example, a comparison between the experimental and theoretical spectra is required. To apply spectral measurements with active learning to general types of spectra, a stopping criterion without a physical parameter is required.

In this study, we applied a universal stopping criterion for XAS spectral measurements using active learning [2]. The stopping criterion is based on the stability of expected generalization errors [3]. This stopping criterion is completely evaluated on a mathematical basis; therefore, it is applicable to general spectral measurements, whose relationship with the physical parameter is unknown.

Figure 1 shows a flowchart of a spectral measurement with active learning. Spectral measurement with active learning consists of the following steps: (1) First, initial spectral data $\mathbf{Y}_0(\mathbf{X}_0)$ are sampled. Here, $\mathbf{Y}_0 = (y_i, \ldots, y_j)$ represents the spectral intensity at energy point $\mathbf{X}_0 = (x_i, \ldots, x_j)$. (2) Subsequently, GPR is applied to the initial data and mean μ_n and standard deviation σ_n for each energy point are evaluated. $n = 0, 1, \ldots$ represents the number of samplings ($n = 0$ for initial sampling). Mean μ_n is regarded as the predicted spectrum. The stopping criterion is evaluated based on the results of the GPR fitting. (3) If the stopping criterion is not satisfied, then next sampling point x_{next} is automatically determined based on the acquisition function. (4) Subsequently, a new energy point is sampled and added to the measured data, $\mathbf{Y}_n = (y_i, \ldots, y_{\text{next}}, \ldots, y_j)$. Finally, by repeating process (2), GPR is applied to $\mathbf{Y}_n(\mathbf{X}_n)$. Processes (2)–(4) are repeated until the stopping criterion is satisfied.

Approximating the spectrum by GPR is considered to be a problem in supervised learning. In this setting, the goodness of approximation is evaluated using the average prediction error of the intensity at an unseen energy point, which is called the generalization error. The error ratio is defined using the generalization error as the stopping criterion. Figure 2 shows a schematic of the stopping criterion with the error ratio. Error ratio λ_n is evaluated for each active learning cycle, and the measurement is stopped when λ_n becomes smaller than predetermined threshold λ.

We applied the aforementioned method to simulated noise-free Ni $L_{2,3}$ XAS of Ni^{2+} to verify the effectiveness of the overall strategy. XAS spectra were simulated using CTM4XAS [4]. Figures 3(a)–(f) show snapshots of the GPR fitting of XAS. In Fig. 3(a), randomly selected initial data points and GPR fitting are shown. The covariance function exhibited a large standard deviation between the sampled data points, and the next sampling point was chosen from the x values with a large value of the acquisition function. GPR fitting after several samplings is shown in Fig. 3(b). A rough spectral shape appeared; however, the standard deviation was still large. Figure 3(c) shows the GPR fitting after 50 samplings. Satellite peaks appeared around the L_3 main peak, and multiplet structures appeared around the L_2 peak. Figures 3(d)–(f) show the results for different stopping timings, that is, different thresholds λ. The standard deviation was relatively small compared to the intensities of the L_3 and L_2 peaks in the entire energy range. The intensity relationships of the multiplet structures around the L_2 peak were correctly approximated. In Figs. 3(d) and 3(e), the difference between the GPR fitting for different thresholds appears only in the standard deviations around the non-peak regions. As shown in Fig. 3(f),
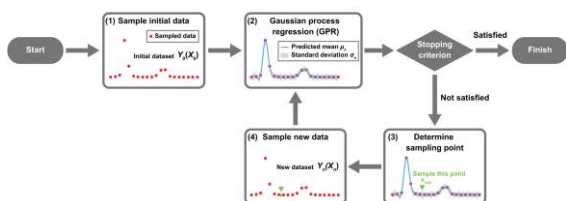

Figure 1. Flowchart of the spectral measurement with active learning. T. Ueno *et al*., npj Comput. Mater. **7**, 139, (2021); licensed under CC BY 4.0. Modified from the original.
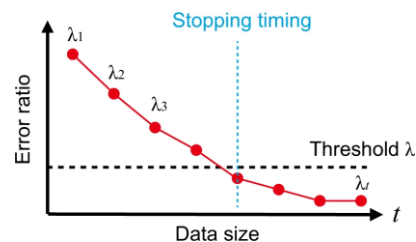
Figure 2. Schematic of the stopping criterion with the error ratio. T. Ueno *et al*., npj Comput. Mater. **7**, 139, (2021); licensed under CC BY 4.0.
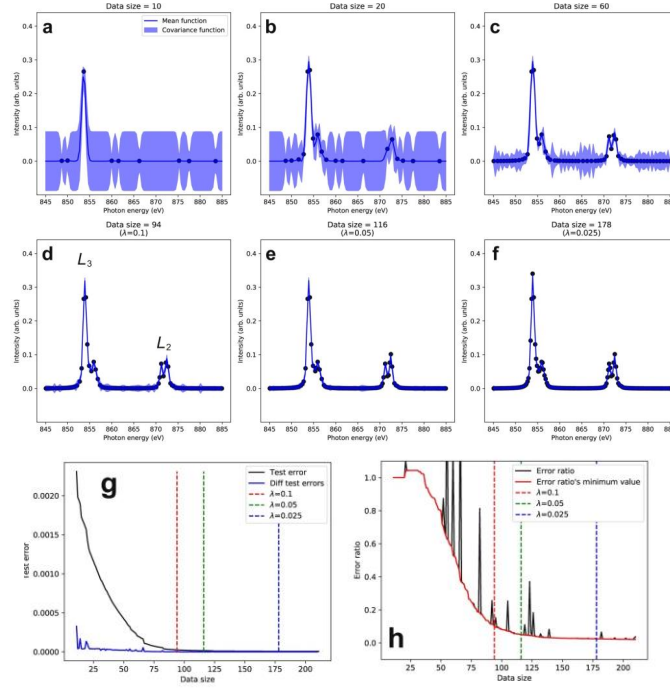
Figure 3. Gaussian process regression for data size of (a) 10 (initial sampling), (b) 20, (c) 60, (d) 94 ($\lambda = 0.1$), (e) 116 ($\lambda = 0.05$), and (f) 178 ($\lambda = 0.025$). (g) Test error versus data size. (h) Error ratio versus data size. T. Ueno *et al.*, npj Comput. Mater. **7**, 139, (2021); licensed under CC BY 4.0. Modified from the original.

the GPR fitting for a data size of 178 was almost the same as the GPR fitting for a data size of 116, but an increase in sampling points around the peak region was observed.

To visualize the progress of the spectral measurement and the stopping timing, the test error and error ratio versus data size are shown in Figs. 3(g) and 3(h), respectively. As shown in Fig. 3(g), the test error steeply decreased with increasing data size as compared to the error ratio in the initial stage of the measurement and converged to a constant value. As shown in Fig. 3(h), the error ratio decreased with increasing data size and converged to an almost constant value. The spikes in the error ratio resulted from the subtraction of the test errors at the steps used to evaluate the upper bound of the test error. The spikes in the error ratio coincided with the spikes in the difference in the test error between the n-th and (n-1)-th sampling. Spikes are inevitable because discontinuous improvement in test errors occasionally arises in active learning. The minimum value of the error ratio is plotted in Fig. 3(h). It was revealed that the minimum value of the error ratio gradually decreased with an increase in the data size. Therefore, immediate early termination of the measurement could be avoided. The vertical dashed lines in Figs. 3(g) and 3(h) indicate the stopping timings for different thresholds corresponding to the GPR fitting shown in Figs. 3(d)–(f). These results indicated that the automated stopping of the XAS measurement based on the generalization error provided GPR fitting with small errors from the ground truth spectrum with a reduced data size.

The XAS spectral measurement with active learning was applied to other spectra, such as simulated Co^{2+} and Mn^{2+} $L_{2,3}$ XAS and experimental Co, Ni, and Mn $L_{2,3}$ XAS for Co and Ni metals and MnO_2 powder. It was concluded that the spectral measurement with active learning was effective for XAS of various elements and with experimental noise.

In summary, we applied a stopping criterion based on the stability of the expected generalization errors for XAS spectral measurements with active learning. This stopping criterion could be evaluated from the self-contained information of GPR fitting. The automated stopping of the XAS spectral measurement was realized with an approximated XAS spectrum with sufficient accuracy. The proposed method can be applied to not only spectral measurements but also other types of measurements. It is expected to enhance experimental efficiency and pave the way for autonomous experimental systems in materials science.

Acknowledgments

References

1. T. Ueno, H. Hino, A. Hashimoto, Y. Takeichi, M. Sawada, and K. Ono, npj Comput. Mater. **4**, 4 (2018).
2. T. Ueno, H. Ishibashi, H. Hino, and K. Ono, npj Comput. Mater. **7**, 139 (2021).
3. H. Ishibashi and H. Hino, arXiv:2104.01836v2 [stat.ML] (2021).
4. E. Stavitski and F. M. F. de Groot, Micron **41**, 687 (2010).

Theoretical study on the time-resolved structure factor in a photoexcited Mott insulator on a square lattice

TSUTSUI Kenji

Condensed Matter Theory Group, Synchrotron Radiation Research Center

Ultrafast optical pulses are a common tool for investigating novel nonequilibrium phenomena in strongly correlated electron systems. One typical method using this tool is the pump-probe optical technique, which has been widely applied to various strongly correlated materials. The pump-probe technique can detect two-particle excitation but cannot observe momentum-dependent collective excitation owing to the negligibly small momentum transfer of probe photons. Conversely, time- and angle-resolved photoemission techniques can probe momentum-dependent electronic excitation after pumping; however, they are limited to a single-particle process, where collective excitation appears indirectly.

The recent development of time-resolved resonant inelastic X-ray scattering (trRIXS) has opened a new avenue for probing collective two-particle excitation, from which novel photoinduced non-equilibrium phenomena can be investigated in a wide range of momentum and energy spaces. RIXS tuning of incident X-rays for the L edge in transition metals can probe not only charge excitation but also magnetic excitation. Motivated by this development, we theoretically investigated momentum-dependent spin dynamics that evolve after pumping within a femtosecond timescale in an antiferromagnetic Mott insulator on a square lattice [1–3]. Characteristic temporal oscillations were demonstrated for the static spin structure factor, exhibiting an antiphase behavior in two orthogonal directions in momentum space: parallel and perpendicular to the electric field of the pump pulse. By analyzing a time-dependent wave function after pumping, we found that the oscillation period was determined by bimagnon excitation in the Mott insulator. This theoretical prediction will be confirmed for Mott insulating cuprates and iridates once trRIXS progresses to a femtosecond timescale.

To describe the Mott insulating states in cuprates, we used a single-band Hubbard Hamiltonian H_0 on a square lattice at half-filling, including the nearest-neighbor (t_h), next-nearest neighbor (t'_h) hopping terms, and on-site Coulomb interaction (U) term. We set $U/t_h = 10$ and $t'_h/t_h = -0.25$, which are typical values for cuprates, with $t_h \sim 0.35$ eV. Hereafter, we use $t_h = 1$ as the energy unit and $1/t_h$ as the time unit. An external spatially homogeneous electric field applied along the x-direction via Peierls phase substitution was incorporated in the hopping terms, leading to the time-dependent Hamiltonian H(t). The vector potential $A(t) = A_0\exp[-(t-t_0)/(2t_d^2)]\cos[w_p(t-t_0)]$ was introduced in the phase, where a Gaussian-like envelope centered at t_0 has a temporal width t_d and a central frequency w_p. We set $A_0 = 0.5$, $t_0 = 0$, $t_d = 0.5$, and $\omega_p = U$.

The time-dependent wave function $|\psi(t)\rangle$ is described by the time-dependent Schrödinger equation. When a time step Δt between two wave functions is as small as $\Delta t = 0.01$, the solution to the Schrodinger equation is given by $|\psi(t+\Delta t)\rangle = \exp[-iH(t)\Delta t]|\psi(t)\rangle$. To calculate the solution, we employed sequential operations of H(t) based on the Taylor expansion: $|\psi(t+\Delta t)\rangle = S_{l=0}|\phi_l\rangle$, where $|\phi_0\rangle = |\psi(t)\rangle$ and $|\phi_{l+1}\rangle = -iH(t)\Delta t$ /(l+1) $|\phi_{l+1}\rangle$. The summation can be truncated if the norm $\langle\phi_M|\phi_M\rangle$ is sufficiently small.

To calculate the dynamic charge and spin correlation functions and the K-edge RIXS spectrum, a real-time representation of the time-dependent cross section has been previously used [4,5]. In this study, we used the spectral representation of dynamic correlation functions, regarding $|\psi(t)\rangle$ as an initial state, which is easily formulated for systems without time-dependent terms in their Hamiltonians. Applying this formalism to a time region after turning off the pump pulse, t > t_{off}, where the Hamiltonian is time independent, we obtained the time-resolved charge and spin dynamic correlation functions with momentum **q** and frequency ω, denoted by N(**q**,ω;t) and S(**q**,ω;t), respectively [1].

Fig. 1 shows the dynamic charge structure factor at t = 5 and N(**q**,ω;t=5). The factor N(**q**,ω) before pumping exhibited momentum-dependent excitations across the Mott gap, which has been observed by Cu K-edge RIXS in insulating cuprates. After pumping, an in-gap excitation emerged inside the Mott gap below ω ~ 7, with a broad spectral weight. The momentum dependence of the in-gap spectral weight was qualitatively similar to that of N(**q**,ω) for the two-hole-doped 4 × 4 Hubbard model; however, its center of gravity was clearly higher in energy and its spectral distribution was sharper. These differences demonstrate the contrasting behaviors of chemical doping and photodoping and
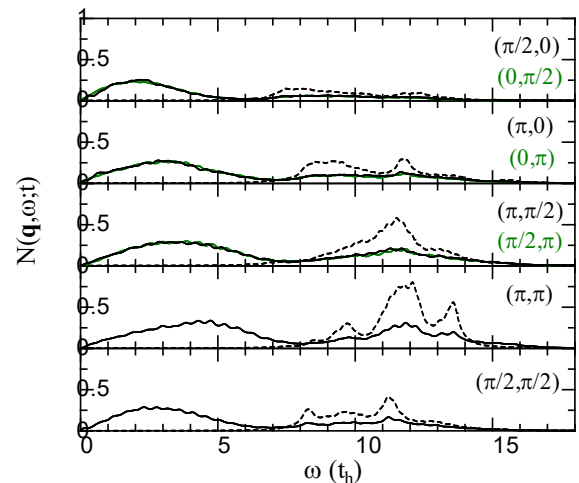
Fig. 1 Dynamic charge structure factor before and after pumping for the half-filled 4 × 4 Hubbard lattice with $t_h = 1$, $t'_h = -0.25$, and U = 10. The black dashed line on each panel represents the equilibrium N(**q**,ω) for **q** denoted in the panel. The black and green solid lines represent N(**q**,ω; t = 5) for **q** denoted by the same color in each panel.
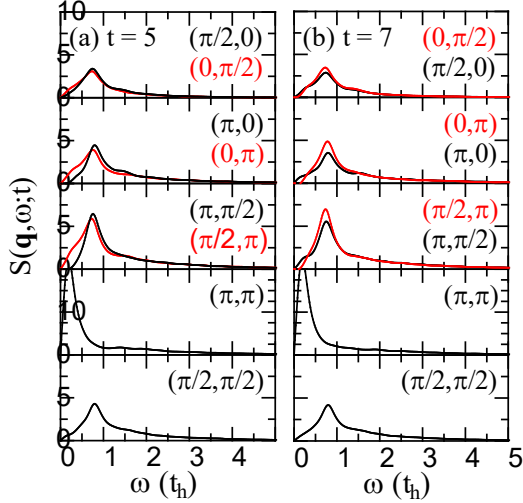
Fig. 2 Dynamic spin structure factor at t = 5 (a) and t = 7 (b) after pumping for the half-filled 4 × 4 periodic Hubbard lattice with $t_h = 1$, $t'_h = -0.25$, and U = 10. Momenta **q** are shown in each panel and their color is the same as that of the solid lines.

Fig. 3 Time-resolved static spin structure factor S(q;t) for the half-filled 4 × 4 Hubbard lattice with $t_h = 1$ and U = 10. The color of the solid lines corresponds to the color of the **q** value denoted in the panel.

may be caused by a drastic change in the electronic state owing to photoirradiation.

Fig. 2 shows the dynamic spin structure factor S(**q**,ω;t) at t = 5 (a) and t = 7 (b). At t = 5, the weight at $(\pi/2,0)$ was slightly larger than that at $(0,\pi/2)$, as shown in Fig. 2(a). Interestingly, the intensity was strongly time-dependent; at t = 7, the intensity at $(\pi/2,0)$ was smaller than that at $(0,\pi/2)$, as shown in Fig. 2(b). This indicates the presence of an oscillation in the spectral intensity as a function of t.

Because the oscillation of the spectral weight causes a change in the integrated intensity with respect to ω, it is useful to investigate the time-resolved static spin-structure factor S(**q**;t), as shown in Fig. 3. To calculate S(**q**;t), we introduced various boundary conditions and averaged them to minimize finite-size effects. As presented in Fig. 3, applying a pumping pulse enhanced the magnitude of S(**q**;t) for small q, whereas this reduced its magnitude for **q** = $(\pi,\pi/2)$ and $(\pi/2,\pi)$ as well as for (π,π) (~40 % reduction, but not shown here). This is because the resonant photoirradiation on the antiferromagnetic Mott insulator destroys the short-range antiferromagnetic correlation, leading to the suppression of spin correlation for large **q** values but enhancement for small **q** values. S(**q**;t) exhibited oscillations, except for **q** = $(\pi/2, \pi/2)$; the oscillations were antiphase between two momenta equivalents such as $(\pi/2,0)$ and $(0,\pi/2)$. We found that the antiphase behavior originates from the B_{1g} channel of the two-magnon excitation in the antiferromagnetic Mott insulator [1–3]. We expect that trRIXS will be able to detect such oscillations in the near future.

Collaborators

Takami Tohyama and Kazuya Shinjo
Department of Applied Physics, Tokyo University of Science

Acknowledgments

References

1. K. Tsutsui, K. Shinjo, and T. Tohyama, Phys. Rev. Lett. 126: 127404 (2021).
2. T. Tohyama, K. Shinjo, S. Sota, and K. Tsutsui, J. Phys.: Conf. Ser. 2207: 012028 (2022).
3. T. Tohyama, K. Shinjo, S. Sota, and K. Tsutsui, J. Phys.: Conf. Ser. 2164: 012049 (2022).
4. Y. Wang, M. Claassen, B. Moritz, and T.P. Devereaux, Phys. Rev. B 96 235142 (2017).
5. Y. Wang, Y. Chen, C. Jia, B. Moritz, and T.P. Devereaux, Phys. Rev. B 101 165126 (2020).

Research Activities of the Institute of Quantum life Science at KPSI

SHIKAZONO Naoya

Institute of Quantum Life Sciences

Quantum life science has emerged to explore new frontiers in biology from the perspective of the quantum domain to describe the dynamics and functions of cells and organisms. The Institute of Quantum Life Science at the National Institutes for Quantum Science and Technology (QST) was established in April 2019 to pioneer a new field in life sciences. Investigations at the Institute of Quantum Life Science are expected to follow two approaches. The first approach is to figure out whether quantum mechanics play an essential role in biological systems. The second approach is to apply quantum science and its technologies for measuring physical and chemical parameters (i.e. temperature, pressure, and pH) inside the cell at an unprecedented minute level, in order to gain information on the structure and dynamics of biomolecules. Using the above two approaches, the goal of the Institute of Quantum Life Science is to discover the essential principles of life and to apply the knowledge developed during the course of investigation in medical sciences and social activities (Fig. 1). The field of quantum life science is envisaged to produce unanticipated discoveries that will expose the existence of quantum phenomena in nature, ultimately leading to their exploitation, which, in turn, would benefit society. At the Kansai Photon Science Institute (KPSI), three research groups in the Institute of Quantum Life Science are carrying out their research by conducting experiments and computer simulations (Fig. 1).

The Molecular Modeling and Simulation Group aims to understand the *in vivo* function of biomolecules at the atomic level. The group uses computer simulations and bioinformatics based on experimental results, such as crystallographic and scattering data obtained by various types of radiation (x-rays, neutrons, and electrons) and cryo-electron microscopy. The main research target is to determine how the dynamics of protein/DNA/RNA complexes relate to essential cellular functions such as transcription, translation, replication, and repair. One of the focuses of this group is to quantitatively predict the stability of supramolecular complexes such as chromosomes. This year, the research group carried out a simulation to elucidate the overall structure of a protein complex involved in generating circadian rhythms. It is well known that life on Earth has developed circadian rhythms to adapt to daily environmental changes. Cyanobacteria are the simplest organisms with a robust circadian clock; therefore, they have become one of the most useful model organisms for circadian biology. The central oscillator that generates the circadian rhythm in the cyanobacterium *Synechococcus elongatus* PCC 7942 is comprised of three proteins: KaiA, KaiB, and KaiC. From the experimental results of small-angle x-ray scattering (SAXS) and small-angle neutron scattering (SANS) of the protein complex, the group built an atomic model of the overall structure [1]. The implications of this study will lead to a better understanding of how the cyanobacterial circadian clock works, and thus, will provide fundamental insights into circadian biology. The results have been described in an associated report. The group has also been working on the structural mechanism of NSD2, which

regulates the methylation level of nucleosomal histone H3. Several lines of evidence demonstrate the critical importance of the strict regulation of cellular histone H3 methylation. One significant effect of cellular H3 methylation is that it regulates gene expression by controlling the extent of repressive chromatin domains in genomic DNA. NSD2 is a member of the NSD family that catalyzes the mono- and di-methylation of histone H3, and the deregulation of NSD2 activity is implicated in carcinogenesis. In this study, the structure and dynamics of NSD2 binding to histone H3 were simulated, based on the structure obtained using cryo-electron microscopy [2]. The results indicated that mutations associated with cancer increase the tendency of the autoinhibitory loop to adopt an open state, which provides insight into the regulatory mechanisms of NSD2 proteins under normal and oncogenic states. The details are described in the following report.

The main goal of the DNA Damage Chemistry Group is to clarify the nature of DNA damage induced by various agents, particularly damage from ionizing radiation. The group aims to utilize new experimental techniques that can reveal the structure of DNA damage as well as the recognition of DNA damage by repair enzymes at the nanometer scale. The focus of this group is currently on "clustered DNA damage" in which two or more DNA lesions are located within one to two helical turns of DNA (within several nanometers along the DNA). Clustered DNA damage is considered challenging to repair, and thus is a detrimental type of damage induced by ionizing radiation. However, its presence and microstructure remain elusive, as few experimental methods have been able to obtain data on the spatial distribution of DNA lesions. This research group established a novel approach for measuring the localization level of DNA damage by directly visualizing it. Atomic force microscopy (AFM) has a resolution at the nanometer/sub-nanometer scale, and thus, DNA can be directly visualized. The research group labeled DNA damage (abasic sites) by attaching aldehyde reactive probes with biotin and then attaching streptavidin to biotin. The large molecular size enabled the detection of streptavidin using AFM. Abasic sites were directly induced or further revealed by removing the damaged bases by DNA glycosylases after irradiation. Using this method, the complex nature of clustered DNA damage was visualized for the first time. The research group further developed a promising method for detecting clustered DNA damage using fluorescence resonance energy transfer (FRET). In this method, aldehyde/ketone moieties, such as those at abasic sites in irradiated DNA, are labeled by aminooxyl fluorophores. Fluorescence anisotropy enabled the estimation of the apparent base-pair separations between lesions in a cluster produced by an ion track and revealed that the yield of clustered abasic sites increased with increasing linear energy transfer (LET) of the radiation. Both the AFM and FRET approaches confirmed that these novel analyses have the potential to discover the qualitative and quantitative differences in clustered DNA damage produced by various types of ionizing radiation.

Institute of Quantum Life Science

Using cutting-edge quantum technologies and advanced computer simulations, the Institute aims to contribute (1) to the elucidation of the basic principles of life, and in longer term, (2) to the benefit for the everyday life of the society.

Groups at KPSI

Fast processes（～fsec order）,Minute regions（～nm order）

Molecular Modeling and Simulation group
> Structure and dynamics of biomolecules

DNA Damage Chemistry Research Group
> DNA damage detection and damage recognition

Mechanism of Mutagenesis Group
> Novel mutation induction pathways

Basic principles of life

Medical applications, Benefit for the society

Figure 1.

The goal of the Mechanism of Mutagenesis Group is to elucidate the underlying mechanisms causing mutations, which are highly relevant to carcinogenesis and the evolution of life. One aspect of this group's research focuses on events at very early stages (around a femtosecond to picosecond) within a space on the scale of nanometers after energy transfer from ionizing radiation, especially from ions. Using Monte Carlo simulations, the research group demonstrated that when water is exposed to densely ionizing ion particles, some of the secondary electrons ejected from water molecules are trapped within the electric potential created by the ionized water molecules. This result led to the realization that the radial dose near the track of a densely ionizing ion particle is much higher than previously understood. This highly localized energy deposition is considered to produce a high yield of clustered DNA damage and thus has important implications for the drastic effect of ion particles on cells. The research group succeeded in arriving at a deeper understanding of the state immediately after energy was deposited near the radiation track by examining the Debye length of the produced plasma [3]. A detailed description is provided in the associated report. Another research interest of this group is the biological effects of cluster ions. They irradiated bacterium (*B. subtilis*) spores with clustered protons and found that (1) 2 MeV H_2 (clustered proton ions consisting of two) showed a higher lethality per particle than 1 MeV H and (2) 2 MeV H_2 showed a much lower lethality than 340 keV H, which has a similar linear energy transfer (LET) with 2 MeV H_2. The 2 MeV H_2 likely dissociates into a pair of 1 MeV H by losing the bonding electrons at the target surface. This consideration suggests that the deposited energy over the dissociated two protons separated by just several nanometers greatly diminishes the lethal effect. The group also carried out whole-genome sequencing of the irradiated genomes to determine the molecular nature of mutations but failed to find a clear difference between non-clustered and clustered protons. These results suggest that cluster ions are a useful tool for understanding the biological effects resulting from the spatial energy deposited by high LET radiation [4].

Quantum life science is related to the interactions between dynamical phenomena at extremely short time scales and minute length scales, that is, from atto to femtosecond energy transfer processes at the (sub)nanometer scale. Over the long term, the field of quantum life science is expected to produce unparalleled discoveries based on the significance of quantum phenomena in biological systems. To achieve such goals, the research of the three groups of the Institute of Quantum Life Sciences at the KPSI is ongoing.

References

1. Yunoki, Y., Matsumoto, A., Morishima, K., Martel, A., Porcar, L., Sato, N., Yogo, R., Tominaga, T., Inoue, R., Yagi-Utsumi, M., Okuda, A., Shimizu, M., Urade, R., Terauchi, K., Kono, H., Yagi, H., Kato, K., Sugiyama, M. Overall structure of a fully assembled complex in the cyanobacterial circadian clock system by an integrated approach. Nat. Commun. 12, 6605 (2021)
2. Sato, K., Kumar, A., Hamada, K., Okada, C., Oguni, A., Machiyama, A., Sakuraba, S., Nishizawa, T., Nureki, O., Kono, H., Ogata, K., Sengoku, T. Structural basis of the regulation of the normal and oncogenic methylation of nucleosomal histone H3 Lys36 by NSD2. Nat. Commun. 12, 6605 (2021)
3. Moribyashi, K. Debye shield formed by track potential and transport of secondary electrons in heavy ion irradiation. Radiation Physics and Chemistry 184, 109436 (2021)
4. Hase, Y., Satoh, K., Chiba, A., Hirano, Y., Moribayashi, K., Narumi, K. Proton-Cluster-Beam Lethality and Mutagenicity in Bacillus subtilis Spores. Quantum Beam Sci. 5. 25 (2021)

Integrative structure modeling of KaiABC clock protein complex

MATSUMOTO Atsushi

Molecular Modeling and Simulation Group, Institute for Quantum Life Science

Every organism on Earth possesses a circadian rhythm that repeats approximately every 24 h and is driven by a circadian clock. The molecular machinery of the circadian clock in cyanobacteria (Kai-clock) comprises three proteins: KaiA, KaiB, and KaiC. These proteins undergo an association–dissociation cycle, coupled with the phosphorylation–dephosphorylation oscillation of KaiC in the presence of adenosine triphosphate (ATP)[1,2]. During the circadian cycle, the Kai-clock system generates three forms of complexes, two binary complexes KaiAC and KaiBC, and one ternary complex KaiABC, at specific clock phases[3,4] (Fig. 1).

KaiA comprises an N-terminal domain ($_N$A), a canonical linker, and a C-terminal domain ($_C$A), and forms a homodimer (A_2) through $_C$A[5,6]. KaiB assumes a single thioredoxin domain and forms a homotetramer (B_4)[7,8]. KaiC comprises two domains (CI and CII) and forms a homohexamer (C_6) with a double doughnut-like shape[9-11]. The binary complex KaiAC (A_2C_6) is formed by an A_2 dimer and a KaiC hexamer through interactions at the C-terminal tails of the CII domains[12-14]. Another binary complex, KaiBC (B_6C_6), is formed by a KaiC hexamer and six KaiB molecules arranged on top of CI domains[3,15,16]. Regarding the ternary complex KaiABC, the supramolecular architecture and stoichiometry of the complex have been controversial for a long time[17-19]. Recently, a cryo-EM (cryo-electron microscopy) study revealed the structure of the complex ($A_{12}B_6C_6$), in which six A_2 dimers were captured onto the KaiB ring in the B_6C_6 subcomplex[20,21]. However, the $_N$A domains of the A_2 dimers were absent from the structure, suggesting that the domains could fluctuate in the complex. Previously reported mutational studies have indicated that the $_N$A domain is essential for the generation of circadian rhythms[22,23]. Therefore, it is crucial to determine the overall structure of the $A_{12}B_6C_6$ complex, including the locations of $_N$A domains.

Small-angle X-ray and neutron scattering (SAXS and SANS) provide structural information regarding supramolecular complexes in solution[24-26]. We utilized SAXS coupled with size-exclusion chromatography (SEC–SAXS)[27-29] to avoid scattering from undesirable components and inverse contrast-matching SANS (iCM-SANS) to selectively observe scattering originating from KaiA in the $A_{12}B_6C_6$ complex.

We established candidate models of the $A_{12}B_6C_6$ complex computationally, which can reproduce the results of SAXS and SANS (see Fig. 2). We used the crystal structures of a KaiC hexamer (C_6, PDB code: 3dvl)[11] and a ternary complex ($_CA_2$-B-$_{CI}$C, PDB code: 5jwr)[21] comprising two C-terminal domains of the KaiA dimer ($_CA_2$), a KaiB monomer (B), and a CI domain of KaiC ($_{CI}$C) to build a model of the $_CA_{12}B_6C_6$ complex ($A_{12}B_6C_6$ complex without $_N$A domains), which agreed well with the previously reported cryo-EM structure. Subsequently, we combined it with the crystal structure of a full-length KaiA dimer (A_2, PDB code: 1r8j)[20] to obtain the overall structure of the $A_{12}B_6C_6$ complex. However, in this structure, the $_N$A domains overlapped structurally with KaiB, indicating that spatial rearrangements of $_N$A domains were necessary. To remove this
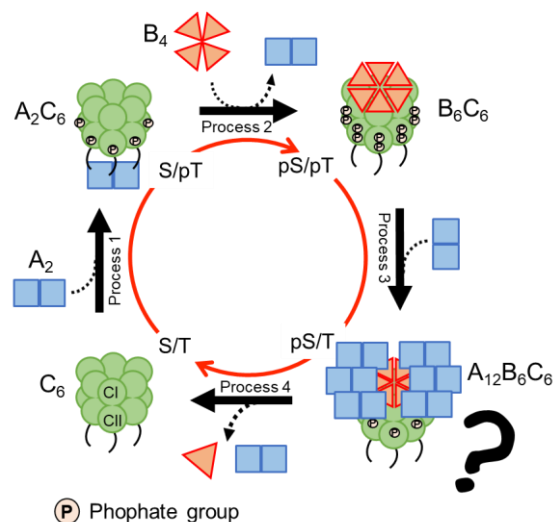
Figure 1: Proposed oscillation scheme for cyanobacterial circadian clock system (Kai clock system). Blue squares, orange triangles, and green spheres represent monomers of KaiA, KaiB, and KaiC, respectively. Two phosphorylated sites, i.e., Ser431 and Thr432, exist in CII domain of KaiC. Phosphorylation cycle is as follows: S/T→S/pT→pS/pT→ pS/T → S/T (p indicates phosphorylated residue). Phosphorylation–dephosphorylation cycle of KaiC is coupled with its association and dissociation with KaiA and KaiB.
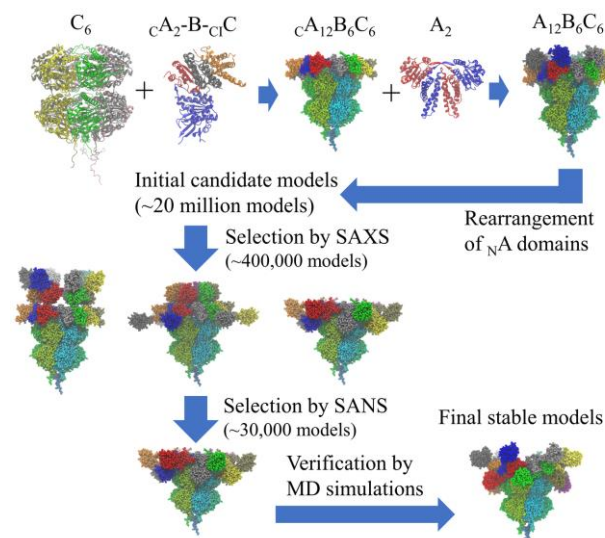
Figure 2: Modeling procedure of overall structure of $A_{12}B_6C_6$ complex.

overlap, we systematically altered the positions and orientations of the individual $_N$A domains. At this stage, we disregarded the linkers connecting the $_N$A and $_C$A domains to reduce the computational cost. Finally, we constructed ~20 million models of the $A_{12}B_6C_6$ complex as the initial structural candidates.

We calculated the scattering curves for each model and selected models that indicated small χ^2 values for both SAXS and SANS. Interestingly, three different types of models agreed well with the SAXS results, but only one of them agreed with the SANS results (Fig. 2). This shows that the combination of multiple experiments is important for structural determination.

After modeling the linkers connecting the $_N$A and $_C$A domains, which were not considered in the previous steps, we performed MD simulations on the models that agreed well with both the SAXS and SANS results to verify their stability in water. This process was necessary because the protein domains were regarded as rigid bodies, and only the exclusive volume of the molecules was considered. In fact, most of the models (> 90%) were unstable and could not maintain small χ^2 values for SAXS and SANS during the simulations; this indicates that the MD simulation may be an effective tool for model selection.

In summary, this study demonstrated that the integrated approach of modern solution scattering methods, i.e., SEC–SAXS and iCM-SANS, as well as computational modeling and molecular dynamics simulation can effectively resolve the structures of supramolecular complexes harboring dynamically fluctuating domains/subunits, such as the KaiABC complex.

References

1   Ishiura, M. *et al. Science* **281**, 1519-1523 (1998).

2   Nakajima, M. *et al. Science* **308**, 414-415 (2005).

3   Chang, Y. G. *et al. Science* **349**, 324-328 (2015).

4   Oyama, K., Azai, C., Nakamura, K., Tanaka, S. & Terauchi, K. *Scientific Reports* **6**, 32443 (2016).

5   Vakonakis, I. *et al. Proc Natl Acad Sci USA* **101**, 1479-1484 (2004).

6   Ye, S., Vakonakis, I., Ioerger, T. R., Li Wang, A. C. & Sacchettini, J. C. *The Journal of Biological Chemistry* **279**, 20511-20518 (2004).

7   Hitomi, K., Oyama, T., Han, S., Arvai, A. S. & Getzoff, E. D. *The Journal of Biological Chemistry* **280**, 19127-19135 (2005).

8   Iwase, R. *et al. The Journal of Biological Chemistry* **280**, 43141-43149 (2005).

9   Mori, T. *et al. Proc Natl Acad Sci USA* **99**, 17203-17208 (2002).

10   Hayashi, F. *et al. Genes to cells: devoted to molecular & cellular mechanisms* **8**, 287-296 (2003).

11   Pattanayek, R. *et al. Molecular Cell* **15**, 375-388 (2004).

12   Yunoki, Y. *et al. Life science alliance* **2** (2019).

13   Pattanayek, R. *et al. The EMBO Journal* **25**, 2017-2028 (2006).

14   Pattanayek, R. *et al. PloS One* **6**, e23697 (2011).

15   Phong, C., Markson, J. S., Wilhoite, C. M. & Rust, M. J. *Proc Natl Acad Sci USA* **110**, 1124-1129 (2013).

16   Sugiyama, M. *et al. Scientific Reports* **6**, 35567 (2016).

17   Kageyama, H. *et al. Molecular Cell* **23**, 161-171 (2006).

18   Mori, T. *et al. PLoS Biology* **5**, e93 (2007).

19   Akiyama, S., Nohara, A., Ito, K. & Maéda, Y. *Molecular Cell* **29**, 703-716 (2008).

20   Snijder, J. *et al. Science* **355**, 1181-1184 (2017).

21   Tseng, R. *et al. Science* **355**, 1174-1180 (2017).

22   Nishimura, H. *et al. Microbiology (Reading, England)* **148**, 2903-2909 (2002).

23   Chen, Q., Liu, S., Yang, L., Zhang, L. & Li, J. *Biochimica et biophysica acta. General Subjects* **1861**, 2535-2542 (2017).

24   Svergun, D. I. *Biophysical Journal* **76**, 2879-2886 (1999).

25   Bernadó, P., Shimizu, N., Zaccai, G., Kamikubo, H. & Sugiyama, M. *Biochimica et Biophysica Acta. General subjects* **1862**, 253-274 (2018).

26   Fejgin, L. A. & Svergun, D. I. *Structure analysis by small-angle X-ray and neutron scattering*.   (Plenum Press, 1987).

27   David, G. & Pérez, J. *Journal of Applied Crystallography* **42**, 892-900 (2009).

28   Ryan, T. M. *et al. Journal of Applied Crystallography* **51**, 97-111 (2018).

29   Inoue, R. *et al. Scientific Reports* **9**, 1-12 (2019).

Oncogenic mutations E1099K and T1150A enhance NSD2 methyltransferase activity by increasing the auto-inhibitory loop dynamics

Amarjeet KUMAR

Molecular Modeling and Simulation Group, Institute for Quantum Life Science

Histone post-translational modifications (PTMs) are distributed throughout chromatin in a context-dependent manner. It is known to regulate diverse genome-related and downstream processes. Alterations, either in the dynamics or distribution of histone PTMs, alter the gene expression profiles of cells. These disturbances are often linked to the development of various pathological conditions in humans [1]. Dimethylation of histone 3 lysine 36 (H3K36me2) is one such PTM, catalyzed by the NSD family member protein NSD2 (also known as WHSC1/MMSET). It incorporates mono- and dimethylation at lysine 36 of histone 3 (H3K36). Aberrant upregulation of H3K36me2 by induced NSD2 overexpression or due to NSD2 point mutations (E1099K and T1150A) is associated with multiple myeloma, lymphoblastic leukemia, and other types of cancers and developmental anomalies in neurons and cardiovascular tissues.
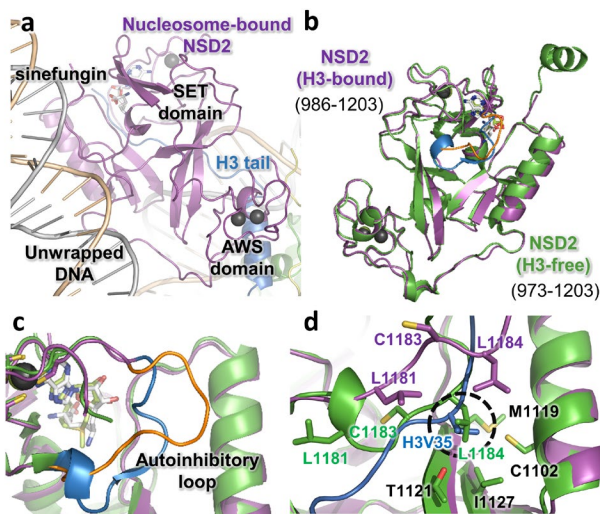
Figure 1. NSD2-nucleosome complex. **a** NSD2 bound to nucleosome with partially unwrapped DNA near the entry/exit site. **b** H3-bound and H3-free NSD2 structure comparison. **c** Comparison of autoinhibitory loop conformation in H3-free (blue) and H3-bound NSD2 (orange). **d** Hydrophobic residues surrounding the H3V35-binding hydrophobic cavity showing the overlap between the positioning of L1184 in H3-free and V35 in H3-bound NSD2 structure.

Biochemical studies have shown that NSD2 has a strong specificity for nucleosomal substrates. Our nucleosome-bound NSD2 cryo-EM structure revealed that nucleosome-NSD2 association requires the removal of one DNA gyre near the entry/exit site to access the H3K36 located between the two DNA gyres in the canonical nucleosome. This leads to the partial unwrapping of DNA at the nucleosomal entry/exit. In this binding mode, NSD2 establishes extensive interactions with the H3 N-terminal tail, H2A C-terminal portion, H3 first α-helix, nucleosomal DNA, and external linker DNA (**Fig. 1a**) [2].
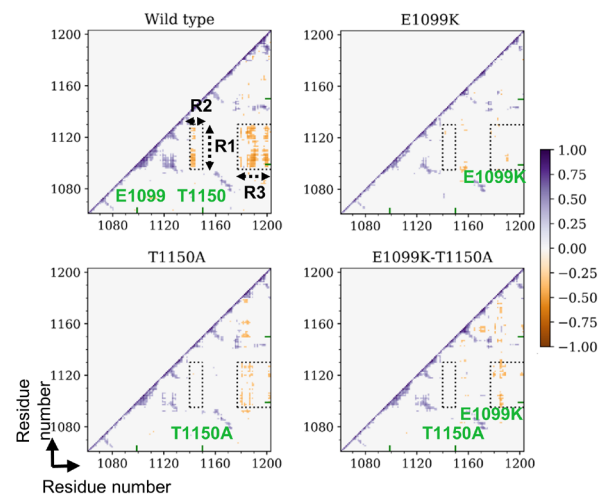
Figure 2. Cross-correlation plots of the residue-wise fluctuation. See the legend in Figure 3 for the definitions of R1, R2 and R3.

The overall structures of the H3-bound and H3-free NSD2 were similar (**Fig. 1b**). However, compared to H3-free NSD2, where the autoinhibitory loop in the SET domain occupies the substrate-binding cleft, assuming a closed conformation, leaving no room for H3 tail accommodation, in the H3-bound NSD2 structure, the autoinhibitory loop adopts an open conformation. (**Fig. 1c**). Point mutations E1099K and T1150A increase NSD2 catalytic activity without increasing its affinity for nucleosomes [2]. There remains a gap in the understanding of the NSD2 catalytic enhancement mechanism following these two point mutations.

To fill this gap, we carried out MD simulations of the H3 free NSD2 wild type and mutants. The NSD2 structure was extracted from the nucleosome-bound complex and used as the starting point for the simulation [2]. Comparative analysis of the MD trajectories based on time-dependent changes in secondary structures and residue-wise contact maps clearly showed that NSD2 wild type, E1099K, T1150A, and the double mutant E1099K-T1150A structures were stable and maintains similar

global conformations, except in the autoinhibitory loop. The autoinhibitory loop remains flexible in all systems [2]. The dynamic cross-correlation analysis of the wild type NSD2 SET domain residue-wise fluctuations showed anti-correlated motions among residues in the regions R1-R2 and R1-R3 (**Fig. 2**), which are absent in the mutants. The absence of anti-correlated motion suggested that the movement of R2 and R3 was independent of R1 in the NSD2 mutants (**Fig. 2**). R1 contained the mutation site E1099 and residues forming the H3V35- and H3P38-binding hydrophobic patches, whereas R2 and R3 constituted the mutation site T1150A and the autoinhibitory loop, respectively (**Fig. 1d and 3a**).

Independent movement of R3 suggests the possibility of autoinhibitory loop adopting an open conformation more frequently, facilitating H3 tail binding to NSD2 mutants. For validation, the open-close motion of the autoinhibitory loop was quantified based on four distance-based locks as shown in **Fig. 3b**. It was observed that the autoinhibitory loop tends to assume an open conformation far more frequently in mutants (9.7%, 6.3%, and 18.8% in the case of E1099K, T1150A, and E1099K-T1150A, respectively) than in the wild type (only 0.86%) (**Fig. 3c**).
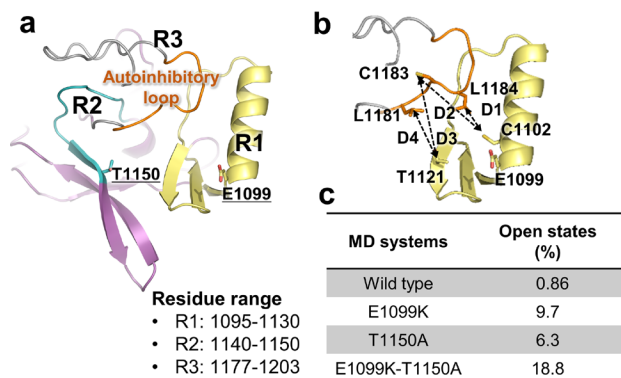
Figure 3. Open-close dynamics of the autoinhibitory loop. **a** Regions R1, R2, and R3 are shown on the NSD2 SET domain structure. **b** Def. of the four distance-based locks to quantify the autoinhibitory open-close dynamics. **c** Table showing the percentage of open autoinhibitory loop conformation in NSD2 wild type and mutant.

A detailed examination of MD trajectories revealed the importance of the interaction between the residue L1181 and the hydrophobic patches (especially T1121 and T1150), whose replacement by alanine leads to NSD2 hyperactivity. Based on the MD simulation results, a working model of NSD2 aberrant catalytic enhancement was proposed. In the wild type H3-free NSD2, the autoinhibitory loop exhibits multiple conformations. However, the hydrophobic interactions between residues L1181, C1183 and L1184 and the hydrophobic patches maintained the autoinhibitory loop in a closed conformation, leaving no space for H3 tail binding. Mutations E1099K and T1150A affect the conformational dynamics of the autoinhibitory loop and promote its tendency to adopt an open conformation, leaving sufficient room for H3 tail-binding. A possible mechanism by which point mutations affect the autoinhibitory loop conformation could be via the network of salt bridge interactions at the base of the H3

binding pocket surrounding the loop (**Fig. 4**). Mutations E1099K and E1099K-T1150A seem to remodel the salt bridge interaction network in the NSD2 wild type by adding a novel salt bridge with D1125, accompanied by a decrease in salt bridge formation between D1123 and K1152. Similarly, in the T1150A mutant, the D1123-K1152 salt bridge formation was seen to decrease (**Fig. 4**).
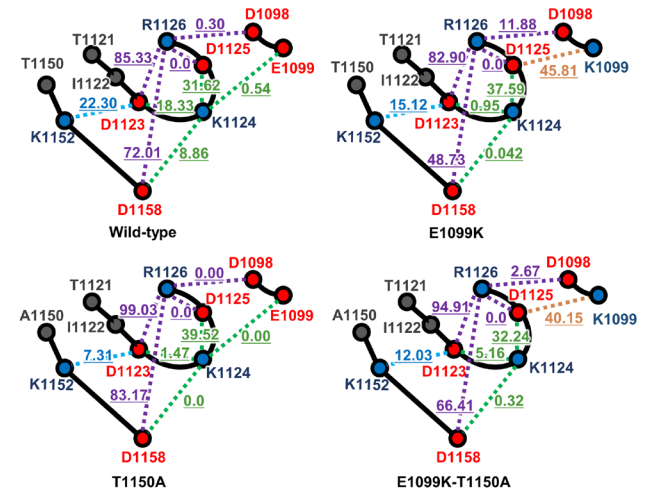
Figure 4. Schematic representation of the residues forming the salt bridge network around the autoinhibitory loop. Dashed lines depict salt bridges between residue pairs with the percentile of bridge formation.

The D1123-K1152 salt bridge connects two β-sheets that form the H3V35 and H3P38 binding patch. Interestingly, the autoinhibitory loop opens when the D1123-K1152 salt bridge is lost. In summary, our study provides insight into the mechanism of catalytic enhancement of NSD2 following oncogenic mutations E1099K and T1150A and facilitates the development of inhibitors against these proteins for cancer treatment.

Collaborators

Ko Sato[1], Keisuke Hamada[1], Chikako Okada[1], Asako Oguni[1], Ayumi Machiyama[1], Shun Sakuraba[2], Tomohiro Nishizawa[3,4], Osamu Nureki[3], Hidetoshi Kono[2], Kazuhiro Ogata[1] and Toru Sengoku[1].
1. Dep. Biochem., YCU, Grad. Sch. Med, Yokohama, Kanagawa, Japan. 2. iQLS, QST, Kizugawa, Kyoto, Japan. 3. Dep. of Bio. Sci., Grad. Sch. Sci., UTokyo, Tokyo, Japan. 4. Grad. Sch. Med. Life Science YCU, Yokohama, Kanagawa, Japan.

Acknowledgments

References

1. Hyun K, Jeon J, Park K, Kim J. *Exp Mol Med* 2017, 49:e324.
2. Sato K, Kumar A, Hamada K, Okada C, Oguni A, Machiyama A, Sakuraba S, Nishizawa T, Nureki O, Kono H, et al. *Nat Commun* 2021, 12:6605.

A Debye shield formed by track potential and transport of secondary electrons under heavy ion irradiation

MORIBAYASHI Kengo

DNA Damage Chemistry Group, Institute of Quantum Life Sciences

1. Introduction

Under heavy ion irradiation, a special physical phenomenon appears near the incident ion path (IP); that is, a strong electric field created near the IP affects the transport of secondary electrons (SEs). A SE is an electron created by incident impact ionization, and the potential created by this electric field is called "track potential (TP)" . This effect is expected to form plasma [1], which contributes to increasing the local dose in this region. The plasma formed by heavy-ion irradiation is assumed to be important; however, this plasma has seldom been studied. To the best of our knowledge, this is because there were no methods to study the plasma produced near the IP before our simulation model was developed [1,2]. Only our simulations [1] succeeded in reproducing the measurement trend of SE yields (Y_{se}) [3]. In this study, we analyzed when, where, and how plasma is created through simulations and Debye shield theory. Furthermore, we studied the effect of this shield on the transport of SEs and TP. The Debye shield decreased the electric field outside the shield itself.

In heavy-ion beam science, SE transport is crucial because SEs transport most of the energy deposited from the incident ion over a wide area. To simulate this transport phenomenon, two types of models were proposed in the early 20th century: free-electron gas and binary collision. In the free-electron gas model, electron plasma, which is estimated to enhance the local dose near the IP, is created. However, (i) the Debye shield is not considered in this model, (ii) it is difficult to incorporate it in a simulation model, and (iii) free-electron gas is far from the real target. In contrast, the binary collision model is easy to employ in large-scale simulations; however, a plasma is not created in this model.

In our simulation model developed based on a binary collision model, we incorporated the effect of the TP on SE transport [1]. We detected from previous simulations [1] that this effect is expected to produce plasma, which increases the local dose near the IP. A similar increase also appeared in free-electron gas models, as mentioned above. We compared our simulations regarding the probability (P_{set}) of SEs escaping TP [1] with the measurement data of the secondary electron yield (Y_{se}) from the insulator KCl target [3]. Note that this trend cannot be explained by the two aforementioned conventional models because TP is ignored in the binary collision model and production rate of electron plasma in SEs is established regardless of the ion impact ionization cross-section σ in the free-electron gas models. Furthermore, we study the Debye shield theory and compare the simulation results with the analytical results.

2. Simulation model

In conventional simulation models based on the binary collision theory, a continuum is employed as the target. To consider a more realistic transport of SEs, we treated individual water molecules in a rectangular target. The procedures followed by the proposed model are summarized below. Using a random number (N_{ran}), the positions of water molecules are randomly determined to obtain N_{mol} in water. Furthermore, we prepared several targets with different molecular locations. For each target, we simulated a heavy ion passing through. The average values of these results are presented in section 4.

A heavy ion is assumed to enter the target perpendicular to its bottom area. Water molecular ions and SEs are produced according to σ, the center of which is located at the center of each molecule. The initial energy and emitted angle of SEs are determined by fitting the measurement functions. To incorporate the effect of TP on the transport of SEs, we considered the Coulomb interaction of the SEs with molecular ions (F_{ei}) produced by the incident ion impact ionization and other SEs (F_{ee}). In the binary collision model, both F_{ei} and F_{ee} are not considered; however, in the free electron gas model, F_{ee} is not incorporated, while an interaction similar to F_{ei} is considered.

3. Debye shield theory

Using one dimensional Poisson's equation, we obtain

$$n_e(r) \sim n_{e0}\, 1/2\pi r \, \exp(-r/\lambda_D), \qquad (1)$$

where n_e, n_{e0}, r, and λ_D are the electron density, constant value, the distance from the ion path, and Debye length, respectively. Using $n_e(r)$, as stated in eq. (1), and ion density, the probability (P_{set}) of the secondary electrons escaping the TP is solved using the following relation:

$$P_{set} \propto \frac{[A + (\sqrt{S} - A)\exp(-\frac{\sqrt{S}r_e}{C})]}{\sqrt{S}}. \qquad (2)$$

Here, r_e is the point at which it is assumed that SEs escape the TP.

4. Results and discussion

Figure 1 depicts $N_{SE}(r)$ vs. r at $E_{ion} \sim 500$ keV/u for $\sigma \sim$ (a) 8 $\times 10^{-16}$ and (b) 2×10^{-15} with $N_{SE}(r) \propto 2\pi r\, n_e(r)$, where E_{ion} denotes the incident-ion energy. In figure 1, functions $N_{SE0} \exp(-r/\lambda_D)$ are also shown, where N_{SE0} and λ_D are approximately estimated from our simulation results. As shown in figure 1, $N_{SE}(r)$ almost coincides with the solution of the Poisson's equation.

Figure 2 depicts P_{set} vs. σ at $r_e \sim 2$ and 5 nm, and $t \sim 2, 3, 4, 5, 10, 40, 80$ fs at $E_{ion} \sim 500$ keV/u. In this figure, the function on the right-hand side of eq. (2) is also plotted. Observe from figure 2 that P_{set} almost coincides with eq. (2). Namely, we succeeded in deriving an analytical solution that approximately reproduces the simulation results of P_{set}. At $r_e < 2$ nm, the term $\exp(-\sqrt{\sigma}r_e/C)$ in Eq.(2) cannot be ignored for all σ in question because r_e and λ_D are comparable. At $r_e \geq 5$ nm, this term becomes almost zero; therefore, $P_{set} \propto 1/\sqrt{\sigma}$.
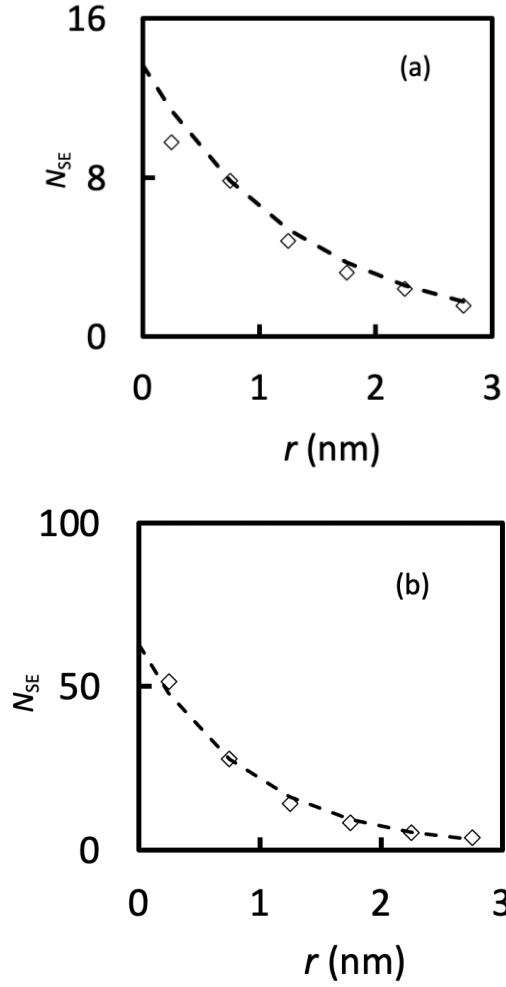
Fig.1 $N_{SE}(r)$ vs. r at $E_{ion} \sim 500$ keV/u for $\sigma =$ (a) 8×10^{-16}, and (b) 2×10^{-15}, and (d) 4×10^{-15} cm². The simulation results are indicated by the symbol $\diamondsuit$, whereas the dashed lines represent the functions $N_{SE0} \exp (-r/\lambda_D)$.

Fig. 2 P_{set} vs. σ for $r_e \sim$ (a) 2 and (b) 5 nm at $E_{ion} \sim 500$ keV/u and $t \sim 2, 3, 4, 5, 10, 40,$ and 80 fs (which are indicated by the symbols $\bigcirc$, $+$, $-$, $\times$, $\diamondsuit$, $\square$, and $\triangle$, respectively). Thick-solid and dashed lines express functions of the right side of eq. (2) and functions showing the trend decreasing $(\sigma)^{-1/2}$, respectively.

5. Summary

In this study, we developed a simulation model that forms the Debye shield. Based on the simulation results of P_{set}, we demonstrated when, where, and how the Debye shield in plasma is created by heavy-ion irradiation. The simulated Debye shield is approximately reproduced by the analytical solution of Poisson's equation. We derived a formula that approximately reproduces the simulation results of P_{set}. This formula is also expressed as a function of only one parameter, namely, σ.

References

1. K. Moribayashi, Jpn. J. Appl. Phys. **59.** SH0801 (2020).
2. K. Moribayashi, Radiat. Phys. Chem. **184** 10.9436(2021).
3. K. Kimura et al, Res. B. **193** 661. Nucl. Insm. Meth.Phys (2002).

Publication Lists

Original Papers

1. Temperature dependence of site-resolved Fe magnetic moments in ThMn$_{12}$-type Sm(Fe$_{1-x}$Co$_x$)$_{12}$ compounds studied via synchrotron Mössbauer spectroscopy.
D. Ogawa, T. Fukazawa, S. Li, T. Ueno, S. Sakai, T. Mitsui, T. Miyake, S. Okamoto, S. Hirosawa, Y. K. Takahashi, Journal of Magnetism and Magnetic Materials, 552, 169188, 2022, DOI:10.1016/j.jmmm.2022.169188

2. Direct observation of magnetic Friedel oscillation at Fe(001) surface.
Takaya Mitsui, Seiji Sakai, Songtian Li, Tetsuro Ueno, Tetsu Watanuki, Yasuhiro Kobayashi, Ryo Masuda, Makoto Seto, Hisazumi Akai, Hyperfine Interactions, 242, 37, 2021, DOI:10.1007/s10751-021-01772-0

3. Element-specific magnetic hysteresis loops observed in hexagonal ErFeO$_3$ thin films.
Hiroko Yokota, Yu Kobori, Shunsuke Jitsukawa, Sakai Seiji, Yukiharu Takeda, Takaya Mitsui, Yasuhiro Kobayashi, Shinji Kitao, Materials Research Express, 8(8), 086402, 2021, DOI:10.1088/2053-1591/ac1aa9

4. Activity enhancement of platinum oxygen-reduction electrocatalysts using ion-beam induced defects.
Kimata Tetsuya, Kakitani Kenta, Yamamoto Shunya, Shimoyama Iwao, Matsumura Daiju, Iwase Akihiro, Mao Wei, Kobayashi Tomohiro, Yamaki Tetsuya, Terai Takayuki, Physical Review Materials, 6, 035801, 2022, DOI:10.1103/PhysRevMaterials.00.005800

5. Mössbauer spectroscopy with polarized synchrotron beams at Fe/Au (111) interface.
Jun Okabayashi, Songtian Li, Seiji Sakai, Yasuhiro Kobayashi, Kosuke Fujiwara, Takaya Mitsui, Seiji Mitani, Hyperfine Interactions, 242, 59, 2021, DOI:10.1007/s10751-021-01788-6

6. Gamma-ray flash in the interaction of a tightly focused single-cycle ultra-intense laser pulse with a solid target.
P. Hadjisolomou, T.M. Jeong, P. Valenta, D. Kolenaty, R. Versaci, V. Olšovcová, C.P. Ridgers, Sergey Bulanov, Journal of Plasma Physics, 88(1), 2022, DOI:10.1017/S0022377821001318

7. On the electromagnetic-electron rings originating from the interaction of high-power short-pulse laser and underdense plasma.
P. Valenta, M. Grittani, C. M. Lazzarini, O. Klimo, S. Bulanov, Physics of Plasmas, 28(12), 2021, DOI:10.1063/5.0065167

8. Ion solvation and association and water structure in an aqueous cerium(III)chloride solution in the gigapascal pressure range.
Toshio Yamaguchi, Nami Fukuyama, Koji Yoshida, Yoshinori Katayama, Analytical Sciences, 38(2), 409 - 417, 2022, DOI:10.2116/analsci.21P297

9. 極端紫外 (EUV) 域低入射角高回折効率ラミナー型回折格子の設計.
小池　雅人, 村野　孝訓, 越谷　翔悟, 羽多野　忠, ピロジコフ　アレキサンダー, 垣尾　翼, 林　信和, 長野　哲也, 近藤　公伯, 寺内　正己, Ｘ線分析の進歩, 53, 70 - 76, 2022

10. Design and experimental evaluation of enhanced diffraction efficiency of lanthanum-based material coated laminar-type gratings in boron K-emission region.
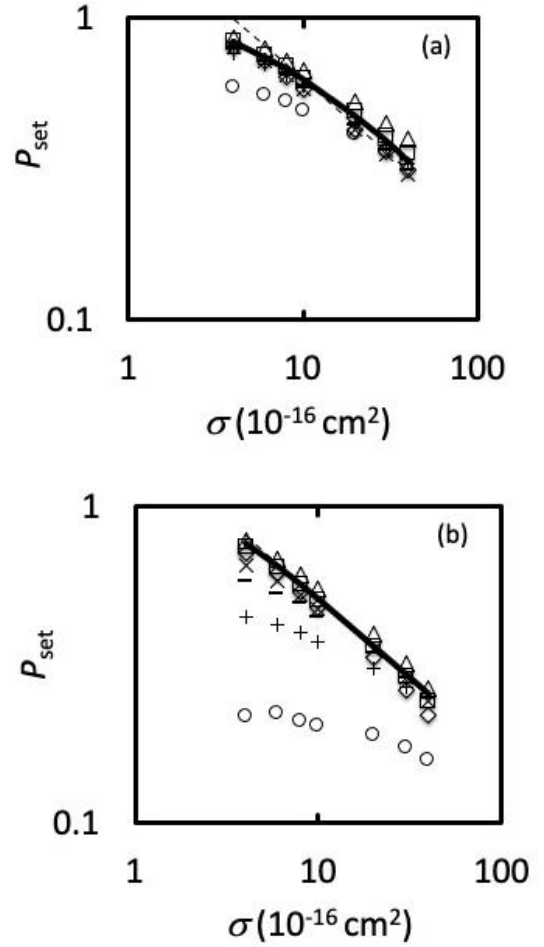Tadashi Hatano, Masato Koike, Masami Terauchi, Alexander S Pirozhkov, Nobukazu Hayashi, Hiroyuki Sasai, Tetsuya Nagano, Applied Optics, 60(16), 4993 - 4999, 2021, DOI:10.1364/AO.430802

11. Enhancement of pre-pulse and picosecond pedestal contrast of the petawatt J-KAREN-P laser.
Kiriyama Hiromitsu, Miyasaka Yasuhiro, Kon Akira, Nishiuchi Mamiko, Sagisaka Akito, Sasao Hajime, Alexander Pirozhkov, Fukuda Yuuji, Ogura Koichi, Kondo Kotaro, Kando Masaki, Dover P. Nicholas, High Power Laser Science and Engineering, 9, e62, 2021, DOI:10.1017/hpl.2021.51

12. In-Target Proton–Boron Nuclear Fusion Using a PW-Class Laser.
Daniele Margarone, Julien Bonvalet , Lorenzo Giuffrida, Alessio Morace, Vasiliki Kantarelou, Marco Tosca, Didier Raffestin, Philippe Nicolai, Antonino Picciotto, Yuki Abe, Yasunobu Arikawa, Shinsuke Fujioka, Fukuda Yuji, Yasuhiro Kuramitsu, Hideaki Habara, Dimitri Batani, Applied Sciences, 12, 1444, 2022, DOI:10.3390/app12031444

13. Broadband normal-incidence mirrors for a range of 111−138 Å based on an a-periodic Mo/Be multilayer structure.

M. M. Barysheva, S. A. Garakhin, A. O. Kolesnikov, A. Pirozhkov, V. N. Polkovnikov, E. N. Ragozin, A. N. Shatokhin, R. M. Smertin, M. V. Svechnikov, E. A. Vishnyakov, Optical Materials Express, 11(9), 3038 - 3048, 2021, DOI:10.1364/OME.434506

14. Deconvolution of multi-Boltzmann x-ray distribution from linear absorption spectrometer via analytical parameter reduction.

C. D. Armstrong, D. Neely, D. Kumar, P. McKenna, R. J. Gray, A. Pirozhkov, Review of Scientific Instruments, 92(11), 113102, 2021, DOI:10.1063/5.0057486

15. Robustness of large-area suspended graphene under interaction with intense laser.

Y. Kuramitsu, T. Minami, T. Hihara, K. Sakai, T. Nishimoto, S. Isayama, Y.T. Liao, K.T. Wu, W.Y. Woon, S.H. Chen, Y.L. Liu, S.M. He, C.Y. Su, M. Ota, S. Egashira, A. Morace, Y. Sakawa, H. Habara, R. Kodama, L. N. K. Dohl, N. Woolsey, M. Koenig, M. Kanasaki, T. Asai, T. Yamauchi, K. Oda, K. Kondo, H. Kiriyama, Y. Fukuda, Scientific Reports, 12, 2346, 2022, DOI:10.1038/s41598-022-06055-4

16. Discriminative detection of laser-accelerated multi-MeV carbon ions utilizing solid state nuclear track detectors.

Hihara Takamasa, Kanasaki Masato, Asai Takafumi, Kusumoto Tamon, Kodaira Satoshi, Kiriyama Hiromitsu, Oda Keiji, Yamauchi Tomoya, Wei-Yen Woon, Kuramitsu Yasuhiro, Fukuda Yuji, Scientific Reports, 11, 16283, 2021, DOI:10.1038/s41598-021-92300-1

17. Energetic α-particle sources produced through proton-boron reactions by high-energy high-intensity laser beam.

J. Bonvalet, Ph. Nicolai, D. Raffestin, E. D'humieres, D. Batani, V. Tikhonchuk, V. Kantarelou, L. Giuffrida, M. Tosca, G. Korn, A. Picciotto, A. Morace, Y. Abe, Y. Arikawa, S. Fujioka, Y. Fukuda, Y. Kuramitsu, H. Habara, D. Margarone, Physical Review E, 103(5), 053202, 2021, DOI:10.1103/PhysRevE.103.053202

18. Highly stable sub-nanosecond Nd:YAG pump laser for optically synchronized optical parametric chirped-pulse amplification.

Yasuhiro Miyasaka, Kotaro Kondo, Maki Kishimoto, Michiaki Mori, Masaki Kando, Hiromitsu Kiriyama, Optics express, 29(20), 32404 - 32411, 2021, DOI:10.1364/OE.430953

19. レーザー加速炭素ビーム粒子数のシングルショット診断.

宮武　立彦, 小島　完興, 榊　泰直, レーザー研究, 50(1), 42 - 46, 2022

20. Superluminal-subluminal orbital angular momentum femtosecond laser focus.

Tae Moon Jeong, Sergey Bulanov, Prokopis Hadjisolomou, Esirkepov Timur, Optics Express, 29(20), 31665 - 31679, 2021, DOI:10.1364/OE.439377

21. Observation of Zeeman splitting effect in a laser-driven coil.

Baojun Zhu, Zhe Zhang, Chang Liu, Dawei Yuan, Weiman Jiang, Huigang Wei, Fang Li, Yihang Zhang, Bo Han, Lei Cheng, Shangqing Li, Jiayong Zhong, Xiaoxia Yuan, Bowei Tong, Wei Sun, Zhiheng Fang, Chen Wang, Zhiyong Xie, Neng Hua, Rong Wu, Zhanfeng Qiao, Guiyun Liang, Baoqiang Zhu, Jianqiang Zhu, Shinsuke Fujioka, Yutong Li, Matter and Radiation at Extremes, 7, 024402, 2022, DOI:10.1063/5.0060954

22. Experimental demonstration of 7-femtosecond electron timing fluctuation in laser wakefield acceleration.

Kai Huang, Zhan Jin, Nakanii Nobuhiko, Tomonao Hosokai, Kando Masaki, Applied Physics Express, 15(3), 036001, 2022, DOI:10.35848/1882-0786/ac5237

23. Generation of High Order Harmonics in Heisenberg-Euler Electrodynamics.

Pavel Sasorov, Francesco Pegoraro, Esirkepov Timur, Sergey Bulanov, New Journal of Physics, 23, 105003, 2021, DOI:10.1088/1367-2630/ac28cb

24. Gamma Factory Searches forNew Extremely Weakly-Interacting Particles.

Sreemanti Chakraborti, Jonathan L. Feng, James Kevin Koga, Mauro Valli, Physical Review D, 104, 055023-1 - 13, 2021, DOI:10.1103/PhysRevD.104.055023

25. Relativistic flying laser focus by a laser-produced parabolic plasma mirror.

Tae Moon Jeong, Sergey Bulanov, Petr Valenta, Georg Korn, Esirkepov Timur, James Kevin Koga, Alexander Pirozhkov, Kando Masaki, Stepan S. Bulanov, Physical Review A, 104(5), 053533, 2021, DOI:10.1103/PhysRevA.104.053533

26. Denoising application for electron spectrometer in laser-driven ion acceleration using a Simulation-supervised Learning based CDAE.

Tatsuhiko Miyatake, Keiichiro Shiokawa, Hironao Sakaki, NicholasPeter Dover, Mamiko Nishiuchi, HazelFrances Lowe, Kotaro Kondo, Akira Kon, Masaki Kando, Kiminori Kondo, Nuclear Instruments and Methods in Physics Research Section A: Accelerators, Spectrometers, Detectors and Associated Equipment, 999, 165227, 2021, DOI:10.1016/j.nima.2021.165227

27. ラスター(格子状)スキャン機能を有するレーザー打音検査装置を用いたトンネル覆工コンクリートの診断支援技術の高度化に関する研究.
戸本　悟史, 長谷川　登, 岡田　大, 近藤　修司, 北村　俊幸, 三上　勝大, 錦野　将元, 中村　光, 構造工学論文集, 68A, 671 - 684, 2022, DOI:10.11532/structcivil.68A.671

28. Nonlinear propagation effect in x-ray parametric amplification during high harmonic generation.
Jozsef Seres, Enikoe Seres, Carles Serrat, Thanhhung Dinh, Hasegawa Noboru, Ishino Masahiko, Nishikino Masaharu, Shinichi Namba, Journal of the Optical Society of America B, 39(4), 1263 - 1271, 2022, DOI:10.1364/JOSAB.454902

29. Defect detection of concrete in infrastructure based on Rayleigh wave propagation generated by laser-induced plasma shock waves.
Wakata Sho, Hosoya Naoki, Hasegawa Noboru, Nishikino Masaharu, International Journal of Mechanical Sciences, 218, 107039, 2022, DOI:10.1016/j.ijmecsci.2021.107039

30. Improvement of ignition and burning target design for fast ignition scheme.
H. Nagatomo, T. Johzaki, M. Hata, Y. Sentoku, S. Fujioka, K. Mima, H. Sakagami, Nuclear Fusion, 61(12), 126032, 2021, DOI:10.1088/1741-4326/ac2d5a

31. Pulse duration constraint of whistler waves in magnetized dense plasma.
Hata Masayasu, Takayoshi Sano, Sentoku Yasuhiko, Hideo Nagatomo, Hitoshi Sakagami, Physical review. E, 104(3), 035205, 2021, DOI:10.1103/PhysRevE.104.035205

32. Independent contribution of optical attenuation length in ultrafast laser-induced structural change.
Shibuya Tatsunori, Sakaue Kazuyuki, Ogawa Hiroshi, Satoh Daisuke, Thanhhung Dinh, Ishino Masahiko, Tanaka Masahito, Washio Masakazu, Higashiguchi Takeshi, Nishikino Masaharu, Kon Akira, Kubota Yuya, Inubushi Yuichi, Owada Shigeki, Kobayashi Yohei, Kuroda Ryunosuke, Optics Express, 29(21), 33121 - 33133, 2021, DOI:10.1364/OE.432130

33. 分子動力学法を用いた DNA テロメア構造中バックボーン水素の溶媒接触表面積の評価.
土田 陽平, 齋藤 誠紀, 中村 浩章, 米谷 佳晃, 藤原 進, 日本シミュレーション学会論文誌, 13(1), 32 - 36, 2021, DOI:10.11308/tjsst.13.32

34. Demonstration of High-Speed Laser Hammering System for the Lining Concrete Inspection.
N. Hasegawa, M. Nishikino, H. Okada, S. Kondo, T. Kitamura, M. Abe, K. Masuzoe, S. Kogure, ITA-AITES World Tunnel Congress, WTC2020 and 46th General Assembly Kuala Lumpur, Malaysia 11-17 September 2020, 46, 653 - 656, 2020

35. Dependence of dose rate on the sensitivity of the resist under ultra-high flux extreme ultraviolet (EUV) pulse irradiation.
Okamoto Kazumasa, Kawai Shunpei, Ikari Yuta, Hori Shigeo, Konda Akihiro, Ueno Koki, Arai Yohei, Ishino Masahiko, Thanhhung Dinh, Nishikino Masaharu, Kon Akira, Owada Shigeki, Inubushi Yuichi, Kinoshita Hiroo, Kozawa Takahiro, Applied Physics Express, 14, 066502, 2021, DOI:10.35848/1882-0786/abfca3

36. Liquid structure of tantalum under internal negative pressure.
Kento Katagiri, Norimasa Ozaki, Satoshi Omura, Bruno Albertazzi, Yoichiro Hironaka, Yuichi Inubushi, K. Ishida, Michel Koenig, Kohei Miyanishi, Hirotaka Nakamura, Nishikino Masaharu, Takuo Okuchi, Tomoko Sato, Yusuke Seto, Keisuke Shigemori, Keiichi Soeda, Yoshinori Tange, Tadashi Togashi, Yuhei Umeda, Makina Yahashi, Toshinori Yabuchi, Ryosuke Kodama, Physical Review Letters, 126, 175503, 2021, DOI:10.1103/PhysRevLett.126.175503

37. Three-temperature modeling of laser-induced damage process in silicon.
Prachi Venkat, Tomohito Otobe, Applied Physics Express, 15, 041008-1-5, 2022, DOI:10.35848/1882-0786/ac5edb

38. Electron excitation rate in dielectrics under an intense elliptically polarized laser field.

Prachi Venkat, Tomohito Otobe, Journal of the Physical Society of Japan, 91(4), 044401, 2022, DOI:10.7566/JPSJ.91.044401

39. Non-linear dynamics of electromagnetic field and valley polarization in WSe$_2$ monolayer.
Arqum Hashmi, Shunsuke Yamada, Atsushi Yamada, Kazuhiro Yabana, Tomohito Otobe, Applied Physics Letters, 120(5), 051108, 2022, DOI:10.1063/5.0077235

40. Valley polarization control in WSe$_2$ monolayer by a single-cycle laser pulse.
Arqum Hashmi, Shunsuke Yamada, Atsushi Yamada, Kazuhiro Yabana, Tomohito Otobe, Physical Review B, 105(11), 115403, 2022, DOI:10.1103/PhysRevB.105.115403

41. Electronic Relaxation and Dissociation Dynamics in Formaldehyde: Pump Wavelength Dependence.
Tomoyuki Endo, Simon P. Neville, Philippe Lassonde, Chen Qu, Hikaru Fujise, Mizuho Fushitani, Akiyoshi Hishikawa, Paul L. Houston, Joel M. Bowman, François Légaré, Michael S. Schuurman, Heide Ibrahim, Physical Chemistry Chemical Physics, 24(3), 1779 - 1786, 2022, DOI:10.1039/D1CP04264E

42. Broadband operation of a synchronously pumped optical parametric oscillator with a spatially dispersed beam.
Nagashima Keisuke, Itakura Ryuji, Ishii Nobuhisa, Optics Letters, 46(17), 4414 - 4417, 2021, DOI:10.1364/OL.435039

43. Attosecond electronic dynamics of core-excited states of N2O in the soft X-ray region.
Saito Nariyuki, Douguet Nicolas, Sannohe Hiroki, Ishii Nobuhisa, Kanai Teruto, Wu Yi, Chew Andrew, Han Seunghwoi, Schneider Barry, Olsen Jeppe, Argenti Luca, Chang Zenghu, Jiro Itatani, Physical Review Research, 3, 043222, 2021, DOI:10.1103/PhysRevResearch.3.043222

44. Generation of wavelength-tunable few-cycle pulses in the mid-infrared at repetition rates up to 10 kHz.
Sanari Yasuyuki, Sekiguchi Fumiya, Nakagawa Kotaro, Ishii Nobuhisa, Kanemitsu Yoshihiko, Hirori Hideki, Optics Letters, 46(20), 5280 - 5283, 2021, DOI:10.1364/OL.440228

45. Terahertz irradiation effects on the morphology and dynamics of actin biopolymer.
Hiromichi Hoshina, Shota Yamazaki, Masaaki Tsubouchi, Masahiko Harata, Journal of Physics: Photonics, 3(3), 034015-1 - 13, 2021, DOI:10.1088/2515-7647/ac0958

46. Semi-classical description of electron dynamics in extended systems under intense laser fields.
Mizuki Tani, Tomohito Otobe, Yasushi Shinohara, Kenichi L. Ishikawa, Physical Review B, 104, 075157, 2021, DOI:10.1103/PhysRevB.104.075157

47. Generation and compression of an intense infrared white light continuum in YAG irradiated by picosecond pulses.
Ishii Nobuhisa, Maruyama Momoko, Nagashima Keisuke, Ochi Yoshihiro, Itakura Ryuji, Optics express, 29(11), 17069 - 17076, 2021, DOI:10.1364/OE.423671

48. Post-Ionization Dynamics of the Polar Molecule OCS in Asymmetric Laser Fields.
Tomoyuki Endo, Karl-Michael Ziems, Martin Richter, Friedrich G. Froebel, Akiyoshi Hishikawa, Stefanie Gräfe, François Légaré, Heide Ibrahim, Frontiers in Chemistry, 10, 859750, 2022, DOI:10.3389/fchem.2022.859750

49. Bulk-sensitive magnetic microscope utilizing x-ray magnetic circularly polarized emission.
Kento Sugawara, Toshiya Inami, Takahiro Nakada, Yui Sakaguchi, Shin Takahashi, Journal of Applied Physics, 130(11), 113901, 2021, DOI:10.1063/5.0058201

50. Morphotropic phase boundaries of $(1-x)Pb(Zn_{1/3}Nb_{2/3})O_3-xPbTiO_3$ probed by Raman spectroscopy at high temperature.
Akari Kanagawa, Yasuhiro Fujii, Kenji Ohwada, Yukikuni Akishige, Shinya Tsukada, Japanese Journal of Applied Physics, 60(SF), SFFA04, 2021, DOI:10.35848/1347-4065/ac0c6d

51. Observation of 90° domain walls in relaxor ferroelectrics PMN-28.6%PT by focusing upon the CTR scattering.

Kenji Ohwada, Kazumichi Namikawa, Japanese Journal of Applied Physics, 60(SF), SFFA05, 2021, DOI:10.35848/1347-4065/ac0df7

52. The Origin of Highly Crystallized Face-Centered Cubic YH$_3$ High-Pressure Phase when quenched to ambient condition.
Riki Kataoka, Noboru Taguchi, Mitsunori Kitta, Nobuhiko Takeichi, Reina Utsumi, Hiroyuki Saitoh, Masashi Nozaki, Atsunori Kamegawa, Materials Today Communications, 31, 103265, 2022, DOI:10.1016/j.mtcomm.2022.103265

53. Comparative study of stress and strain partitioning behaviors in medium manganese and transformation-induced plasticity-aided bainitic ferrite steels.
Tomohiko Hojo, Motomichi Koyama, Bakuya Kumai, Yuki Shibayama, Ayumi Shiro, Takahisa Shobu, Hiroyuk iSaitoh, Saya Ajito, Eiji Akiyama, Scripta Materialia, 210(15), 114463, 2022, DOI:10.1016/j.scriptamat.2021.114463

54. In situ synchrotron radiation observation of deformation and annealing processes of aluminum single crystal.
Ayumi Shiro, Tatsuya Okada, Shobu Takahisa, Mechanical Engineering Journal, 8(6), 21-00106, 2021, DOI:10.1299/mej.21-00106

55. Bayesian sparse modeling of extended X-ray absorption fine structure to determine interstitial oxygen positions in yttrium oxyhydride epitaxial thin film.
Hiroyuki Kumazoe, Yasuhiko Igarashi, Fabio Iesari, Ryota Shimizu, Yuya Komatsu, Taro Hitosugi, Daiju Matsumura, Hiroyuki Saitoh, Kazunori Iwamitsu, Toshihiro Okajima, Yoshiki Seno, Masato Okada, Ichiro Akai, AIP Advances, 11(12), 125013, 2021, DOI:10.1063/5.0071166

56. In situ synchrotron radiation X-ray diffraction measurements of Fe–Mo alloy hydrides formed under high pressure and high temperature.
Reina Utsumi, Masahiro Morimoto, Hiroyuki Saitoh, Tetsu Watanuki, Toyoto Sato, Shigeyuki Takagi, Journal of Alloys and Compounds, 893, 162300, 2021, DOI:10.1016/j.jallcom.2021.162300

57. Hydrogenation treatment under several gigapascals assists diffusionless transformation in a face-centered cubic steel.
Motomichi Koyama, Hiroyuki Saitoh, Toyoto Sato, Shin-ichi Orimo, Eiji Akiyama, Scientific Report, 11, 119384, 2021, DOI:10.1038/s41598-021-98938-1

58. Nano-structural perspective for destabilization of Mg hydride using immiscible transition metal of Mn.
Yanshan Lu, Kohta Asano, Herman Schreuders, Hyunjeong Kim, Kouji Sakaki, Akihiko Machida, Tetsu Watanuki, Bernard Dam, Inorganic Chemistry, 60(19), 15024 - 15030, 2021, DOI:10.1021/acs.inorgchem.1c02525

59. Density and elastic properties of liquid gallium up to 10 GPa using X-ray absorption method combined with externally heated diamond anvil cell.
Ryo Tsuruoka, Hidenori Terasaki, Seiji Kamada, Fumiya Maeda, Tadashi Kondo, Naohisa Hirao, Saori I. Kawaguchi, Iori Yamada, Satoru Urakawa, Akihiko Machida, High Pressure Research, 41(4), 379 - 391, 2021, DOI:10.1080/08957959.2021.1998478

60. Revised α/ε′–γ phases boundaries for the Fe–H system.
Sho Kakizawa, Chikara Shito, Yuichiro Mori, Hiroyuki Saitoh, Katsutoshi Aoki, Solid State Communications, 340, 114542, 2021, DOI:10.1016/j.ssc.2021.114542

61. Generating Mechanism of Catalytic Effect for Hydrogen Absorption/Desorption Reactions in NaAlH$_4$-TiCl$_3$.
Kazutaka Ikeda, Fumika Fujisaki, Toshiya Otomo, Hidetoshi Ohshita, Takashi Honda, Toru Kawamata, Hiroshi Arima, Kazumasa Sugiyama, Hitoshi Abe, Hyunjeong Kim, Kouji Sakaki, Yumiko Nakamura, Akihiko Machida, Toyoto Sato, Shigeyuki Takagi, Shin-ichi Orimo, Applied Sciences, 11(18), 8349, 2021, DOI:10.3390/app11188349

62. Origin and absence of giant negative thermal expansion in reduced and oxidized Ca$_2$RuO$_4$.
Lei Hu, Yingcai Zhu, Yue-wen Fang, Masayuki Fukuda, Takumi Nishikubo, Zhao Pan, Yuki Sakai, Shogo Kawaguchi, Hena Das, Akihiko Machida, Tetsu Watanuki, Shigeo Mori, Koshi Takenaka, Masaki Azuma, Chemistry of Materials, 33(19), 7665 - 7674, 2021, DOI:10.1021/acs.chemmater.1c01619

63. Sodium insertion and de-insertion mechanism of spinel-type sodium titanium oxide studied by in situ XRD.
Riki Kataoka, Toshikatsu Kojima, Akihiko Machida, Mitsunori Kitta, Journal of Alloys and Compounds, 890(15), 161763, 2021, DOI:10.1016/j.jallcom.2021.161763

64. Pressure–Temperature Phase Diagram of Ta-H System up to 9 GPa and 600 °C.
Hiroyuki Saitoh, Shigeyuki Takagi, Toyoto Sato, Shin-ichi Orimo, Applied Sciences, 11(15), 6719, 2021, DOI:10.3390/app11156719

65. Hydrogen storage by earth-abundant metals, synthesis and characterization of $Al_3FeH_{3.9}$.
Hiroyuki Saitoh, Toyoto Sato, Mai Tanikami, Kazutaka Ikeda, Akihiko Machida, Tetsu Watanuki, Tomitsugu Taguchi, Shunya Yamamoto, Tetsuya Yamaki, Shigeyuki Takagi, Toshiya Otomo, Shin-ichi Orimo, Materials & Design, 208, 109953, 2021, DOI:10.1016/j.matdes.2021.109953

66. Iodine containing porous organosilica nanoparticles trigger tumor spheroids destruction upon monochromatic X-ray irradiation: DNA breaks and K-edge energy X-ray.
Yuya Higashi, Kotaro Matsumoto, Hiroyuki Saitoh, Ayumi Shiro, Yue Ma, Mathilde Laird, Shanmugavel Chinnathambi, Albane Birault, Tan Le Hoang Doan, Ryo Yasuda, Toshiki Tajima, Tetsuya Kawachi, Fuyuhiko Tamanoi, Scientific Reports, 11, 14192, 2021, DOI:10.1038/s41598-021-93429-9

67. Internal Strain Distribution of Laser Lap Joints in Steel under Loading Studied by High-Energy Synchrotron Radiation X-rays.
Takahisa Shobu, Ayumi Shiro, Fumiaki Kono, Toshiharu Muramatsu, Tomonori Yamada, Masayuki Naganuma, Takayuki Ozawa 8, Quantum Beam Science, 5(2), 17, 2021, DOI:10.3390/qubs5020017

68. 張出し成形した焼戻しマルテンサイト鋼板の水素脆化に及ぼす残留応力の影響.
西村 隼杜, 北條 智彦, 味戸 沙耶, 柴山 由樹, 小山 元道, 齋藤 寛之, 城 鮎美, 安田 良, 菖蒲 敬久, 秋山 英二, 鉄と鋼, 107(9), 760 - 768, 2021, DOI:10.2355/tetsutohagane.TETSU-2021-055

69. Bragg coherent diffraction imaging allowing simultaneous retrieval of three-dimensional shape and strain distribution for 40–500 nm particles.
Norihiro Oshime, Kenji Ohwada, Kento Sugawara, Tomohiro Abe, Reiji Yamauchi, Tetsuro Ueno, Akihiko Machida, Tetsu Watanuki, Shintaro Ueno, Ichiro Fujii, Satoshi Wada, Ryota Sato, Toshiharu Teranishi, Miho Yamauchi, Kenji Ishii, Hidenori Toyokawa, Koichi Momma, Yoshihiro Kuroiwa, Japanese Journal of Applied Physics, 60(SF), SFFA07, 2021, DOI:10.35848/1347-4065/ac148b

70. Temperature Effects on Local Structure, Phase Transformation, and Mechanical Properties of Calcium Silicate Hydrates.
Sumin Im, Hyeonseok Jee, Heongwon Suh, Manabu Kanematsu, Satoshi Morooka, Taku Koyama, Yuhei Nishio, Akihiko Machida, Jihoon Kim, Sungchul Bae, Journal of the American Ceramic Society, 104(9), 4803 - 4818, 2021, DOI:10.1111/jace.17881

71. Depressurization-induced diffusionless transformation in pure iron hydrogenated under several gigapascals.
Motomichi Koyama, Hiroyuki Saitoh, Toyoto Sato, Shin-ichi Orimo, Eiji Akiyama, Materials Letters: X, 11, 100078, 2021, DOI:10.1016/j.mlblux.2021.100078

72. ヒドラジン酸化触媒の In-situ XAFS 測定.
吉元 光児, 西野 英里子, 坂本 友和, 加藤 豪士, 草野 翔吾, 水木 純一郎, 松村 大樹, 石井 賢司, SPring-8/SACLA 利用研究成果集, 9(6), 414 - 416, 2021, DOI:10.18957/rr.9.6.414

73. Dynamical effects on thermal diffuse scattering in Si 111 Bragg reflection.
Takaya Mitsui, Kosuke Fujiwara, Yasuhiko Imai, Yoshitaka Yoda, Journal of the Physical Society of Japan, 91, 035002, 2022, DOI:10.7566/JPSJ.91.035002

74. Distinct variation of electronic states due to annealing in T'-type $La_{1.8}Eu_{0.2}CuO_4$ and Nd_2CuO_4.
Shun Asano, Kenji Ishii, Daiju Matsumura, Takuya Tsuji, Kota Kudo, Takanori Taniguchi, Shin Saito, Toshiki Sunohara, Takayuki Kawamata, Yoji Koike, Masaki Fujita, Physical Review B, 104(21), 214504, 2021, DOI:10.1103/PhysRevB.104.214504

75. Unsupervised clustering for identifying spatial inhomogeneity on local electronic structures.

Hideaki Iwasawa, Tetsuro Ueno, Takahiko Masui, Setsuko Tajima, npj Quantum Materials, 7, 24, 2022, DOI:10.1038/s41535-021-00407-5

76. Structure and reaction mechanism of binary Ni–Al oxides as materials for lithium-ion battery anodes.

Noriyuki Sonoyama, Kaori Niki, Akihiro Koide, Mina Eguchi, Yoshitaka Ogasawara, Tetsuya Tsukada, Patrick K. Dedetemo, Dalton Transactions, 50(40), 14176 - 14186, 2021, DOI:10.1039/D1DT01911B

77. Competition between helimagnetic and ferroquadrupolar orderings in a monoaxial chiral magnet $DyNi_3Ga_9$ studied by resonant x-ray diffraction.

Mitsuru Tsukagoshi, Takeshi Matsumura, Shinji Michimura, Toshiya Inami, Shigeo Ohara, Physical Review B, 105(1), 014428, 2021, DOI:10.1103/PhysRevB.105.014428

78. Sum rules of L-edge x-ray magnetic circularly polarized emission for 3d transition metals.

Akihiro Koide, Takuji Nomura, Toshiya Inami, Physical Review B, 104(9), 094419, 2021, DOI:10.1103/PhysRevB.104.094419

79. ^{161}Dy Synchrotron-Radiation-Based Mössbauer Absorption Spectroscopy.

Ryo Masuda, Shinji Kitao, Hiroyuki Tajima, Hiroki Taniguchi, Takaya Mitsui, Kosuke Fujiwara, Yoshitaka Yoda, Daisuke Ishikawa, Alfred. Q. R. Baron, Takefumi Yoshida, Tetsu Sato, Hisao Kobayashi, Makoto Seto, Hyperfine Interactions, 243, 17, 2022, DOI:10.1007/s10751-022-01802-5

80. Pure Nuclear Bragg Reflection due to Combined Magnetic and Quadrupole Interaction in Fe_3O_4.

Shin Nakamura, Takaya Mitsui, Masayuki Kurokuzu, Susumu Shimomura, Journal of the Physical Society of Japan, 90, 104713, 2021, DOI:10.7566/JPSJ.90.104713

81. Automated stopping criterion for spectral measurements with active learning.

Tetsuro Ueno, Hideaki Ishibashi, Hideitsu Hino, Kanta Ono, npj Computational Materials, 7, 139, 2021, DOI:10.1038/s41524-021-00606-5

82. Electronic and crystal structures of $LnFeAsO_{1-x}H_x$ (Ln = La, Sm) studied by x-ray absorption spectroscopy, x-ray emission spectroscopy, and x- ray diffraction: II pressure dependence.

Yoshiya Yamamoto, Hitoshi Yamaoka, Masahiro Yoshida, Jun-ichi Yamaura, Kenji Ishii, Seiichiro Onari, Takayuki Uozumi, Atsushi Hariki, Takuma Kawai, Munetaka Taguchi, Kensuke Kobayashi, Jung-Fu Lin, Nozomu Hiraoka, Hirofumi Ishii, Ku-Ding Tsuei, Hiroshi Okanishi, Soshi Iimura, Satoru Matsuishi, Hideo Hosono, Jun'ichiro Mizuki, Journal of Physics: Condensed Matter, 33(25), 255603, 2021, DOI:10.1088/1361-648X/abfaf4

83. Valence Control of Charge and Orbital Frustrated System $YbFe_2O_4$ with Electrochemical Li^+ intercalation.

Satoshi Murase, Yumi Yoshikawa, Kosuke Fujiwara, Yukimasa Fukada, Takeshi Teranishi, Jun Kano, Tatsuo Fujii, Yasuhiro Inada, Misaki Katayama, Kenji Yoshii, Takuya Tsujii, Daiju Matsumura, Naoshi Ikeda, Journal of Physics and Chemistry of Solids, 162, 110468, 2022, DOI:10.1016/j.jpcs.2021.110468

84. Synchrotron Mössbauer spectroscopic and x-ray diffraction study of ferropericlase in the high-pressure range of the lower mantle region.

Maki Hamada, Seiji Kamada, Eiji Ohtani, Tatsuya Sakamaki, Takaya Mitsui, Ryo Masuda, Naohisa Hirao, Yasuo Ohishi, Masahide Akasaka, Physical Review B, 103(17), 174108, 2021, DOI:10.1103/PhysRevB.103.174108

85. Quantum Interference of Totally Reflected Mössbauer γ-Rays From a ^{57}Fe Monolayer Embedded in a Thin Film.

Kosuke Fujiwara, Takaya Mitsui, Yumito Aoyagi, Yoshitaka Yoda, Naoshi Ikeda, Journal of the Physical Society of Japan, 90(8), 084705, 2021, DOI:10.7566/JPSJ.90.084705

86. Electronic and crystal structures of $LnFeAsO_{1-x}H_x$ (Ln = La, Sm) studied by x-ray absorption spectroscopy, x-ray emission spectroscopy, and x- ray diffraction (part I: carrier-doping dependence).

Yoshiya Yamamoto, Hitoshi Yamaoka, Takayuki Uozumi, Atsushi Hariki, Seiichiro Onari, Jun-ichi Yamaura, Kenji Ishii, Takuma Kawai, Masahiro Yoshida, Munetaka Taguchi, Kensuke Kobayashi, Jung-Fu Lin, Nozomu Hiraoka, Hirofumi Ishii, Ku-DIng Tsuei, Hiroshi

Okanishi, Soshi Iimura, Satoru Matsuishi, Hideo Hosono, Jun'ichiro Mizuki, Journal of Physics: Condensed Matter, 33(25), 255602, 2021, DOI:10.1088/1361-648X/abf9b9

87. Magnetization process of the S= 1/2 Heisenberg antiferromagnet on the floret pentagonal lattice.

Rito Furuchi, Hiroki Nakano, Norikazu Todoroki, Toru Sakai, Journal of Physics Communications, 5(12), 125008, 2022, DOI:10.1088/2399-6528/ac3f7a

88. Simulating Raman spectra of hydrogen hydrates using first-principles path-integral ring-polymer molecular dynamics.

Takashi Ikeda, Chemical Physics Letters, 792, 139416, 2022, DOI:10.1016/j.cplett.2022.139416

89. Antiphase oscillations in the time-resolved spin structure factor of a photoexcited Mott Insulator on a square lattice.

Takami Tohyama, Kazuya Shinjo, Kenji Tsutsui, Journal of Physics: Conference Series, 2164, 012049, 2022, DOI:10.1088/1742-6596/2164/1/012049

90. Numerical simulations of spectroscopic properties in two-dimensional Mott insulator.

Takami Tohyama, Kazuya Shinjo, Shigetoshi Sota, Kenji Tsutsui, Journal of Physics: Conference Series, 2207, 012028, 2022, DOI:10.1088/1742-6596/2207/1/012028

91. Effect on Compton Scattering Spectra by Hermite–Gaussian Light.

Akane Agui, Hiroshi Sakurai, Naruki Tsuji, Haruka Ito, Kiyofumi Nitta, crystals, 11(6), 650, 2021, DOI:10.3390/cryst11060650

92. MRS-measured glutamate versus GABA reflects excitatory versus inhibitory neural activities in awake mice.

Takado Yuhei, Takuwa Hiroyuki, Kazuaki Sampei, Urushihata Takuya, Manami Takahashi, Shimojo Masafumi, Uchida Shoko, Nitta Nobuhiro, Shibata Sayaka, Nagashima Keisuke, Ochi Yoshihiro, Ono Maiko, Maeda Jun, Tomita Yutaka, Sahara Naruhiko, Jamie Near, Aoki Ichio, Shibata Kazuhisa, Higuchi Makoto, Journal of Cerebral Blood Flow & Metabolism, 42(1), 197 - 212, 2022, DOI:10.1177/0271678X211045449

93. プルトニウムの体外排出に向けたキレート剤による除染に関する基礎検討: X 線吸収分光法によるプルトニウム模擬元素とキレート剤との結合性評価.

上原 章寛, 鮮 樹輝, 佐藤 遼太朗, 松村 大樹, 辻 卓也, 薬丸 晴子, 城 鮎美, 齋藤 寛之, 田中 泉, 石原 弘, 武田 志乃, X 線分析の進歩, 53, 223 - 229, 2022

94. Overall structure of fully assembled cyanobacterial KaiABC circadian clock complex by an integrated experimental-computational approach.

Yasuhiro Yunoki, Atsushi Matsumoto, Ken Morishima, Anne Martel, Lionel Porcar, Nobuhiro Sato, Rina Yogo, Taiki Tominaga, Rintaro Inoue, Maho Yagi-Utsumi, Aya Okuda, Masahiro Shimizu, Reiko Urade, Kazuki Terauchi, Hidetoshi Kono, Hirokazu Yagi, Koichi Kato, Masaaki Sugiyama, Communications Biology, 5, 184, 2022, DOI:10.1038/s42003-022-03143-z

95. HNF1A POU Domain Mutations Found in Japanese Liver Cancer Patients Cause Downregulation of HNF4A Promoter Activity with Possible Disruption in Transcription Networks.

Haque Effi, Teeli Aamir Salam, Winiarczyk Dawid, Taguchi Masahiko, Sakuraba Shun, Kono Hidetoshi, Leszczyński Paweł, Mariusz Pierzchała, Taniguchi Hiroaki, Genes, 13(3), 413, 2022, DOI:10.3390/genes13030413

96. Hybrid QM/MM Free-Energy Evaluation of Drug-Resistant Mutational Effect on the Binding of an Inhibitor Indinavir to HIV-1 Protease.

Taguchi Masahiko, Oyama Ryo, Kaneso Masahiro, Hayashi Shigehiko, Journal of Chemical Information and Modeling, 62, 1328-1344, 2022, DOI:https://doi.org/10.1021/acs.jcim.1c01193

97. Interplay among transacting factors around promoter in the initial phases of transcription.

Amarjeet Kumar, Wai Soon Chan, Taguchi Masahiko, Kono Hidetoshi, Current Opinion in Structural Biology, 71, 7 - 15, 2021, DOI:10.1016/j.sbi.2021.04.008

98. Extended ensemble simulations of a SARS-CoV-2 nsp1–5′-UTR complex.

Shun Sakuraba, Qilin Xie, Kota Kasahara, Junichi Iwakiri, Hidetoshi Kono, PLoS Computational Biology, 18(1), e1009804, 2022, DOI:10.1371/journal.pcbi.1009804

99. Structural basis of the regulation of the normal and oncogenic methylation of nucleosomal histone H3 Lys36 by NSD2.

Ko Sato, Amarjeet Kumar, Keisuke Hamada, Chikako Okada, Asako Oguni, Ayumu Machida, Shun Sakuraba, Tomohiro Nishizawa, Osamu Nureki, Hidetoshi Kono, Kazuhiro Ogata, Toru Sengoku, nature communications, 12(1), 6605, 2021, DOI:10.1038/s41467-021-26913-5

100. The N-terminal Tails of Histones H2A and H2B Adopt Two Distinct Conformations in the Nucleosome with Contact and Reduced Contact to DNA.

Hideaki Ohtomo, Jun-ichi Kurita, Shun Sakuraba, Zhenhai Li, Yasuhiro Arimura, Masatoshi Wakamori, Yasuo Tsunaka, Takashi Umehara, Hitoshi Kurumizaka, Hidetoshi Kono, Yoshifumi Nishimura, Journal of Molecular Biology, 433(15), 167110, 2021, DOI:10.1016/j.jmb.2021.167110

101. Proton-Cluster-Beam Lethality and Mutagenicity in Bacillus subtilis Spores.

Hase Yoshihiro, Sato Katsuya, Chiba Atsuya, Hirano Yoshimi, Moribayashi Kengo, Narumi Kazumasa, Quantum Beam Science, 5(3), 25, 2021, DOI:10.3390/qubs5030025

102. Formation of clustered DNA damage in vivo upon irradiation with ionizing radiation: Visualization and analysis with atomic force microscopy.

Nakano Toshiaki, Akamatsu Ken, Masataka Tsuda, Ayane Tujimoto, Hirayama Ryoichi, Hiromoto Takeshi, Tamada Taro, Hiroshi Ide, Shikazono Naoya, Proceedings of the National Academy of Sciences of the United States of America, 119, e2119132119, 2022, DOI:10.1073/pnas.2119132119

103. Debye shield formed by track potential and transport of secondary electrons in heavy ion irradiation.

Moribayashi Kengo, Radiation Physics and Chemistry, 184, 109436, 2021, DOI:10.1016/j.radphyschem.2021.109436

104. Study on irradiation effects by femtosecond-pulsed extreme ultraviolet in resist materials.

Hosaka Yuji, Yamamoto Hiroki, Ishino Masahiko, Thanhhung Dinh, Nishikino Masaharu, Kon Akira, Owada Shigeki, Inubushi Yuichi, Kubota Yuya, Maekawa Yasunari, Journal of Photopolymer Science and Technology 34, 95–98, 2021, DOI: 10.2494/photopolymer.34.95

105. Absolute response of a Fuji BAS-TR imaging plate to low-energy protons (<0.2 MeV) and carbon ions (<1 MeV).

Sadaoki Kojima, Tatsuhiko Miyatake, Shunsuke Inoue, Thanh Hung Dinh, Noboru Hasegawa, Michiaki Mori, Hironao Sakaki, Mamiko Nishiuchi, Nicholas P. Dover, Yoichi Yamamoto, Teru Sasaki, Fuyumi Ito, Kotaro Kondo, Takashi Yamanaka, Masaki Hashida, Shuji Sakabe, Masaharu Nishikino, and Kiminori Kondo Review of Scientific Instruments 92, 033306 (2021) DOI:10.1063/5.0035618

106. Modeling the wavelength of unresolved transition arrays in the extreme ultraviolet region from Sn to Hf ions by combining theoretical and experimental spectral data.

Akira Sasaki, Keisuke Fujii, Izumi Murakami, Hiroyuki A. Sakaue, Takeshi Nishikawa, Hayato Ohashi, Nobuyuki Nakamura, AIP Advances 12, 025309 (2022) DOI: 10.1063/5.0077130

107. Hydrophobic Effect on Alkaline Stability of Graft Chains in Ammonium-type Anion Exchange Membranes Prepared by Radiation-Induced Graft Polymerization.

Takashi Hamada, Yue Zhao, Kimio Yoshimura, Aurel Radulescu, Kenji Ohwada, Yasunari Maekawa, R ChemistrySelect, 6(33), 8879-8888, 2021, DOI:10.1002/slct.202102045

108. NRF2 DLG Domain Mutations Identified in Japanese Liver Cancer Patients Affect the Transcriptional Activity in HCC Cell Lines.

Haque E., Śmiech M., Łuczyńska K., Bouchard M. F., Viger R., Kono H., Pierzchała M., Taniguchi H., International Journal of Molecular Sciences, 22 (10), 5296, 2021, DOI:10.3390/ijms22105296

Proceedings

1. **差周波発生のための高非線形性フォトニック結晶ファイバーによる波長シフト.**
   川瀬 啓悟, 羽島 良一, 森 道昭, 永井 良治, 第 18 回日本加速器学会年会プロシーディングス, 2021
2. **Fine structures of Fe L-emission examined by a new HR-SXES instrument.**
   Masami Terauchi, Ryogo Ebisu, Yohei Sato, Koike Masato, Microscopy & Microanalysis, 27(S1), 1370 - 1371, 2021, DOI:10.1017/S1431927621005109
3. **軟 X 線レーザ表面加工.**
   石野 雅彦, 第 95 回レーザ加工学会講演論文集, , 57 - 61, 2021
4. **Short pulse soft x-ray laser ablation research.**
   Ishino Masahiko, Thanhhung Dinh, Mikami Katsuhiro, Hasegawa Noboru, Nishikino Masaharu, Proceedings of SPIE, 11886, 118860R-1 - 5, 2021, DOI:10.1117/12.2591909
5. **Ultra-strong attosecond laser focus produced by a relativistic-flying parabolic mirror.**
   Tae Moon Jeong, Sergey Bulanov, Petr Valenta, Georg Korn, Esirkepov Timur, James Kevin Koga, Alexander Pirozhkov, Proceedings of the 17th International Conference on X-Ray Lasers 2020, 11866, 118860H-1 - 8, 2021, DOI:10.1117/12.2592047
6. **X-ray absorption spectroscopy on uranium ligand exchange in serum between biologicalligands and chelating agents.**
   Uehara Akihiro, Matsumura Daiju, Tsuji Takuya, Yakumaru Haruko, Tanaka Izumi, Shiro Ayumi, Saito Hiroyuki, Ishihara Hiroshi, Takeda Shino, The Journal of Toxicological Sciences, 46, S91, 2021
7. **X 線吸収分光法を用いた血清内の生体内配位子及び除染剤キレートによるウランの配位状態解析.**
   上原 章寛, 松村 大樹, 薬丸 晴子, 城 鮎美, 田中 泉, 辻 卓也, 齋藤 寛之, 石原 弘, 武田 志乃, Fundamental Toxicological Sciences, 8, 119, 2021
8. **Effect of Coulomb interaction between secondary electrons on plasma formation due to heavy-ion irradiation.**
   Moribayashi Kengo, Journal of Physics : Conference series, 2207(1), 012020, 2022, DOI:10.1088/1742-6596/2207/1/012020

表彰

1. **OSA Senior Membership.**
   小池 雅人
   The Optical Society, 2021-07-21
2. **Outstanding Presentation Award.**
   浅井 孝文 "The New Measurement Method for Laser-accelerated Sub-GeV-class Protons using Multiple Coulomb Scattering in an Emulsion Cloud Chamber"
   International Conference on Materials and Systems for Sustainability 2021 (ICMaSS2021), 2021-11-06
3. **日本物理学会若手奨励賞.**
   黄 開 「電気光学効果による先進的なビーム計測とレーザープラズマ加速への応用」
   日本物理学会, 2022-03-16
4. **若手発表賞.**
   小島 完興 「次世代重粒子線がん治療装置のための高純度炭素イオンのレーザー駆動加速」
   ビーム物理研究会, 2021-12-03
5. **分子科学会優秀講演賞.**
   遠藤 友随 「H2CO 分子の超高速緩和およびローミング過程の実時間観測」
   分子科学会, 2021-10-25
6. **第 38 回強誘電体会議 優秀発表賞.**
   押目 典宏 「コヒーレント X 線回折を利用したナノ結晶の 3 次元イメージング」及び論文 "Bragg coherent diffraction imaging allowing simultaneous retrieval of three-dimensional shape and strain distribution for 40–500 nm particles"
   強誘電体会議, 2022-06-01（2021 年度論文に対する表彰）

7. 優秀若手表彰.

内海　伶那　「Mn-Mo 合金水素化物の高温高圧合成」

公益社団法人日本金属学会 水素化物に関わる次世代学術・応用展開研究会, 2021-11-18

8. 第 62 回高圧討論会ポスター賞.

内海　伶那　「Mn に富む Al-Mn 合金水素化物の高温高圧合成」

日本高圧力学会, 2021-10-19

9. 第 15 回水素若手研究会ポスター賞.

内海　伶那　「Fe-Mo 合金の高温高圧水素化反応の組成依存性」

水素若手研究会, 2021-09-07

10. 令和２年度大阪ニュークリアサイエンス協会（ONSA）賞.

三井　隆也　「表面を一原子層単位の深さ精度で磁性探査できる新技術を開発 ―鉄の磁石の「表面の謎」を解明！―」

一般社団法人　大阪ニュークリアサイエンス協会, 2021-06-10

11. 泰山賞.

桐山　博光、Alexander Selgeivich Pirozhkov、神門　正城　「世界最高高性能ペタワットレーザーの開発と量子ビーム制御」

公益財団法人　レーザー技術総合研究所, 2021-11-17

特許登録

1. Spectroscopic apparatus.

Imazono Takashi, Koike Masato, Terauchi Masami, Sasai Hiroyuki, Takahashi Hideyuki

EU 登録　2647983 (2021-5-26)

2. 血中物質濃度測定装置及び血中物質濃度測定方法.

Yamakawa Koichi

EU 登録 EP 3248544 B1 (2021-12-08)

3. 血中物質濃度測定装置及び血中物質濃度測定方法.

Yamakawa Koichi

中国登録 CN 107427266 B (2021-12-3)

特許出願

1. 合金、水素取出システム、水素吸蔵材、および合金の製造方法.

山本　春也, 齋藤　寛之, 田口　富嗣, 八巻　徹也

特願 2021-132850 (2021-08-17)

2. 測定装置及び測定方法.

神門　正城, 黄　開

特願 2022-034464 (2022-03-07)

3. 光学測定装置、および光学測定方法.

森　道昭, 森　道昭, 小瀧　秀行, 小瀧　秀行, 林　由紀雄, 林　由紀雄, 神門　正城, 神門, 中新　信彦, 中新, 黄　開, 黄　開, 近藤　公伯

特願 2022-032770 (2022-03-03)

4. レーザ加速粒子ビーム装置およびレーザ加速粒子ビーム発生方法.

中新　信彦, 神門　正城, 黄　開, 近藤　康太郎

特願 2022-030350 (2022-02-28)

5. 加振装置、検査システム、及び加振方法.

錦野　将元, 北村　俊幸

特願 2021-163076 (2021-10-01)

6. 磁化測定方法.

稲見　俊哉, 菅原　健人, 綿貫　徹, 小出　明広, 野村　拓司

PCT/JP2021/044470 (2021-12-03)

7. 磁化測定装置及び磁化測定方法.
　　稲見　俊哉, 菅原　健人, 綿貫　徹, 小出　明広, 野村　拓司
　　PCT/JP2021/044469 (2021-12-03)
8. データ取得装置、データ補正装置、データ補正方法、プログラム及び記録媒体.
　　佐々木　拓生, 高橋　正光
　　特願 2022-041838 (2022-03-16)
9. 水素吸蔵材およびその製造方法.
　　齋藤　寛之, 内海　伶那, 綿貫　徹
　　特願 2022- 39521 (2022-03-14)
10. 新規ヒトインターロイキン１８変異体及びその用途.
　　田中　義正, 櫻庭　俊
　　特願 2021-01941 (2021-02-10)

The Kids' Science Museum of Photons

きっづ光科学館ふぉとんは、2020 年度の 300 人を上回る 757 人の方々にご来館いただきました。

　2021 年度も新型コロナウィルスの感染拡大防止のため年度当初より臨時休館することとなりましたが、4 月に一般社団法人 VR 革新機構（VRIO）の公益事業プログラム（コロナ禍の博物館等を支援する 3D+VR ボランティア撮影）により、科学館内部を撮影していただきました。レーザースキャナーや赤外線カメラによるデータも用いて構成される 3D ビューコンテンツにより、館内見学を仮想体験できます。また、超長尺三脚を駆使して計測・撮影されたデータや画像も併用・統合して構築された「ドールハウス表示」により、館内部を俯瞰することもできます。

　公開 URL　　https://my.matterport.com/show/?m=wAeZTtF8jv8
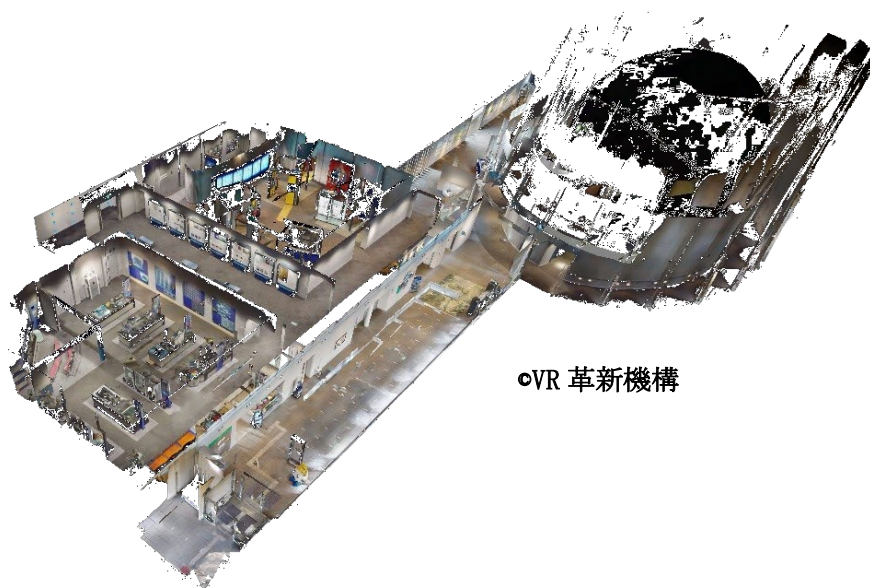
©VR 革新機構

科学館 3D ビューコンテンツのドールハウス表示

　7 月上旬より課外授業（学習投影）等の場として利用していただくため、プラネタリウムの上映を事前予約制で再開しました。7 月 11 日に開館 20 周年を迎え、7 月 25 日には入館者数が 75 万人に達しました。その後、8 月半ばに京都府に緊急事態宣言が発出されたことにともない 9 月末まで休館、10 月より再開し、プラネタリウムに加え希望者には親子工作を体験していただいています。偏光板工作や分光板工作のサンプルや作品の試作を行うとともに、ウェルカムボードや月替わりの偏光グラフィックスの作成・展示も行いました。

　関西研の施設公開（10 月 31 日）では、プラネタリウムの上映を入替制で 4 回行い、「案内・誘導・上映・座席消毒」の工程も 4 セットとなり、慌ただしくも活気のある一日となりました。

ふぉとん 20 周年（7 月 11 日）

ふぉとんウェルカムボード

偏光グラフィックス展示

75万人達成（7月25日）

工作体験

2022年1月より、「光の不思議体験コーナー」を受付エリアに開設し、鏡とハーフミラーの間にLEDライトを配置してできる無限鏡（光のトンネル）や錐体万華鏡、立方体万華鏡を体験していただきました。

無限鏡
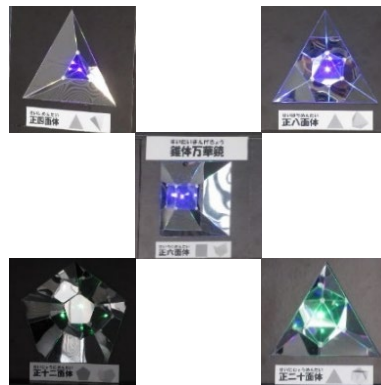
錐体万華鏡

立方体万華鏡

年度末には、光の科学ゾーンの展示装置「波のテーブル」の改修ならびに館外で記念撮影などに用いるパネルの更新を行いました。

「波のテーブル」

記念撮影パネル

Appendix

共同研究課題、施設共用課題

1）木津地区

【共同研究課題】

共同研究先	共同研究課題名	担当研究グループ
日本原子力研究開発機構	中性子散乱による生体高分子のダイナミクス解析に関する研究	生体分子シミュレーショングループ
大阪大学、東北大学	シンチレータを用いた相対論的イオン検出手法の開発	先端レーザー技術開発グループ
東京大学	半古典 Vlasov 方程式に基づくレーザー加工シミュレータの研究開発	超高速光物性研究グループ
京都大学	レーザー誘起弾性波技術によるインフラ構造物診断の高度化に関する研究	X線レーザー研究グループ
日本電信電話株式会社	アト秒パルスの波形計測と時間分解計測に関わる基盤技術開発	超高速光物性研究グループ
大阪大学	超高強度レーザーと固体物質からのガンマ線発生及び核物理に関する研究	高強度レーザー科学研究グループ
慶應義塾大学、近畿大学	レーザーを活用した整形外科インプラント設置強度評価機構の開発	X線レーザー研究グループ
株式会社島津製作所	高耐性光学デバイスの開発研究	X線レーザー研究グループ
宇都宮大学、広島大学、東北大学	高輝度軟X線発生に関する基礎研究	X線レーザー研究グループ
京都大学	TW 級チタンサファイアレーザーを用いた量子ビーム発生に関する研究	X線レーザー研究グループ
奈良女子大学	レーザー誘起振動波計測の機械学習手法の適用に関する研究	X線レーザー研究グループ
株式会社フォトンラボ	レーザー誘起振動波計測技術の小型化に関する研究	X線レーザー研究グループ
芝浦工業大学	レーザー誘起振動波計測技術の高度化に関する研究	X線レーザー研究グループ
NTT アドバンステクノロジ株式会社	高耐力軟X線光学素子に関する基礎研究	X線レーザー研究グループ
東京学芸大学	リラクサー強誘電体のドメイン形成に関する研究	X線レーザー研究グループ
ライトタッチテクノロジー株式会社	中赤外レーザーを用いた医療応用計測技術の開発	光量子科学研究部

理化学研究所	テラヘルツパルス光源による高分子高次構造の制御	超高速光物性研究グループ
大阪大学	高強度テラヘルツパルス光源による新規物質創成と新規物性発現に関する研究	超高速光物性研究グループ
奈良先端科学技術大学院大学	有機半導体におけるフォノン-励起子相互作用を利用した状態制御に関する基盤技術開発	超高速光物性研究グループ
兵庫県立粒子線医療センター	量子メスに向けた粒子線照射計測及び制御技術に関する研究	高強度レーザー科学研究グループ
東北大学、島津製作所	極端紫外線領域の低入射角回折格子の開発	先端レーザー技術開発グループ
同志社大学	フェムト秒パルスレーザーの位相受動整合コヒーレント加算に関する研究	先端レーザー技術開発グループ
神戸大学、名古屋大学、東京大学	固体飛跡検出器を用いた高エネルギーイオン検出手法開発	先端レーザー技術開発グループ
京都大学	高強度レーザーと構造性媒質との相互作用に関する研究	先端レーザー技術開発グループ
大阪大学、青山学院大学	宇宙物理の手法に基づく粒子加速・電磁放射に関する研究	先端レーザー技術開発グループ
核融合科学研究所、京都工芸繊維大学、富山高等専門学校	凝縮相の量子・分子動力学計算に関する研究	X線レーザー研究グループ
大阪大学	レーザー電子加速の安定化・性能評価研究	高強度レーザー科学研究グループ
住友重機械工業株式会社	量子メス用レーザー加速入射器の評価手法の開発	光量子科学研究部
日立造船株式会社	量子メス用レーザー加速入射器のターゲット駆動装置に関する研究開発	光量子科学研究部
日本電子	電子顕微鏡搭載用高感度軟X線回折格子分光器の開発	光量子科学研究部
筑波大学	光・電子融合第一原理ソフトウェア「SALMON」の開発及び利用研究	超高速光物性研究グループ
株式会社 NAT	小型レーザー駆動量子ビームの安定運用の研究	高強度レーザー科学研究グループ
株式会社日本防振工業	レーザー電子加速に資する防振・光軸安定化に関する研究	高強度レーザー科学研究グループ
大阪大学	フェムト秒レーザー・物質相互作用の高速計測に関する研究	高強度レーザー科学研究グループ

【施設共用課題】

課題番号	利用区分	施設装置	利用課題
2021B-K01	公開	J-KAREN-P レーザー装置	陽子線計測の統計的有意性に基づいたレーザー駆動イオン加速の高強度化

2）播磨地区

【共同研究課題】

共同研究先	共同研究課題名	担当研究グループ
物質・材料研究機構	原子二体分布関数法による機能性材料の先進的ナノ構造研究	高圧・応力科学研究グループ
京都大学	同位体特定による局所状態解明のための先進的メスバウアー分光法の開発研究	磁性科学研究グループ
京都大学、分子科学研究所、理化学研究所	コヒーレント X 線を利用したナノ粒子計測に関する研究	コヒーレント X 線利用研究グループ
広島大学	コヒーレント X 線を利用した強誘電体一粒子計測	コヒーレント X 線利用研究グループ
京都大学	ナノ粒子を取り込んだがん細胞に及ぼす高エネルギー単色 X 線照射の影響に関する研究	高圧・応力科学研究グループ
JEF テクノリサーチ株式会社	磁気円偏光発光を用いた方向性珪素鋼板の内部磁区観察のための研究開発	磁性科学研究グループ
日本原子力研究開発機構	放射光による物質科学に関する研究	放射光科学研究センター
産業技術総合研究所	水素雰囲気その場・時分割放射光 X 線全散乱を利用した水素吸蔵合金の構造変化の観測	高圧・応力科学研究グループ
東北大学、上智大学	水素雰囲気その場・時分割放射光 X 線全散乱を利用した水素吸蔵合金の構造変化の観測	磁性科学研究グループ

【施設共用課題】

　播磨地区では 2012 年度より文部科学省のナノテクノロジープラットフォーム事業を受託しており、放射光科学研究施設を成果公開型課題で利用する外部研究者に対して、特に専用ビームラインにおける研究支援を強化しています。課題は年 2 回、SPring-8 を運営する公益財団法人高輝度光科学研究センターの一般課題募集時期（5 月及び 11 月）に合わせて募集しています。

課題番号	利用区分	利用装置	研究課題
2021A-H01	公開	放射光メスバウアー分光装置	Dy 放射光メスバウアー吸収分光法の高度化による単分子磁石の磁気緩和過程解明
2021A-H02	公開	放射光メスバウアー分光装置	電荷秩序配列に起因する純核ブラッグ散乱の測定
2021A-H03	公開	放射光メスバウアー分光装置	放射光メスバウアー分光を利用した (Al，Fe3+)OOH中の鉄のスピン状態の圧力依存性の解明
2021A-H04	公開	共鳴X線非弾性散乱装置	Investigating the electronic structure of Cu2ZnSnSe4 by resonant inelastic x-ray scattering at Cu K-edge
2021A-H05	公開	表面X線回折計	RF-MBE法による窒化物半導体成長初期過程のXRDその場観察
2021A-H06	公開	表面X線回折計	アモルファスカーボン量の最適化によるグラフェン析出成長の過飽和度制御
2021A-H07	公開	表面X線回折計	InGaN自立基板製作に向けたその場X線回折測定による成長制御
2021A-H08	公開	表面X線回折計	グラフェンを用いたサファイア上でのGaNのリモートエピタキシーのリアルタイムX線回折
2021A-H09	公開	高温高圧プレス装置	ポリエチレンの高温高圧Hexagonal相の存在領域の研究
2021A-H10	公開	高温高圧プレス装置	Colossal Negative Thermal Expansion in Polar Perovskites with Large Tetragonality
2021A-H11	公開	高温高圧プレス装置	放射光透過ラウエによるマグネシウム系材料の曲げ加工後の内部損傷評価
2021A-H12	公開	高温高圧プレス装置	高圧合成技術を活用した熱化学式水素圧縮機用新規水素吸蔵合金の探索
2021A-H13	公開	高温高圧プレス装置	高圧下水素化技術による鉄鋼材料の新奇無拡散相の探索（2）
2021A-H14	公開	高温高圧プレス装置	マグネシウム系遷移金属錯体水素化物における高温高圧合成過程のその場観察
2021A-H15	公開	高温高圧プレス装置	白色X線と二重露光法による溶接底部の残留応力評価
2021A-H16	公開	高温高圧プレス装置	合金化溶融亜鉛メッキ鋼板抵抗スポット溶接部における溶接割れの放射光X線イメージング
2021A-H17	公開	ダイヤモンドアンビルセル回折計	PbFeO3における圧力誘起金属間電荷移動転移の観測と負熱膨張化への展開
2021A-H19	非公開	共鳴X線非弾性散乱装置	RIXSを駆使したSCM415鋼の水素トラップ現象解明

2021B-H01	公開	放射光メスバウアー分光装置	金属−窒素−ドープカーボン触媒の局所活性サイト構造の解明
2021B-H03	公開	放射光メスバウアー分光装置	高水素圧力下におけるEu水素化物の電子状態分析
2021B-H04	公開	放射光メスバウアー分光装置	純核ブラッグ散乱法による自然鉄試料のサイト選択的スペクトル測定
2021B-H05	公開	共鳴非弾性X線散乱装置	準静的磁場変化における方向性電磁鋼板の内部磁区構造調査
2021B-H06	公開	表面X線回折計	放射光X線を用いたヘテロ界面上の転位生成ダイナミクスと転位すべり面分布の測定
2021B-H07	公開	表面X線回折計	放射光X線を用いた格子不整合III−V族化合物半導体混晶のリアルタイム構造解析
2021B-H08	公開	表面X線回折計	GaN/グラフェン基板上でのInGaNヘテロエピタキシャル成長における応力緩和過程の観察
2021B-H09	公開	表面X線回折計	InGaNエピタキシャル成長におけるその場X線回折測定による歪み制御
2021B-H10	公開	高温高圧プレス装置	高圧合成技術を活用した熱化学式水素圧縮機用新規水素吸蔵合金の水素放出挙動の観察
2021B-H11	公開	高温高圧プレス装置	水素貯蔵合金の潜在化された水素吸蔵サイトの解明
2021B-H12	公開	高温高圧プレス装置	Mg−W系遷移金属錯体水素化物の高温高圧合成過程のその場観察
2021B-H13	公開	高温高圧プレス装置	中Mn鋼の残留オーステナイト変態挙動, 引張変形時の相応力分配挙動と優れた延性発現機構の解明
2021B-H14	公開	高温高圧プレス装置	X線回折とX線透過法を用いたTi−Mg系の高圧高温状態のその場観察
2021B-H15	公開	高温高圧プレス装置	高温高圧法を用いた酸水素化物合成の直接観察
2021B-H16	公開	高温高圧プレス装置	鉄鋼材料の高温圧縮過程のX線その場観察
2021B-H17	公開	高温高圧プレス装置	放射光白色X線を用いた高強度鋼板抵抗スポット溶接継手の内部ひずみ分布の測定
2021B-H19	公開	ダイヤモンドアンビルセル回折計	PbFeO3における圧力誘起金属間電荷移動転移の観測と負熱膨張化への展開II
2021B-H23	非公開	大型X線回折計	円筒電池かしめ部の残留応力評価

関西光科学研究所での各種シンポジウム・施設公開・出展・アウトリーチ活動

　全世界的な新型コロナウイルス感染症（COVID-19) の影響で、2021 年度も対面での活動が大きく制限されました。そのような状況下ですが、関西研（木津地区、播磨地区）の各種シンポジウム、セミナー、研究会等について主なものを記載します。

　年 1 回の施設公開について木津地区では 2021 年 10 月 31 日（日）に人数制限・事前登録のうえ当日の感染症対策を徹底して開催しました。なお、播磨地区での開催は見送りました。
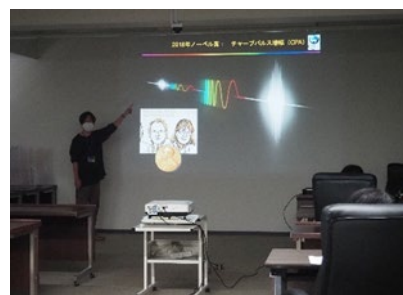
関西研施設公開（木津地区）
スーパーサイエンスセミナー

【木津地区】

1	22-JUN-2021	オンライン開催	主催：阪大・レーザー科学研究所、量研・関西光科学研究所
	光・量子ビーム科学合同シンポジウム 2021 OPTO2020　Symposium on Photon and Beam Science		
2	30-JUN-2021	オンライン開催（発表）	主催：関西文化学術研究都市推進機構
	けいはんな若手研究者交流会（第 44 回）		
3	29-OCT-2021	オンライン開催（発表）	主催：関西文化学術研究都市推進機構
	けいはんな若手研究者交流会（第 45 回）		
4	31-OCT-2021	関西光科学研究所（木津地区：京都府木津川市）	主催：関西光科学研究所
	関西光科学研究所施設公開（木津地区）		
5	11-13-NOV-2021	オンライン開催（出展）	主催：けいはんな R&D フェア 2020 実行委員会、関西文化学術研究都市推進機構
	京都 R&D フェア 2021、けいはんなビジネスメッセ 2021		
6	3-DEC-2021	オンライン開催	主催：関西文化学術研究都市推進機構
	けいはんなサイエンスカフェ（第 88 回）		
7	4-FEB-2022	オンライン開催	主催：RIKEN-RAP & QST- KPSI
	第 5 回 RIKEN-RAP & QST-KPSI ジョイントセミナー		

【播磨地区】

1	14-16-JUN-2021	つくば国際会議場+オンライン開催	主催：公益社団法人日本顕微鏡学会
	公益社団法人日本顕微鏡学会 2021 年度第 77 回学術講演会「S-8　ナノテクノロジープラットフォーム・微細構造解析プラットフォーム 10 年間の活動と成果」シンポジウム		
2	11-14-JUL-2021	SPring-8 （兵庫県佐用郡佐用町）	主催：兵庫県立大学理学部／大学院理学研究科、関西学院大学理学部・工学部・生命環境学部・大学院理工学研究科、東京大学 放射光分野融合国際卓越拠点、岡山大学、大阪大学未来

			戦略光科学連携センター・蛋白質研究所・核物理研究センター、茨城大学大学院理工学研究科、(公財)高輝度光科学研究センター(JASRI)、理化学研究所 放射光科学研究センター、日本原子力研究開発機構 物質科学研究センター、量子科学技術研究開発機構 関西光科学研究所
	第 21 回 SPring-8 夏の学校		
3	16-SEP-2021	物質・材料研究機構千現地区+オンライン開催	主催：国立研究開発法人物質・材料研究機構ナノテクノロジープラットフォームセンター
	文部科学省ナノテクノロジープラットフォーム令和 3 年度利用成果発表会		
4	17-SEP-2021	物質・材料研究機構千現地区+オンライン開催	主催：国立研究開発法人物質・材料研究機構ナノテクノロジープラットフォームセンター
	令和 3 年度文部科学省ナノテクノロジープラットフォーム学生研修プログラム成果発表会		
5	14-OCT-2021	オンライン開催	主催：SPring-8 ユーザー協同体（SPRUC）、（公財）高輝度光科学研究センター、理化学研究所放射光科学研究センター
	令和 3 年度文部科学省ナノテクノロジープラットフォーム事業　JAEA＆QST 微細構造解析プラットフォーム放射光設備利用講習会　－反応・合成とバルク・表層の構造解析－		
6	8-10-NOV-2021	幕張メッセ国際展示場（千葉県千葉市）	主催：QST 微細構造解析プラットフォーム、JAEA 微細構造解析プラットフォーム
	Japan Analytical & Scientific Instruments Show（JASIS）　2021		
7	24-26-NOV-2021	九州大学医学部百年講堂	主催：一般社団法人日本分析機器工業会、一般社団法人日本科学機器協会
	日本顕微鏡学会　第 64 回シンポジウム　文部科学省ナノテクノロジープラットフォーム微細構造解析プラットフォームブース展示		
8	16-DEC-2021	オンライン開催	主催：日本顕微鏡学会
	文部科学省ナノテクノロジープラットフォーム　JAEA＆QST 微細構造解析プラットフォーム合同地域セミナー　－ 最新の電子状態・表面反応・結晶構造解析 －		
9	7-9-JAN-2022	東京大学本郷キャンパス+オンライン開催	主催：JAEA 微細構造解析プラットフォーム、QST 微細構造解析プラットフォーム
	第 35 回日本放射光学会年会・放射光科学合同シンポジウム		
10	26-28-JAN-2022	東京ビッグサイト+オンライン開催	主催：第 35 回日本放射光学会年会・放射光科学合同シンポジウム組織委員会
	第 20 回国際ナノテクノロジー総合展・技術会議（nano tech 2021）		
11	28-JAN-2022	東京ビッグサイト+オンライン開催	主催：nano tech 2022 実行委員会
	文部科学省ナノテクノロジープラットフォーム第 20 回ナノテクノロジー総合シンポジウム JAPANNANO 2022　ナノテクノロジープラットフォームからマテリアル DX プラットフォームへ〜マテリアル先端リサーチインフラの目指すもの〜		
12	3-MAR-2022	東京大学本郷キャンパス+オンライン開催	主催：文部科学省ナノテクノロジープラットフォーム、国立研究開発法人物質・材料研究機構ナノテクノロジープラットフォームセンター
	微細構造解析プラットフォームシンポジウム（10 年の総括）		

13	4-MAR-2022	オンライン開催	主催：国立研究開発法人物質・材料研究機構微細構造解析プラットフォーム
	令和3年度文部科学省ナノテクノロジープラットフォーム事業京大・JAEA・QST 微細構造解析プラットフォーム合同地域セミナー　—最新の微細構造・状態解析—		
14	8-MAR-2022	物質・材料研究機構千現地区+オンライン開催	主催：京大微細構造解析プラットフォーム最先端構造観察・計測共用拠点、QST 微細構造解析プラットフォーム、JAEA 微細構造解析プラットフォーム
	文部科学省ナノテクノロジープラットフォーム令和3年度総会		
15	9-MAR-2022	物質・材料研究機構千現地区+オンライン開催	主催：国立研究開発法人物質・材料研究機構ナノテクノロジープラットフォームセンター
	令和3年度文部科学省ナノテクノロジープラットフォーム技術スタッフ交流プログラム報告会		

KPSI セミナー（第 79 回～85 回）

　QST 木津地区では国内外の著名な研究者をお招きして学術的に最先端の専門的なセミナーを開催しています。今年度は人数制限した会場から Web 中継も行うハイブリッドセミナーを中心に合計 7 回開催しました。開催にあたっては KPSI Web サイトやけいはんなメーリングリストを活用し、関西研内外に開催案内を行っています。また報告については Web サイト、関西研だより等を活用しています。（参加費無料・事前登録制）

　Web サイト：https://www.qst.go.jp/site/kansai-topics/29853.html

高部英明教授

79	27-MAY-2021	Prof. Hideaki Takabe	National Taiwan University
	Hawking radiation from true and analog black holes = Grasping physics intuitively and thinking about analog black hole experiments with ultra-intense lasers =		
80	28-SEP-2021	染川　智弘	（公財）レーザー技術総合研究所、大阪大学レーザー科学研究所
	海底開発における環境影響評価に向けた水中レーザーリモートセンシング技術の開発		
81	8-OCT-2021	Associate Prof. Jiro Itatani	ISSP, The Univ. of Tokyo
	Intense ultrashort-pulse sources for materials science		
82	12-OCT-2021	Associate Professor Tomomasa Ohkubo	Tokyo University of Technology,
	Development of Solar-Pumped Laser		
83	18-OCT-2021	Prof. Kenichi L. Ishikawa	The University of Tokyo
	Building Science and Theory of Laser-Matter Interaction toward Super-Smart Society		
84	10-DEC-2021	佐々木　茂美	広島大学
	量子ビームが運ぶ光の軌道角運動量 光の軌道角運動量を持つ X 線ビームで何が出来るか？		

85	20-JAN-2022	紀井　俊輝	京都大学
バルク超伝導体の新しい応用　遮蔽電流制御による高度な磁場分布デザイン			

左から、第 80 回 染川智弘博士、第 81 回 板谷治郎先生、第 82 回 大久保友雅先生
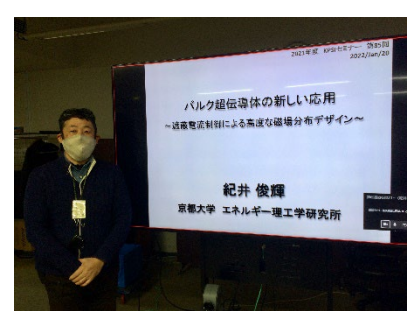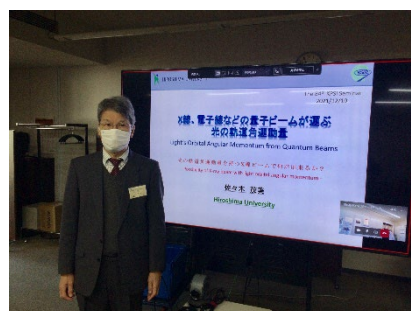
左から、第 83 回 石川顕一博士、第 84 回 佐々木茂美先生、第 85 回 紀井俊輝先生

QST 播磨セミナー（第 22 回～第 30 回）

　播磨地区では QST 内の研究者や国内外の著名な研究者によるセミナーを開催しています。2021年度は新型コロナウイルス感染症防止対策のため、オンライン開催としました。

22	21-APR-2021	Dr. Ayumi Shiro	High Pressure Science and Stress Research Group, QST
Tumor spheroid destruction by gadolinium-loaded nanoparticles irradiated with synchrotron radiation monochromatic X-rays			
23	26-MAY-2021	Dr. Yoshinori Katayama	Kansai Photon Science Institute, QST
Overview of Advanced Research Infrastructure for Materials Science Project			
24	23-JUN-2021	Dr. Kenji Tsutsui	Condensed Matter Theory Group, QST
Antiphase Oscillations of the Time-Resolved Spin Structure Factor in Antiferromagnetic Mott Insulators			
25	14-JUL-2021	Dr. Mao Ye	State Key Laboratory of Functional Materials for Informatics, Shanghai Institute of Microsystem and Information Technology, Chinese Academy of Sciences
Recent Progress and Activities of the Soft-X-ray and Vacuum-Ultraviolet Beamlines at Shanghai Synchrotron Radiation Facility			

| 26	21-JUL-2021	Dr. Morihisa Saeki	Tokai Quantum Beam Science Center, Takasaki Advanced Radiation Research Institute, QST
	Dispersive XAFS Study on Laser-induced Photoreduction of Rhodium(III) Complexes: Information Extraction of Rh Intermediate by MCR-ALS Analysis		
27	25-AUG-2021	Dr. Hideaki Iwasawa Dr. James Harries	Magnetism Research Group, QST Coherent X-ray Research Group, QST
	Remote experiments at domestic and international synchrotron radiation facilities		
28	22-SEP-2021	Dr. Hiroyuki Saito	High Pressure Science and Stress Research Group, QST
	- Hydrogen storage with earth abundant metals - Current situation of data structuring in Materials Advanced Research Infrastructure project		
29	27-OCT2021	Dr. Tetsuro Ueno	Magnetism Research Group, QST
	Automated stopping criterion for spectral measurement with active learning		
30	30-NOV-2021	Dr. Takuji Nomura	Condensed Matter Theory Group, QST
	Theory of L-shell x-ray magnetic circularly polarized emission: New optical sum rules		
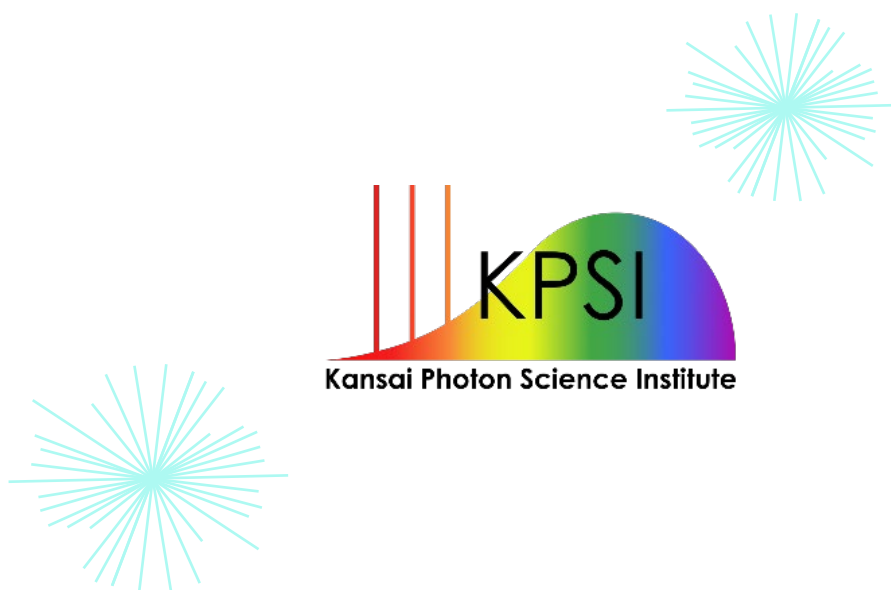
Kansai Photon Science Institute
Quantum Beam Science Research Directorate
National Institutes for Quantum Science and Technology

8-1-7, Umemidai. Kizugawa-shi, Kyoto 619-0215, Japan
https://www.qst.go.jp/site/kansai-english/